

Electronic Theses and Dissertations, 2004-2019

2008

N Multilayer Thin Film Reactions To Form L10 Fept And Exchange Spring Magnets

Bo Yao

University of Central Florida

 Part of the [Materials Science and Engineering Commons](#)
Find similar works at: <https://stars.library.ucf.edu/etd>
University of Central Florida Libraries <http://library.ucf.edu>

This Doctoral Dissertation (Open Access) is brought to you for free and open access by STARS. It has been accepted for inclusion in Electronic Theses and Dissertations, 2004-2019 by an authorized administrator of STARS. For more information, please contact STARS@ucf.edu.

STARS Citation

Yao, Bo, "N Multilayer Thin Film Reactions To Form L10 Fept And Exchange Spring Magnets" (2008).
Electronic Theses and Dissertations, 2004-2019. 3678.
<https://stars.library.ucf.edu/etd/3678>

[Fe/Pt]_n MULTILAYER THIN FILM REACTIONS TO FORM L1₀ FePt AND
EXCHANGE SPRING MAGNETS

by

BO YAO

B.S. Huazhong University of Science and Technology, China, 1996

M.S. Huazhong University of Science and Technology, China, 1999

A dissertation submitted in partial fulfillment of the requirements
for the degree of Doctor of Philosophy
in the Department of Mechanical, Materials and Aerospace Engineering
in the College of Engineering and Computer Science
at the University of Central Florida
Orlando, Florida

Fall Term

2008

Major Professor: Kevin R. Coffey

@ 2008 Bo Yao

ABSTRACT

FePt films with the $L1_0$ phase have potential applications for magnetic recording and permanent magnets due to its high magnetocrystalline anisotropy energy density. Heat treatment of $[\text{Fe/Pt}]_n$ multilayer films is one approach to form the $L1_0$ FePt phase through a solid state reaction. This thesis has studied the diffusion and reaction of $[\text{Fe/Pt}]_n$ multilayer films to form the $L1_0$ FePt phase and has used this understanding to construct exchange spring magnets. The process-structure-property relations of $[\text{Fe/Pt}]_n$ multilayer films were systematically examined.

The transmission electron microscopy (TEM) study of the annealed multilayers indicates that the Pt layer grows at the expense of Fe during annealing, forming a disordered *fcc* FePt phase by the interdiffusion of Fe into Pt. This thickening of the *fcc* Pt layer can be attributed to the higher solubilities of Fe into *fcc* Pt, as compared to the converse. For the range of film thickness studied, a continuous $L1_0$ FePt product layer that then thickens with further annealing is not found. Instead, the initial $L1_0$ FePt grains are distributed mainly on the grain boundaries within the *fcc* FePt layer and at the Fe/Pt interfaces and further transformation of the sample to the ordered $L1_0$ FePt phase proceeds coupled with the growth of the initial $L1_0$ FePt grains.

A comprehensive study of annealed $[\text{Fe/Pt}]_n$ films is provided concerning the phase fraction, grain size, nucleation/grain density, interdiffusivity, long-range order parameter, and texture, as well as magnetic properties. A method based on hollow cone dark field TEM is introduced to measure the volume fraction, grain size, and density of ordered $L1_0$ FePt phase grains in the annealed films, and low-angle X-ray diffraction is used to measure the effective Fe-Pt interdiffusivity.

The process-structure-properties relations of two groups of samples with varying substrate temperature and periodicity are reported. The results demonstrate that the processing parameters (substrate temperature, periodicity) have a strong influence on the structure (effective interdiffusivity, LI_0 phase volume fraction, grain size, and density) and magnetic properties. The correlation of these parameters suggests that the annealed $[\text{Fe}/\text{Pt}]_n$ multilayer films have limited nuclei, and the subsequent growth of LI_0 phase is very important to the extent of ordered phase formed. A correlation between the grain size of fcc FePt phase, grain size of the LI_0 FePt phase, the LI_0 FePt phase fraction, and magnetic properties strongly suggests that the phase transformation of $fcc \rightarrow LI_0$ is highly dependent on the grain size of the parent fcc FePt phase. A selective phase growth model is proposed to explain the phenomena observed.

An investigation of the influence of total film thickness on the phase formation of the LI_0 FePt phase in $[\text{Fe}/\text{Pt}]_n$ multilayer films and a comparison of this to that of FePt co-deposited alloy films is also conducted. A general trend of greater LI_0 phase formation in thicker films was observed in both types of films. It was further found that the thickness dependence of the structure and of the magnetic properties in $[\text{Fe}/\text{Pt}]_n$ multilayer films is much stronger than that in FePt alloy films. This is related to the greater chemical energy contained in $[\text{Fe}/\text{Pt}]_n$ films than FePt alloy films, which is helpful for the LI_0 FePt phase growth. However, the initial nucleation temperature of $[\text{Fe}/\text{Pt}]_n$ multilayers and co-deposited alloy films was found to be similar.

An investigation of LI_0 FePt-based exchange spring magnets is presented based on our understanding of the LI_0 formation in $[\text{Fe}/\text{Pt}]_n$ multilayer films. It is known that exchange coupling is an interfacial magnetic interaction and it was experimentally shown that this interaction is limited to within several nanometers of the interface. A higher degree of order of

the hard phase is shown to increase the length scale slightly. Two approaches can be used to construct the magnets. For samples with composition close to stoichiometric LI_0 FePt, the achievement of higher energy product is limited by the average saturation magnetization, and therefore, a lower annealing temperature is beneficial to increase the energy product, allowing a larger fraction of disordered phase. For samples with higher Fe concentration, the $(BH)_{max}$ is limited by the low coercivity of annealed sample, and a higher annealing temperature is beneficial to increase the energy product.

In memory of my parents.

ACKNOWLEDGMENTS

First of all I would like to express my gratitude to my advisor, Dr. Kevin Coffey, for the support, supervision, guidance, and encouragement. I thank my other committee members, Dr. Katayun Barmak, Dr. C. Suryanarayana, Dr. Yongho Sohn, and Dr. Helge Heinrich for thoughtful discussions and valuable comments.

The Advanced Materials Processing and Analysis Center (AMPAC), and Department of Mechanical, Materials and Aerospace Engineering (MMAE) are acknowledged. I thank administrative personnel, Cynthia Harle, Karen Glidewell, and Kari Stiles for their help.

It is a pleasure to work in Materials Characterization Facility (MCF) for these years. I appreciate the help and support from the engineers in MCF, Kirk Scammon, Mikhail Klimov, and Zia ur Rahman. Dr. Helge Heinrich is highly appreciated for teaching me both the theory and practical operation of TEM.

I would like to thank Andrew Warren for introducing me to many instruments in MCF, making my beginning life here much easier. Edward Dein is acknowledged for giving me a lot of help in the cleaning room and setting up the AGFM. I thank my colleagues, Ravi Todi, Parag Gadkari, Tik Sun, Chaitali China, Amurata Borge, Prabhu Doss Mani, and Vinit Todi for the help, especially for the sample preparation in the cleaning room.

Finally, special thanks go to my wife, Hui, and my daughter, Daphne.

TABLE OF CONTENTS

ABSTRACT	iii
LIST OF FIGURES.....	xii
LIST OF TABLES.....	xxi
LIST OF ACRONYMS/ABBREVIATIONS	xxiii
CHAPTER 1 INTRODUCTION AND BACKGROUND.....	1
1.1 $L1_0$ FePt and Fe-Pt system	1
1.2 $L1_0$ FePt material for thin film magnetic recording.....	8
1.3 $L1_0$ FePt based exchange-coupled permanent magnets	17
1.4 Phase transformation.....	29
1.4.1 General introduction	29
1.4.2 Disorder-order phase transformation of FePt	34
1.4.3 Phase transformation in thin films	37
1.4.4 Phase transformation through thin film multilayer reactions	39
CHAPTER 2 MOTIVATION, OBJECTIVE, AND THESIS OUTLINE	42
CHAPTER 3 EXPERIMENTAL METHODS.....	47
3.1 DC/RF magnetron sputtering.....	48
3.2 Modified tube furnace.....	49
3.3 Rutherford backscattering spectrometry	52
3.4 Transmission electron microscopy	54
3.5 X-Ray Reflectometry	59

3.6	Alternating Gradient Field Magnetometry.....	61
CHAPTER 4 XTEM STUDY ON THE DIFFUSION AND REACTION OF [Fe/Pt] _n		
MULTILAYER THIN FILMS.....		
4.1	Introduction.....	62
4.2	Experiments	64
4.3	Results and discussion	65
4.4	Conclusions.....	74
CHAPTER 5 THE INFLUENCE OF PERIODICITY AND DEPOSITION		
TEMPERATURE ON THE DIFFUSIVITY, STRUCTURE AND MAGNETIC		
PROPERTIES OF ANNEALED MULTILAYER FILMS		
5.1	Introduction.....	75
5.2	Methods.....	78
5.2.1	Interdiffusivity measurement in [Fe/Pt] _n multilayer films.....	78
5.2.2	Volume fraction of <i>L1₀</i> FePt phase.....	81
5.2.3	Long-range order parameter	92
5.2.4	Grain size and nucleation/grain density of the <i>L1₀</i> FePt phase.....	98
5.3	Experiments	101
5.4	Results.....	103
5.4.1	Multilayer structure.....	103
5.4.2	Effective interdiffusivity.....	105
5.4.3	Microstructure of annealed [Fe/Pt] _n multilayer films	110
5.4.4	Long-range order parameter	120

5.4.5	Volume fraction and nucleation/grain density of $L1_0$ FePt phase.....	125
5.5	Magnetic properties	129
5.6	Discussion.....	132
5.7	Conclusions.....	141
CHAPTER 6 THE INFLUENCE OF THE FILM THICKNESS ON THE FORMATION		
OF L_{10} FePt PHASE		142
6.1	Introduction.....	142
6.2	Experiments	144
6.3	Results.....	146
6.3.1	Multilayer samples (“ML_THK_8” to “ML_THK_100”)	146
6.3.2	Comparison of $[Fe/Pt]_n$ with co-sputtered FePt samples	153
6.4	Discussion and Conclusions	161
CHAPTER 7 EXCHANGE SPRING MAGNETS INVESTIGATION		165
7.1	Introduction and review	165
7.2	Experiments	169
7.3	Results and discussion	170
7.3.1	The scale of exchange coupling length.....	170
7.3.2	Construction of exchange coupled magnets	174
7.4	Conclusions.....	182
CHAPTER 8 SUMMARY		183
8.1	Conclusions.....	183
8.2	Future work.....	186

APPENDIX A THEORY OF EFFECTIVE INTERDIFFUSIVITY OF MULTILAYER FILMS THROUGH XRD	188
APPENDIX B TEM DIFFRACTION INTENSITY EVALUATION OF FCC AND $L1_0$ FePt PHASES	192
LIST OF REFERENCES	196

LIST OF FIGURES

Figure 1.1 The phase diagram of Fe-Pt.....	4
Figure 1.2 Ball-and-stick models of unit cells of (a) ordered $L1_0$ FePt; (b) disordered fcc FePt; (c) ordered $L1_2$ FePt ₃ ; and (d) ordered $L1_2$ Fe ₃ Pt.....	5
Figure 1.3 Schematic of an inductive read / wire head and a GMR read head.....	10
Figure 1.4 Illustration of grains, the randomness of easy-axis orientations, and the bit boundary in longitudinal recording.....	11
Figure 1.5 A schematic of a fully magnetized sample composed of microscopic dipoles.....	17
Figure 1.6 Partial B-H loop showing contours of constant B-H in second quadrant.....	18
Figure 1.7 The ideal demagnetization field H and magnetization M for $(BH)_{max}$	20
Figure 1.8 The $(BH)_{max}$ with magnetization M	20
Figure 1.9 The $(BH)_{max}$ with the demagnetizing field H	21
Figure 1.10 The road map of $(BH)_{max}$ product of hard magnets.....	23
Figure 1.11 Illustration of spring exchange behavior near the hard magnet / soft magnet interface. It indicates that the exchange coupling is very sensitive to the distance.....	25
Figure 1.12 Hysteresis loops of spring exchange coupled (a) & uncoupled (b) magnets.....	27
Figure 1.13 The illustration of the influence of “edge effect” on the volume fraction of product phase. The filled circles indicate the nucleated product phase. The absent of neighboring nuclei (A, B, C, D, and E) in thin film (b), as compared to the bulk sample (a), decreases the volume fraction of product phase.....	38
Figure 3.1 A schematic view of a modified tube furnace.....	50

Figure 3.2 The relative orientation of samples, Si wafer, and crucible.	51
Figure 3.3 A typical RBS spectrum of FePt film on SiO ₂ /Si substrate. The red line is the simulation curve, and the dark line is the as-acquired spectrum.	53
Figure 3.4 (a) diffraction pattern of polycrystalline Cu films; (b) HCDF-TEM with ideal objective aperture; (c) practical operation for HCDF-TEM.	56
Figure 3.5 A high contrast Cu TEM image with the HCDF-TEM mode	57
Figure 3.6 A typical XRR spectrum of [Fe/Pt] _n multilayer films	60
Figure 4.1 The BF XTEM images of sample [Fe _{22nm} /Pt _{28nm}] ₆ . (a) as-deposited, (b) annealed at 350°C 10 minutes, and (c) annealed at 350°C 20 minutes. The bright stripes represent Fe (or solution) layer, and the dark stripes indicate Pt (or Pt solution).	66
Figure 4.2 (a) The HAADF STEM image of the sample annealed at 350C for 10 minutes, (b) the EDX in the middle of the Fe layer, and (c) the EDX in the middle of the Pt layer.	68
Figure 4.3 The possible <i>fcc</i> FePt formation mechanisms. (a) Gradual penetration of Fe atoms into Pt grains, which is not supported by the published diffusivities; (b) Re-nucleation of <i>fcc</i> FePt grains and growth by “discontinuous dissolution” via grain boundary diffusion.	69
Figure 4.4 HCDF TEM image of sample [Fe _{22nm} /Pt _{28nm}] ₆ annealed at 350°C for 20 minutes. The image was formed using the 001 and 110 reflections of <i>L1₀</i> FePt phase. The illuminated <i>L1₀</i> FePt phase grains are circled out to be differentiated from the CCD noise in pixel size.	71
Figure 4.5 (a) The M-H hysteresis curve, and (b) the Henkel plot of δm of sample [Fe _{22nm} Pt _{28nm}] ₆ after annealed at 350°C 20 minutes.	73
Figure 5.1 Portion of a TEM SADP of a film containing both ordered <i>L1₀</i> and disordered <i>fcc</i> FePt phases.	83

Figure 5.2 The (a) bright field, (b) HCDF($\{200_{L10+fcc}\}+201_{L10}+112_{L10}$), (c) HCDF(001_{L10}), (d) HCDF($201_{L10}+112_{L10}$), (e) contrast selected HCDF($\{200_{L10+fcc}\}+201_{L10}+112_{L10}$), and (f) processed binary TEM images of a typical multilayer sample annealed at 500°C for 30 minutes. In the processed image, the light grey level grains indicate $L1_0$ phase grains with 001 planes illuminated, and the dark grains indicates all fcc grains with $\{200\}$ family planes illuminated, as well as the $L1_0$ grains with 200 or 020 planes illuminated. 89

Figure 5.3 XRD of standard Si powder 93

Figure 5.4 The intensity ratio of calculated and measured Si peaks, after normalized at the peak intensity of all peaks with refers to Si (111) peak. 95

Figure 5.5 The XRD of a reference highly ordered FePt film. The long –range order parameter was characterized to be 0.92 ± 0.05 96

Figure 5.6 XRR of the as-deposited and annealed samples “ML_PDT_11”, “ML_PDT_21”, “ML_PDT_43”, “ML_PDT_86”, and “ML_PDT_172” deposited at 250°C with different periodicity. 104

Figure 5.7 The decay of the first satellite peak due to annealing for sample “ML_PDT_86” annealed at 325°C. 106

Figure 5.8 The $\ln(I(t)/I(0))$ versus annealing time for samples “ML_PDT_21”, “ML_PDT_43”, and “ML_PDT_86”. 106

Figure 5.9 (a) The $\ln(D_A)$ versus $(1/T)$ for samples “ML_TMP_N50”, “ML_TMP_25”, and “ML_TMP_200”. (b) The $\ln(D_A)$ versus $(1/T)$ for samples “ML_PDT_21”, “ML_PDT_43”, and “ML_PDT_86”. D_A has the unit of m^2/s 108

Figure 5.10 Plan view HCDF TEM images of the sample “ML_PDT_172”, $[\text{Fe}_{71}\text{ÅPt}_{101}\text{Å}]_3$, annealed at different temperatures..... 111

Figure 5.11 (a) shows the location of $L1_0$ phase grains on a network of visible grain boundaries traced from the enlarged HCDF image (Figure 5.11 c) and the bright filed image at the same view (Figure 5.11 b) for sample “ML_PDT_172” annealed at 500°C for 30 minutes..... 111

Figure 5.12 (a) to (e) The plan view HCDF TEM images from $L1_0$ 001 and 110 superlattice reflections of samples “ML_TMP_N50”, “ML_TMP_25”, “ML_TMP_150”, “ML_TMP_200”, and “ML_TMP_250” annealed at 400°C for 30minutes, respectively. . 112

Figure 5.13 The measured grain size of $L1_0$ FePt phase versus the deposition temperature for samples “ML_TMP_N50” ~ “ML_TMP_250” annealed at 400 °C for 30 minutes. 113

Figure 5.14 (a) to (e) plan view HCDF TEM images of samples “ML_PDT_11” to “ML_PDT_172” annealed at 400°C for 30minutes from 001 and 110 superlattice diffraction rings. 114

Figure 5.15 The measured grain size of $L1_0$ FePt phase versus the periodicity for samples “ML_PDT_11” ~ “ML_PDT_172” annealed at 400°C for 30minutes..... 115

Figure 5.16 The TEM diffraction pattern of a slightly textured Cu film examined (a) 0 tilted, and (b) 19.5 degree tilted condition. The diffractions rings were indexed as 111, 200, 220, 311, 222 starting from the center..... 118

Figure 5.17 The TEM diffraction pattern of a sample “ML_PDT_172”, annealed at 500°C for 30 minutes and examined at (a) 0 tilted, and (b) 19.5 degree tilted condition. 119

Figure 5.18 shows the XRD of sample “ML_TMP_N50”, “ML_TMP_25”, “ML_TMP_150”, “ML_TMP_200”, and “ML_TMP_250” annealed at 400 °C for 30 minutes, from the top to bottom sequentially..... 121

Figure 5.19 shows the XRD of sample “ML_PDT_11”, “ML_PDT_21”, “ML_PDT_43”, “ML_PDT_86”, and “ML_PDT_172” annealed at 400 °C for 30 minutes, from the top to bottom sequentially..... 122

Figure 5.20 (a) the c/a ratio versus deposition temperature for samples “ML_TMP_N50”, “ML_TMP_25”, “ML_TMP_150”, “ML_TMP_200”, and “ML_TMP_250” annealed at 500°C for 30 minutes. (b) the c/a ratio versus periodicity for samples “ML_PDT_11”, “ML_PDT_21”, “ML_PDT_43”, “ML_PDT_86”, and “ML_PDT_172” annealed at 400°C for 30 minutes. The c/a ratio was determined from the superlattice reflections of Ll_0 FePt phase in the XRD patterns. 123

Figure 5.21 The measured value of S versus (a) the deposition temperature and (b) the periodicity of two sets of samples annealed at 400°C for 30 minutes. 124

Figure 5.22 The measured volume fraction of Ll_0 FePt phase versus (a) the deposition temperature and (b) the periodicity of two sets of samples annealed at 400°C for 30 minutes. 127

Figure 5.23 The measured Ll_0 FePt phase nuclei/grain density versus (a) the deposition temperature and (b) the periodicity of two sets of samples annealed at 400°C for 30 minutes. 128

Figure 5.24 (a) The M-H curves, and (b) the in-plane H_c versus the deposition temperature for samples “ML_TMP_N50”, “ML_TMP_25”, “ML_TMP_150”, “ML_TMP_200”, and “ML_TMP_250”. All samples were annealed at 400°C for 30 minutes. 130

Figure 5.25 (a) The M-H curves, and (b) the in-plane H_c versus the periodicity for samples “ML_PDT_11”, “ML_PDT_21”, “ML_PDT_43”, “ML_PDT_86”, and “ML_PDT_172”. All samples were annealed at 400°C for 30 minutes. 131

Figure 5.26 The in-plane coercivity versus the $L1_0$ FePt volume fraction of two set of samples with varying substrate temperature (“ML_TMP_N50” to “ML_TMP_250”) and bi-layer periodicity (“ML_PDT_11” to “ML_PDT_172”). All samples were annealed at 400°C for 30 minutes..... 134

Figure 5.27 The coercivity versus periodicity for a set of samples with varying periodicity at room temperature..... 137

Figure 5.28 A schematic to demonstrate the different growth rates of $L1_0$ FePt grains..... 140

Figure 6.1 (a) to (e) are the plan view HCDF TEM images using 001 and 110 reflections of $L1_0$ FePt phase for samples “ML_THK_8”, “ML_THK_25”, “ML_THK_50”, “ML_THK_73”, and “ML_THK_100” annealed at 400 °C for 1 hour, respectively. 146

Figure 6.2 (a) to (e) are the plan view HCDF TEM images using 001 and 110 reflections of $L1_0$ FePt phase for samples “ML_THK_8”, “ML_THK_25”, “ML_THK_50”, “ML_THK_73”, and “ML_THK_100” annealed at 500 °C for 1 hour, respectively. 147

Figure 6.3 (a), (b), (c), and (d) shows the BF, HCDF TEM images from $(001+110)_{L1_0}$, $(201+112)_{L1_0}$, and $(201+112)_{L1_0} + \{200 + 220\}_{fcc+L1_0}$ reflections of sample “ML_THK_100” annealed at 500°C for 1 hour. The same CCD integration time (32 seconds) is applied. A

much lower illumination intensity of $(201+112)_{L1_0}$ grains compared to that of $(001+110)_{L1_0}$ grains or $\{200+220\}_{fcc+L1_0}$ is well demonstrated.....	148
Figure 6.4 The $L1_0$ FePt phase fraction of versus film thickness for samples “ML_THK_8”, “ML_THK_25”, “ML_THK_50”, “ML_THK_73”, and “ML_THK_100” annealed at 400 °C and 500 °C for 1 hour.....	149
Figure 6.5 The XRD patterns of samples “ML_THK_25”, “ML_THK_50”, “ML_THK_73”, and “ML_THK_100” annealed at 400 °C for 1 hour.....	150
Figure 6.6 The long-range order parameter of samples “ML_THK_25”, “ML_THK_50”, “ML_THK_73”, and “ML_THK_100” annealed at 400 °C for 1 hour.....	151
Figure 6.7 The a) M-H curves and b) in-plane coercivity versus film thickness for samples “ML_THK_8”, “ML_THK_25”, “ML_THK_50”, “ML_THK_73”, and “ML_THK_100” annealed at 400 °C for 1 hour.	152
Figure 6.8 The M-H curves of (a) sample co-sputtered FePt film “ML_THK_100” and multilayer film “A1_THK_100” annealed at different temperature for one hour.	154
Figure 6.9 (a) to (f) are the plan view HCDF TEM images using 001 and 110 reflections of $L1_0$ FePt phase for samples “A1_THK_7”, “A1_THK_25”, “A1_THK_50”, “A1_THK_73”, “A1_THK_100”, and “A1_THK_200” annealed at 400 °C for 1 hour, respectively.....	155
Figure 6.10 (a) to (f) are the HCDF TEM images using 001 and 110 reflections of $L1_0$ FePt phase for samples “A1_THK_7”, “A1_THK_25”, “A1_THK_50”, “A1_THK_73”, “A1_THK_100”, and “A1_THK_200” annealed at 500 °C for 1 hour, respectively.....	156

Figure 6.11 A comparison of measured Ll_0 FePt phase grain size in $[\text{Fe}/\text{Pt}]_n$ multilayer films (“ML_THK_8” to “ML_THK_100”) and FePt alloy films (“A1_THK_7” to “A1_THK_200”) annealed at 400°C for 1 hour. 156

Figure 6.12 The Ll_0 FePt phase fraction of versus film thickness for FePt alloy samples (“A1_THK_7” to “A1_THK_200”) and $[\text{Fe}/\text{Pt}]_n$ multilayer films (“ML_THK_8” to “ML_THK_100”) annealed at 400 °C for 1 hour. 157

Figure 6.13 A comparison of measured Ll_0 FePt phase nuclei/grain density in $[\text{Fe}/\text{Pt}]_n$ multilayer films (“ML_THK_8” to “ML_THK_100”) and FePt alloy films (“A1_THK_7” to “A1_THK_200”) annealed at 400°C for 1 hour. 158

Figure 6.14 The c/a ratio versus film thickness for samples “A1_THK_7”, “A1_THK_25”, “A1_THK_50”, “A1_THK_73”, “A1_THK_100” and “A1_THK_200” annealed at 400 °C for 1 hour. 159

Figure 6.15 The (a) M-H curves, and (b) the coercivity of samples “A1_THK_7” to “A1_THK_200” annealed at 400 °C for 1 hour. As a comparisons, the coercivities of annealed $[\text{Fe}/\text{Pt}]_n$ multilayer films (“ML_THK_8” to “ML_THK_100”) were also included. 160

Figure 6.16 (a) to (f) shows the BF TEM images of samples “A1_THK_7” (7 nm), “A1_THK_25” (25 nm), “A1_THK_50” (50 nm), “A1_THK_73” (73 nm), “A1_THK_100” (100 nm), and “A1_THK_200” (200 nm) annealed at 400 °C for 1 hour, respectively. 162

Figure 6.17 A schematic showing the relative energy of $[\text{Fe}/\text{Pt}]_n$ multilayers, FePt alloys, and order Ll_0 phase. Point “A” indicates the Gibbs free energy of $[\text{Fe}/\text{Pt}]_n$ multilayer films. Point “B” indicates the Gibbs free energy of disordered *fcc* FePt alloy films, and point “C”

indicates the Gibbs free energy of ordered $L1_0$ FePt samples. Point “A”, “B”, and “C” indicate the energy of samples with the same average composition of $Fe_{50}Pt_{50}$ 164

Figure 7.1 M-H loops of samples listed in table 7.2. The Fe thickness (t) was (a) t=1 nm; (b) t=2 nm; (c) t=3 nm; (d) t=4 nm; (e) t=5 nm; (f) t=6 nm. The samples with Fe thicker than 6 nm have similar M-H loops as (f). 171

Figure 7.2 M-H of samples listed in table 7.3. The Fe thickness (t) was (a) t=1 nm; (b) t=2 nm; (c) t=3 nm; (d) t=4 nm; (e) t=5 nm; (f) t=6 nm; (g) t=7 nm; (h) t=8 nm. The samples with Fe thicker than 8 nm have similar M-H loops as (h). 172

Figure 7.3 The M-H loops of as-deposited and 400°C annealed sample “ML_MGT_50”. The red dot in the figure indicates the position of the $(BH)_{max}$ 175

Figure 7.4 The M-H hysteresis loops of sample “ML_MGT_50” annealed at (a) 300°C for 1 hour, (b) 350°C for 1 hour, (c) 400°C for 15 minutes, and (d) 400°C for 60 minutes. The red spots on the curve shows the position of $(BH)_{max}$ 177

Figure 7.5. The M-H hysteresis loops of sample (a) “ML_MGT_56”; (b) “ML_MGT_59”; (c) “ML_MGT_61”; and (d) “ML_MGT_68” annealed at 400°C for 60 minutes. The red spots on the curve shows the position of $(BH)_{max}$ 179

LIST OF TABLES

Table 1.1 A list of commonly used high K_u materials	6
Table 1.2 Hard magnetic properties of commercially available permanent magnets.....	22
Table 5.1 The reflections along with the contributing planes.....	84
Table 5.2 The calculated and measured XRD peaks of Si powders	94
Table 5.3 The calculated 001 and 002 XRD peaks of $L1_0$ Fe ₅₀ Pt ₅₀ (S=1).....	96
Table 5.4 A list the [Fe/Pt] _n multilayer films.....	102
Table 5.5 The diffusivities measured and the Arrhenius expressions	109
Table 5.6 A summary of measured structure and properties of samples	134
Table 5.7 A list the [Fe/Pt] _n multilayer films.....	137
Table 7.1 A review of $L1_0$ FePt based exchange spring magnets.....	167
Table 7.2 A set of samples with varying thickness of Fe deposited on 73 nm $L1_0$ FePt films. The $L1_0$ FePt film was achieved by annealing the stoichiometric [Fe/Pt] _n multilayer samples, “ML_THK_73”, at 450 °C for 30 minutes.	170
Table 7.3 A set of samples with varying thickness of Fe deposited on highly ordered $L1_0$ FePt films. The $L1_0$ FePt film was achieved by annealing the stoichiometry [Fe/Pt] _n multilayer samples (“ML_THK_73”) at 700 °C for 30 minutes.....	172
Table 7.4 A list of samples with varying composition	174
Table 7.5 A summary of magnetic properties of sample “ML_MGT_50” annealed at different conditions.....	178
Table 7.6 The saturation magnetization (emu/cc) of annealed samples	180

Table 7.7 The coercivity (kOe) of annealed samples	180
Table 7.8 The energy product (MGOe) of annealed samples	181

LIST OF ACRONYMS/ABBREVIATIONS

\tilde{D}_0	Interdiffusivity of bulk diffusion couples
f_0	Attempt frequency of magnetization reversion
k	Coefficient between the change of free energy and compositional gradient
τ	Required storage time
ϕ_0	Amplitude of the direct beam
ξ_0	Extinction distance for the direct beam
θ_B	Bragg angle
$(BH)_{max}$	Energy product
ϕ_g	Amplitude of diffracted beam
ξ_g	Extinction distance for the diffracted beam
A	Absorption factor
$A(t)$	Amplitude of composition modulation at time t
AGFM	Alternating Gradient Force Magnetometer
A_h	Exchange constants of the hard phase
B	Flux density or magnetic induction
bcc	Body-centered cubic
BF	Bright field
B_r	Remnant magnetization
DC	Direct current
DF	Dark field

D_{Λ}	Effective interdiffusivity
EDX	Energy dispersive X-ray spectrum
F	Structure factor
f'	Helmholtz free energy
fcc	face-centered cubic
f_i	Atomic scattering factor for electron beams
f_0	Attempt frequency for thermal magnetic reversal
FIB	Focused ion beam
f_{LI_0}	Volume fraction of LI_0 FePt phase
GMR	Giant magnetoresistive
H	External magnetic field
HAADF	High angular annular dark field
HCDF	Hollow cone dark field
H_m	Reverse field
HRTEM	High resolution transmission electron microscopy
I	Peak intensity of XRD
JH_c	Internal coercivity
K_1	The first order of magnetocrystalline anisotropy energy density
k_B	Boltzmann constant
K_h	Anisotropy constants of the hard phase
K_u	magnetocrystalline anisotropy energy density
M	Magnetization

MEMS	Micro-electro-mechanical-systems
M_s	Saturation magnetization
p	Multiplicity factor
RBS	Rutherford backscattering spectrometry
RF	Radio frequency
RT	Room temperature
s	Excitation error
S	Long-range order parameter
SADP	Selected area diffraction pattern
S_{eff}	Effective excitation error
SNR	Signal-to-noise ratio
STEM	Scanning transmission electron microscopy
T	Storage time
T	Temperature
T_c	Curie temperature
TEM	Transmission electron microscopy
TMR	Tunneling magnetoresistive
V	Grain Volume
V_c	Volume of a unit cell
XRD	X-ray diffraction
XRR	X-ray reflectometry
XTEM	Cross sectional transmission electron microscopy

z	Distance along the optic axis
δ_h	Width of a domain wall in the hard phase
λ	Wavelength
μ	Linear absorption coefficient
Λ	Bi-layer period

CHAPTER 1 INTRODUCTION AND BACKGROUND

1.1 $L1_0$ FePt and Fe-Pt system

In the recent years, $L1_0$ FePt thin films have stimulated much research interest because of their potential applications as high-density magnetic recording medium and permanent magnets due to the large magnetocrystalline anisotropy energy density ($K_u \sim 10^7$ ergs/cm³) of the $L1_0$ phase [Skomski (2003)]. The $L1_0$ FePt is an ordered intermetallic phase composed of Fe and Pt, with a stoichiometric composition of 50 at. % Fe and 50 at. % Pt, as shown in the Fe-Pt phase diagram (Figure 1.1) [Massalski et al. (1990)]. In bulk form, this phase is thermodynamically stable at temperatures below 1300 °C. At higher temperature, the disordered face-centered cubic (*fcc*) phase becomes more stable because its larger entropy provides a lower Gibbs free energy. This disordered *fcc* FePt phase has a low magnetic anisotropy energy, without any attractive hard magnetic properties. Ball-and-stick models of the ordered $L1_0$ FePt and disordered *fcc* FePt unit cells are shown in Figure 1.2 (a) and (b), respectively.

The $L1_0$ FePt phase achieves its large magnetocrystalline anisotropy energy density mainly from the Fe-Pt interactions and its lattice structure. The magnetocrystalline anisotropy is the energy that causes a preferred alignment of magnetic moments in a specific crystallographic orientation. The origin of this energy is from the Fe and Pt interactions originating from spin-orbit coupling and the hybridization between Fe *3d* and Pt *5d* states [Burkert et al. (2005); Brown et al. (2003); Kitakami et al. (2003); Staunton et al. (2004)]. The spin-orbit coupling is of tremendous importance for a host of magnetic phenomena that are key to most applications of magnetic materials. These

phenomena include the magnetocrystalline anisotropy, magnetostriction, magneto-optic effects, anisotropic magnetoresistance, ferromagnetic Hall effect, and magnetic resonance damping [O'Handley (1999)].

A simple understanding of the spin-orbit interaction is given below. In a classical understanding, condensed material is composed of a lattice of positively charged nuclei and surrounding electrons. The positive nucleus lattice generates a crystal field anisotropy and a magnetic field. The lower the crystal structure symmetry, the higher the crystal field anisotropy. This crystal field anisotropy strongly influences the preferred orientation of the spin magnetic moment of the moving electrons, which causes the spin-orbit interaction. As to the $L1_0$ FePt phase structure, it is distorted along the “ c ” axis, and has a lower lattice symmetry (or higher crystal field anisotropy) than that of the disordered fcc FePt phase. Consequently, the “ c ” axis of $L1_0$ FePt phase is the preferred direction of magnetization (or called easy axis), and “ a ” and “ b ” directions are the hard axes. The significance of magnetocrystalline anisotropy energy on magnetic recording and exchange spring magnets will be given in following sections.

Table 1.1 lists typical materials with high magnetocrystalline anisotropy energy density (K_u) [Coey (2002); Fidler et al. (2004); Skomski et al. (2003); Weller et al. (2000)]. Three alloy groups can be classified. The Co-based alloys are widely used as thin film magnetic recording media, although strictly speaking, they do not have a large value of K_u compared to materials in the other two groups. The rare earth transition metals have been commonly used as permanent magnets in bulk forms [Coey (2002); Fidler et al. (2004)]. Recently, thin films of these materials with perpendicular magnetic anisotropy have also been reported for high-density magnetic recording [Sayama et al.

(2005); Sayama et al. (2007)]. A major disadvantage of these materials is their poor chemical stability, which limits their application. Another group with high K_u is the $L1_0$ materials which have been studied extensively. Different from rare earth transition metals, the $L1_0$ phases are studied mainly for thin film applications because of the large concentration of Pt or Pd involved, which makes the bulk form very expensive. Another attractive property of $L1_0$ FePt thin films, besides their high K_u , is their high chemical stability due to the Fe-Pt interactions as described above, which makes them especially useful for practical applications in solid-state devices and biomedicine [Sun et al. (2006)].

Although the $L1_0$ FePt thin film demonstrates very promising hard magnetic properties, it cannot be readily prepared. The FePt thin films or nanoparticles prepared near room temperature through sputtering [Coffey et al. (1995)], evaporation [Bian et al. (2000)], and wet chemical synthesis [Sun et al. (2000)] usually have the disordered phase. The main reason is that these thin film (including nanoparticles) fabrication methods generally are non-equilibrium and processed by rapid quenching of the atoms in vapor or liquid phase into the solid phase at room temperature. Consequently, the non-equilibrium phase, disordered fcc FePt, results from these fabrication methods. Because the disordered phase has no attractive magnetic properties, a disorder-order phase transformation of FePt is necessary. A detailed review of the preparation of $L1_0$ FePt thin films will be given in section 1.2.

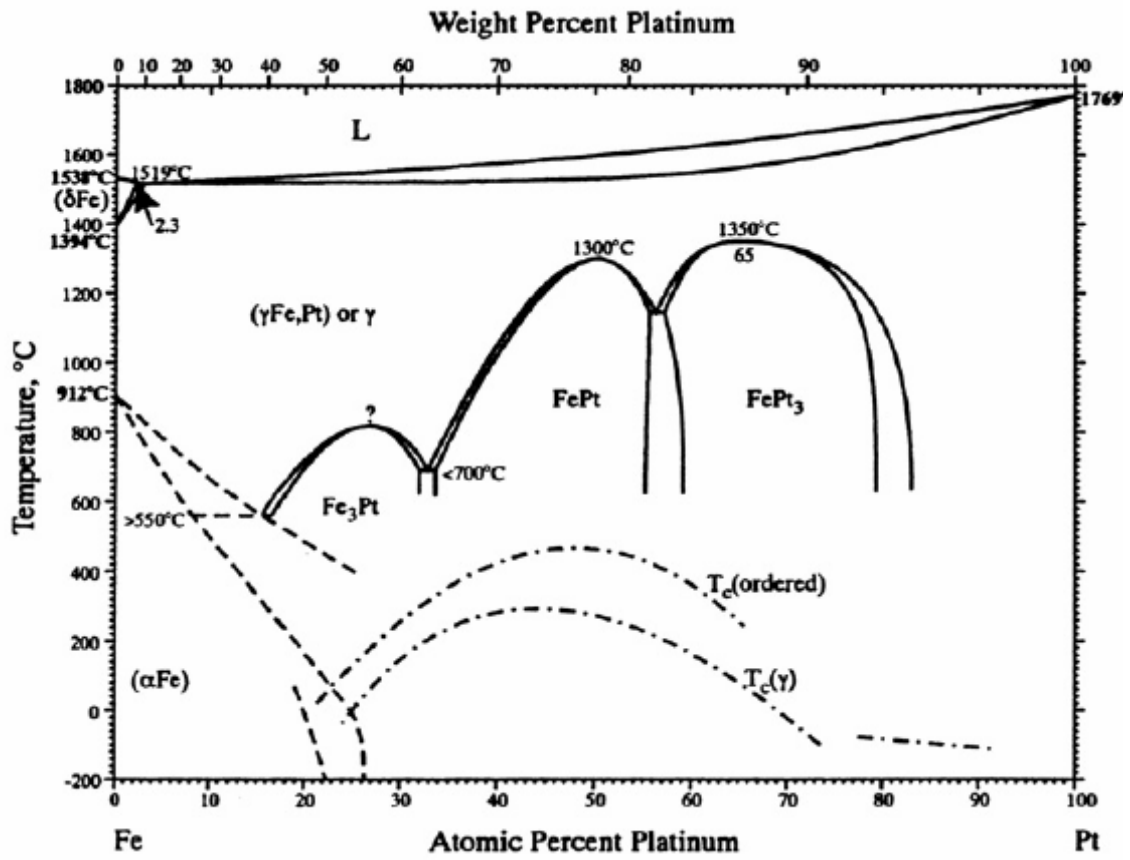
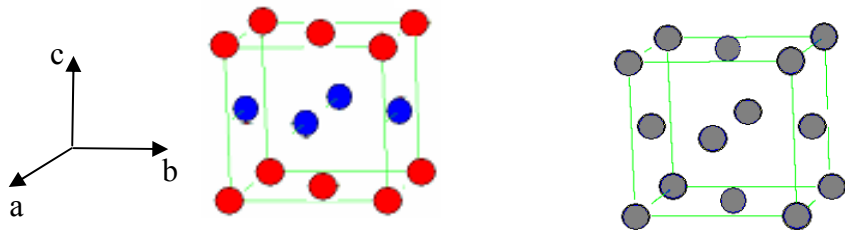
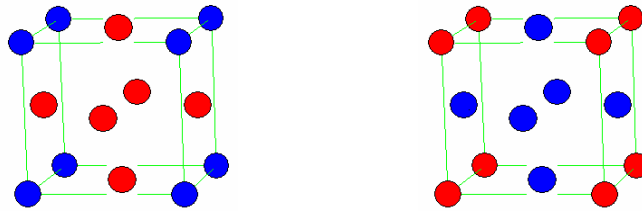


Figure 1.1 The phase diagram of Fe-Pt. [Massalski (1990)]



(a) ordered FePt ($L1_0$, $a=3.847\text{\AA}$ $c=3.715\text{\AA}$) (b) disordered FePt (fcc , $a=3.877\text{\AA}$)



(c) ordered FePt₃ ($L1_2$, $a=3.866\text{\AA}$)

(d) ordered Fe₃Pt ($L1_2$, $a=3.750\text{\AA}$)



Figure 1.2 Ball-and-stick models of unit cells of (a) ordered $L1_0$ FePt; (b) disordered fcc FePt; (c) ordered $L1_2$ FePt₃; and (d) ordered $L1_2$ Fe₃Pt.

[PDF 43-135; PDF 29-0716; PDF 27-071]

Table 1.1 A list of commonly used high K_u materials

[Coey (2002); Fidler et al. (2004); Skomski et al. (2003); Weller et al. (2000)].

Material system	Material	$\mu_0 M_s$ (T)	T_C (K)	K_I (MJ m ⁻³)	Minimum stable grain size as ferromagnets (nm)
Co and its alloys	CoPtCr	0.37	--	0.2	10.4
	Co	1.76	1404	0.45	8.0
	Co ₃ Pt	1.38	--	2.0	4.8
Rare earth transition metals	SmCo ₅	1.07	1003	17.0	2.2-2.7
	Sm ₂ Co ₁₇	1.20	1190	3.3	--
	Sm ₂ Fe ₁₇ N ₃	1.54	749	8.9	--
	Nd ₂ Fe ₁₄ B	1.61	585	5.0	3.7
$L1_0$ phases	FePt	1.43	750	6.6	2.8-3.3
	CoPt	1.00	840	4.9	3.6
	FePd	1.37	760	1.8	5.0

Other phases in the Fe-Pt system, except $L1_0$ FePt, do not possess a high magnetic anisotropy energy density and attractive hard magnetic properties. α -Fe at room temperature, having a body-centered cubic (*bcc*) structure, is commonly used as a soft magnet with large saturation magnetization and small anisotropy energy. The γ phase, also called disordered *fcc* FePt phase, shows a low value of K_u . In this thesis, the “disordered FePt phase” or “*fcc* FePt phase” will be used to indicate the solid solution with considerable concentration of Pt and Fe, while Pt or γ Fe will be used to represent pure Pt or pure γ Fe. Strictly speaking, the pure Pt, γ Fe, and disordered *fcc* FePt are different compositional ranges of the same *fcc* phase in the phase diagram. Ordered

Fe_3Pt and FePt_3 intermetallic phases have an $L1_2$ structure with a low K_u . The ball-and-stick models of ordered FePt_3 and ordered Fe_3Pt are shown in Figure 1.2 (c) and (d), respectively.

A large value of saturation magnetization is very important for magnetic materials. In the Fe-Pt system, the magnetization generally increases with the increase of Fe concentration. Therefore, pure Fe, Fe_3Pt , and the disordered *fcc* phase with large concentration of Fe have relatively large values of M_s . As will be discussed later, these soft phases are useful as the high- M_s soft phase to construct $L1_0$ FePt based exchange spring magnets.

1.2 $L1_0$ FePt material for thin film magnetic recording

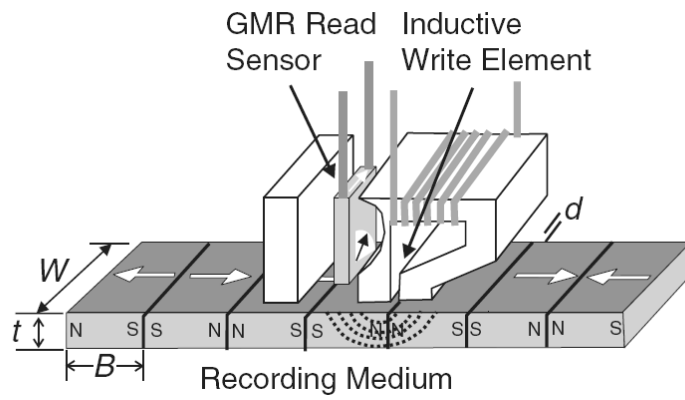
A brief introduction of thin film magnetic recording is helpful to understand the application of $L1_0$ FePt as a promising medium for next generation high-density magnetic recording. A schematic of thin film magnetic recording is shown in Figure 1.3, including longitudinal (Figure 1.3 a) and perpendicular recording (Figure 1.3 b) modes. The magnetic recording consists of “writing” and “reading” processes. The writing process involves passing a current (i.e., the signal to be recorded) through the coil of the head. This current generates a magnetic field which changes the magnetic state of the media according to the signal to be recorded. Another head based on giant magnetoresistive (GMR) or tunneling magnetoresistive (TMR) is used in the reading process. The GMR/TMR head shows a change of electrical resistance induced by the different alignment (parallel vs. anti-parallel) of the magnetic moment of a layer within the head that is induced by the residual moment of the recorded medium. It possesses the merits of very high signal-to-noise ratio (SNR) and high spatial resolution. The longitudinal and perpendicular recording modes have different set-up and physical principles [Piramanaya (2007); Richter (1999); Moser et al. (2002)]. In longitudinal recording technology, the magnetizations that lie longitudinally (in the film plane) are used to store the information. This technology has been used since IBM’s first hard disk drive in the late 1950s. For about half a century, the longitudinal recording density has increased dramatically from about 10^{-3} Mbits/in² to 10^5 Mbits/in² [Grochowski]. An alternative technology, perpendicular recording in which magnetizations lie perpendicular to the disk surface was proposed in the late 1970s to overcome some of the potential problems of longitudinal

recording [Iwasaki et al. (1977); Iwasaki et al. (1979); Iwasaki (1980)]. Only in the past several years, however, has the research on perpendicular recording media been intense and received the attention of industry researchers worldwide [Piramanaya (2007)]. The main reason for the current interest comes from the need to find an alternative technology to get away from the superparamagnetic limit faced by the longitudinal recording which will be explained later. Another reason comes from the progress in some of the materials and techniques used in perpendicular recording. Today, most hard disk drive products are using perpendicular recording. A detailed review on the physics and progress of these techniques can be found in the references [Piramanaya (2007); Rithter (1999); Moser et al. (2002)].

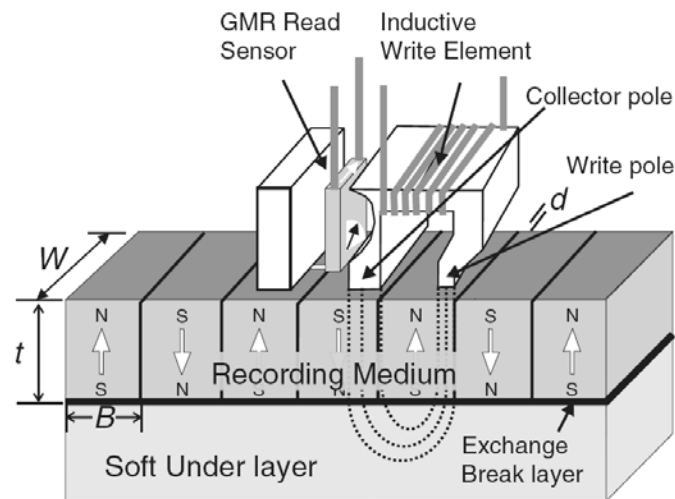
For both recording modes, the signal-to-noise ratio (SNR) is a key indicator of the performance of a recording medium. As shown in Figure 1.3, the change of magnetization direction between two neighboring magnetized bits can be used to represent the bit “1”, and the absence of the change represents the bit “0”. The SNR indicates how reliably the bits can be read out at a certain linear density, which has a relation with the number of grains in a bit (N).

$$SNR = 10 \log(N) \quad (1.1)$$

Equation 1.1 indicates that increasing the number of grains would help increase the SNR. One illustration of grains, with the easy-axis orientation of each grain and the bit boundary is shown in Figure 1.4. To keep an acceptable SNR, one bit is usually composed of hundreds of grains.



(a)



(b)

Figure 1.3 Schematic of an inductive read / wire head and a GMR read head

[Moser et al. (2002)].

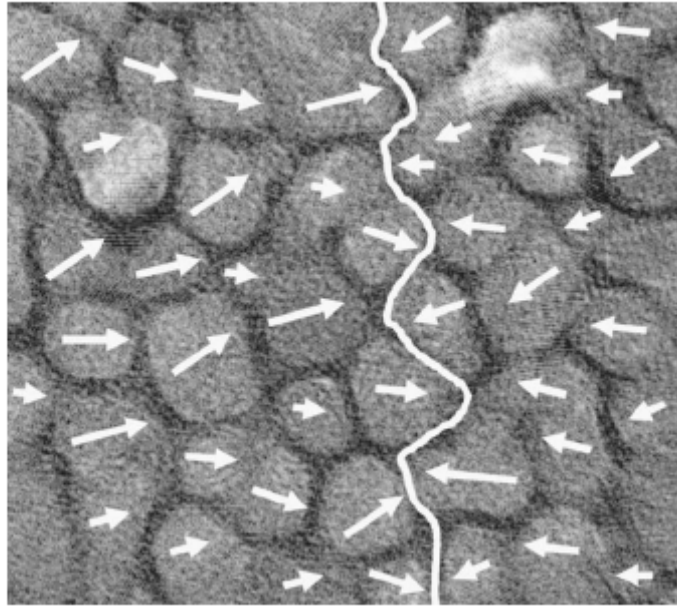


Figure 1.4 Illustration of grains, the randomness of easy-axis orientations, and the bit boundary in longitudinal recording. [Piramanaygam (2007)]

There are many technical issues to resolve to increase the magnetic recording density, however, in all cases it is required to decrease the bit size. Two approaches may be used to decrease the bit size. One is to use fewer grains for each bit, and the other is to decrease the grain size. The use of fewer grains for one bit will unavoidably decrease the SNR, and decreasing the grain size will decrease the thermal stability of magnetization, as will be explained later. Therefore, the design of magnetic recording is generally a “trilemma” among recording density, SNR, and thermal stability. The selection of a higher K_u material is of interest as it allows an increase in the thermal stability of smaller grains for the high-density recording.

The thermal stability of a recording medium refers to its ability to resist the unintended thermal reversal of the magnetized grains, and the Arrhenius-Néel model is commonly used to describe this phenomenon. Equation (1.2) gives the expression of storage time without considering the demagnetizing field [Néel (1949)].

$$\tau = |\ln x| \tau_0 \exp\left(\frac{K_u V}{k_B T}\right) \quad (1.2)$$

where τ is the required storage time. $\tau_0 = 1/f_0$ and f_0 is an “attempt frequency” usually taken as ($\sim 10^9$ Hz) [Brown (1979)]. x is the fraction of the retained magnetization. K_u is the magnetocrystalline anisotropy energy density and V is the volume of each grain, thus $K_u V$ is the magnetocrystalline anisotropy energy, which keeps the magnetic moment oriented along the recorded easy axis direction and prevents the reversal of the moment. $k_B T$ is the thermal energy, which plays a role to reverse the magnetization (thus to erase the recorded information on the disk). As an example, if the required storage time is 10 years ($\sim 10^8$ s) and the percentage loss of data amplitude is 5%,

$$\frac{K_u V}{k_B T} \approx 43$$

From this equation, it can be seen that if the grain size is too small, the thermal energy ($k_B T$) will be substantial compared to the anisotropy energy ($K_u V$), and the recorded magnetization can be reversed easily. Such a phenomenon, where the magnetic particles could reverse their magnetization without any external field, is called superparamagnetism. Table 1.1 lists the minimal thermally stable grain size for the recording of most commonly investigated high K_u materials under industrially specified working condition and storage time. The CoCrPtX alloy (X=B, Ta) used in longitudinal

magnetic recording has a grain size of about 9 nm [Moser et al. (2002), Weller et al. (2000)]. To further increase the recording density by decreasing the grain size, a high K_u material is highly desirable. For this reason, $L1_0$ FePt has attracted research attention. The preliminary recording experiments have demonstrated that 4 nm $L1_0$ FePt nanoparticles show high anisotropy without the superparamagnetism phenomenon, which suggests that it is a very good candidate medium for the recording density in Tbits/in² scale [Sun et al. (2000)].

The practical use of FePt media is hindered by several problems that must be solved. These problems include:

- 1) high formation temperature of ordered phase
- 2) control of crystallographic orientation to provide perpendicular magnetic anisotropy
- 3) high media noise
- 4) coercivity (H_c) too high to write with current head technology

The decrease of kinetic formation temperature will be reviewed in detail later, and the other three problems will be briefly introduced here. To realize a perpendicular anisotropy film, it is required to align the easy axis (“c” axis for $L1_0$ FePt) of the grains normal to the film plane. This orientation is needed for perpendicular magnetic recording. Such textured films have been successfully prepared by using MgO [Farrow et al. (1996); Thiele et al. (1998)] or Al₂O₃ substrates [Visokay et al. (1995); Chou et al. (2004)]. Media noise of FePt films can be attributed to the magnetic exchange interaction between grains, a large grain size distribution, a distribution of grain anisotropies, and a variation of grain orientations. The media noise can not be avoided, but can be reduced. For example, a non-magnetic matrix (i.e., C, SiO₂, Al₂O₃, Si₃N₄)

used to separate the magnetic FePt grains or particles can effectively decrease the exchange coupling between them. Small $L1_0$ FePt nanoparticles (<10 nm) with a very small grain size distribution have been prepared with wet-chemical synthesis, which is also helpful to decrease the noise [Sun et al. (2000)]. The development of a writing method on high- H_c media is another challenging task. The maximum magnetic field generated by a writing head is typically limited by the saturation magnetization of the head. Because of the high K_u of FePt ordered films, anisotropy field H_k (the upper limit of H_c) becomes as high as 10 MA/m [Shibata et al. (2003)], which is beyond the limit of all investigated write head materials to saturate. Some heat-assisted magnetic recording has been proposed to aid the writing of high anisotropy materials [Suzuki et al. (1998); Grober et al. (1997)]. In these methods, the medium temperature is increased by optical irradiation during writing so that the H_c of the medium can be decreased.

Decreasing the processing temperature needed to form $L1_0$ FePt films with small grains is another challenging task which partially drives the work of this dissertation. As described above, the FePt nanoparticles or thin films prepared by commonly used fabrication methods usually have the disordered fcc phase structure, which lacks any attractive hard magnetic properties because of its small magnetocrystalline anisotropy. Further ex-situ annealing at high temperature (>500°C) is typically used to achieve highly ordered $L1_0$ FePt phase through the disorder-to-order phase transformation. Such high temperatures are not compatible with the aluminum and glass substrates commonly used in hard disk drives. Furthermore, at such high annealing temperatures, grain growth and/or particle agglomeration will occur along with the phase transformation, which prevents the achievement of small ordered $L1_0$ FePt nanoparticles for high-density

recording. Many approaches have been proposed to solve this problem and are described below.

- 1) Deposition of FePt films on heated substrates is one approach to nucleate the $L1_0$ FePt phase. Compared to the ex-situ annealing, the substrate temperature is usually lower [Suzuki et al. (2001); Huang et al. (2002); Takahashi et al. (2001)]. Although the $L1_0$ FePt phase was identified, the magnetic properties of films deposited at lower temperatures are generally poor, which indicates that the films either have a low ordering (i.e., small long range order parameter) or are only partially ordered (i.e., a small volume phase fraction of ordered phase).
- 2) The irradiation [Cantelli et al. (2007); Wiedwald et al. (2007); Hasegawa et al. (2006)] of films before annealing is another approach to decrease the kinetic temperature. It is believed that the enhancement of the atomic diffusivity in the films is a benefit to the nucleation of $L1_0$ FePt phase.
- 3) The effects of ternary elements on the kinetic ordering temperature have been widely reported. These ternary elements may include Ag [Kang et al. (2002); Sato et al. (2003); Platt et al. (2002)], Au [Platt et al. (2002); Kang et al. (2003)], and Cu [Maeda et al. (2002); Platt et al. (2002); Wierman et al. (2003)]. Contrary conclusions have been reported as to the impact of Cu on the kinetic ordering temperature in FePt [Berry et al. (2005)]. For example, Platt et al. and Maeda et al. found that Cu aided in the transformation and attributed the enhanced ordering kinetics to an increased driving force for ordering. Takahashi et al. also observed that Cu aided in the ordering transformation but surmised that Cu lowers the melting point and therefore enhances the diffusivity of the alloy. Wierman et al. found that through

careful control of the Fe and Pt concentrations, Cu did not aid in the ordering transformation; however, altering the binary Fe/Pt ratio had a major impact on the transformation kinetics. The differential scanning calorimetry (DSC) conducted by Berry and Barmak demonstrate that Cu additions are found to be no more beneficial towards lowering the kinetic ordering temperature or driving force than equivalent additions of Fe (or reductions of Pt) [Berry et al. (2005)].

- 4) Another very interesting approach to achieve the $L1_0$ FePt at low temperature, which will be investigated in this dissertation, is through the solid state reaction of $[\text{Fe/Pt}]_n$ multilayer films. It has been widely reported that the ordered $L1_0$ FePt phase was found at a reduced annealing temperature (as low as 300°C) for both epitaxial [Verdier et al. (2005); Endo et al. (2001); Endo et al. (2003); Chou et al. (2004); Chou et al. (2004)] and polycrystalline [Luo et al. (1995); Reddy et al. (2006)] thin films. Although it is commonly accepted that the long distance diffusion is responsible for the low temperature nucleation of $L1_0$ FePt, the mechanism of the diffusion and reaction of $[\text{Fe/Pt}]_n$ films is still poorly understood. This fact partially motivates this study. The review of $[\text{Fe/Pt}]_n$ multilayer films will be given at the beginning of chapter 4, 5, 6, and 7 from different aspects.

1.3 $L1_0$ FePt based exchange-coupled permanent magnets

Another important application of $L1_0$ FePt is to fabricate exchange-coupled permanent magnets. Permanent magnets are unique in their ability to deliver magnetic flux into the air gap of a magnetic circuit without any continuous expenditure of energy. The reason that permanent magnets generate magnetic fields is because of the existence of free poles at the end surface, as shown in Figure 1.5, a schematic of a permanent magnet composed of microscopic dipoles. Inside the magnetic material, this field has an opposite direction of the magnetization, and it is called demagnetizing field. The energy due to the appearance of free poles at the end surface is the magnetostatic energy. Obviously, the properties of a permanent magnet are directly related to its magnetostatic energy density.

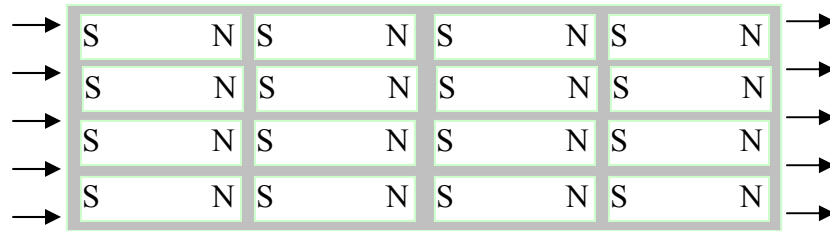


Figure 1.5 A schematic of a fully magnetized sample composed of microscopic dipoles.

In practice, the permanent magnet materials are characterized by their energy product, $(BH)_{max}$, where B is the flux density or magnetic induction, and H is the external magnetic field. The $(BH)_{max}$ product can be calculated from the second quadrant of the B- H_i loop (demagnetizing), as shown in Figure 1.6. The location of $(BH)_{max}$ is the point at which the material characteristics of a permanent magnet are most efficiently used. The

free poles at the end surface give rise to the magnetostatic energy, and the $(BH)_{max}$ is the maximum available magnetostatic energy density of a permanent magnet. Another very important term which strongly influences the demagnetizing field, demagnetizing factor N , is directly related to the sample shape.

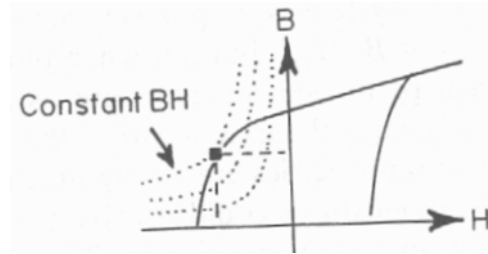


Figure 1.6 Partial B-H loop showing contours of constant B-H in second quadrant [O'Handley (1999)].

The maximum energy product, $(BH)_{max}$, of a magnet can be limited by its saturation magnetization (M_s), if $H_c \geq 2\pi M_s$, or limited by its coercivity (H_c), if $H_c \leq 2\pi M_s$.

The relationships will be derived below.

From $B = \mu_0(H+M)$, we have

$$BH = \mu_0(H+M)H$$

In the second quadrant during demagnetizing, M is positive, H is negative, and BH is also negative. If H only represents the magnitude of the magnetic field, above equation can be rewritten as

$$BH = \mu_0(M-H)(-H),$$

or

$$-BH = \mu_0HM - \mu_0H^2$$

While M is typically observed to decrease when the magnitude of the reversal field (H) is increased, a limiting case for a high H_c material can be explored by assuming no decrease in M . When M is a constant, $(BH)_{max}$ will be achieved when the derivative of above equation to H is 0.

$$\mu_0 M - 2\mu_0 H = 0 \rightarrow M = 2H \quad (1.3)$$

From this, we see that the ideal demagnetization field is given as $\frac{1}{2}$ the magnetization and that the maximum energy product is proportional to the square of the magnetization. The above equations used SI unit, and in CGS units, Equation (1.3) can be expressed as Equation (1.4)

$$H (Oe) = 2\pi M (M \text{ in } emu/cc) \quad (1.4)$$

The M is limited by M_s , and demagnetizing field H is limited by H_c . Therefore, when $H_c \geq 2\pi M_s$, the $(BH)_{max}$ is limited by the M_s , as Equation (1.5) in CGS units. In this case, further increase of the H_c is not helpful to increase the energy product.

$$(BH)_{max} (GOe) = (2\pi M)^2 (M \text{ in } emu/cc) \quad (1.5)$$

On the other hand, when $H_c \leq 2\pi M_s$, the $(BH)_{max}$ is limited by its coercivity, as Equation (1.6) in CGS units. In this case, further increase of the M_s is not helpful to increase the energy product.

$$(BH)_{max} (GOe) = H^2 (H \text{ in } Oe) \quad (1.6)$$

Equations (1.4) ~ (1.6) are also described with Figure 1.7, 1.8, and 1.9, respectively.

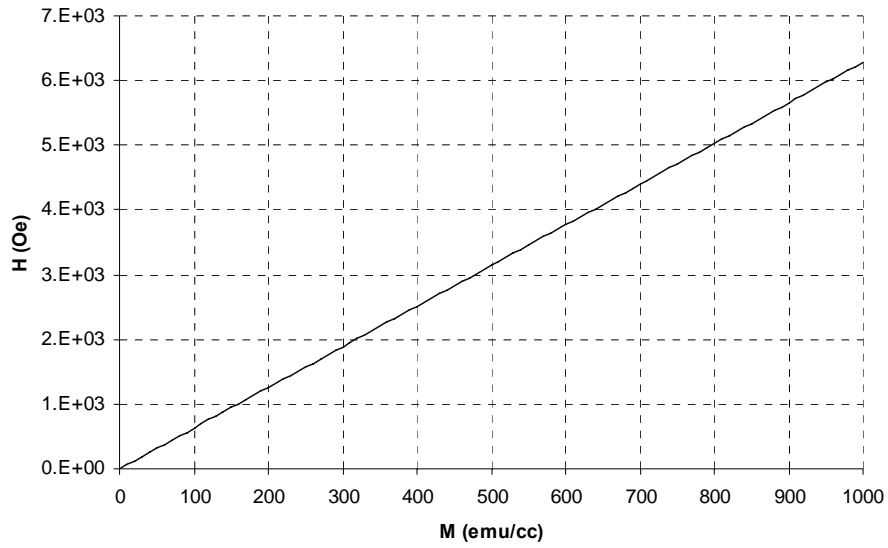


Figure 1.7 The ideal demagnetization field H and magnetization M for $(BH)_{max}$.

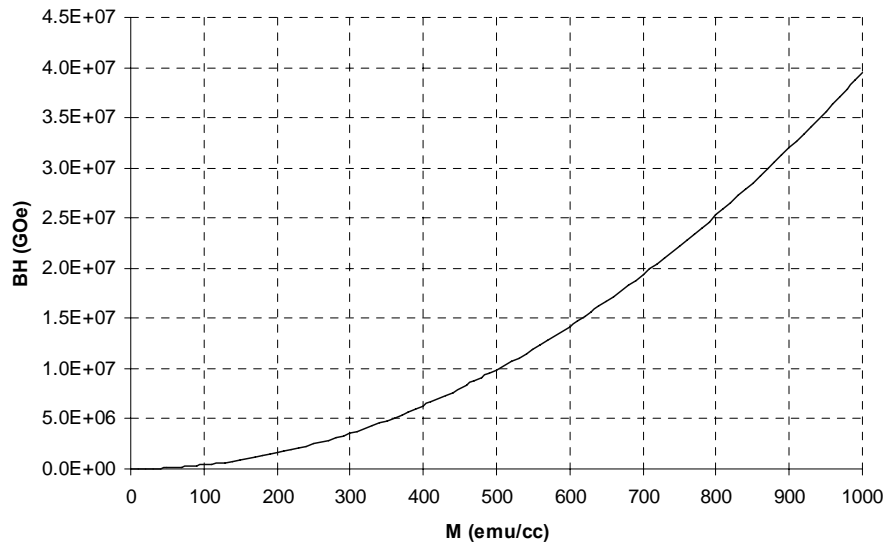


Figure 1.8 The $(BH)_{max}$ with magnetization M .

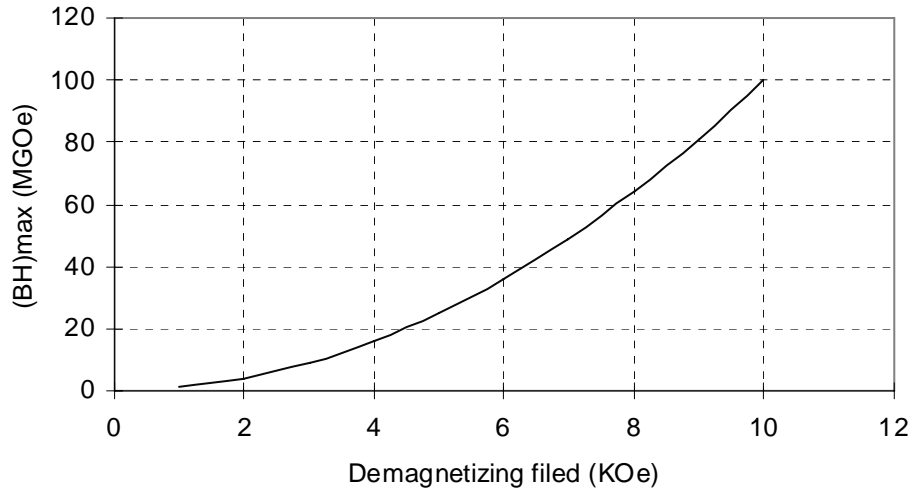


Figure 1.9 The $(BH)_{max}$ with the demagnetizing field H .

From above, it can be seen that a large $(BH)_{max}$ is given by

- 1) A large coercivity, to maintain a constant high magnetization (M) value in the presence of the demagnetizing field
- 2) A large M_s , which is the largest possible magnetization that the material might exhibit
- 3) A square hysteresis loop shape, maintaining the M_s value as ideally constant and equal to the maximum possible value for the material.

M_s is a property of the material which is sensitive to the composition, but not structure sensitive. The coercivity of a magnet is highly structure sensitive, but has an upper bound which is determined by the magnetic anisotropies present. For permanent magnets, the magnetocrystalline anisotropy energy is the most important one.

Permanent magnets have a very broad range of applications [Coey (2002); Fidler et al. (2004)]. The majority of applications are for the storage and transformation of various forms of energy, which include:

Mechanical energy \rightarrow electric energy (microphone, generator);

Electric \rightarrow mechanical energy (loudspeaker, motor);

Magnetic energy \rightarrow mechanical energy (coupling, bearing).

Another wide application is for the guidance of charged particles including hexapoles, magnetron sputtering, wave tubes, and magnetic lenses in many instruments (e.g., electron microscopy). The total world production of permanent magnets is of the order of 250,000 tones per year with an annual growth rate between 10% and 20% [Fidler et al. (2004)]. Table 1.2 is a list of commercially available permanent magnets along with their magnetic properties. Figure 1.10 shows the historical development of energy product $(BH)_{max}$ of these magnets. The world market, in value, is shared between the low cost hard ferrites (55%), the Nd-Fe-B based magnets (25%), the SmCo magnets (10%) and the AlNiCo magnets (10%) [Coey (2002); Fidler et al. (2004)].

Table 1.2 Hard magnetic properties of commercially available permanent magnets [Coey (2002); Fidler et al. (2004)]

Magnet	B_r (T)	JH_c (KA m^{-1})	$(BH)_{max}$ (KJ m^{-3})	T_C ($^{\circ}$ C)
Hard ferrites	0.35	320	25	450
AlNiCo ₅	1.30	65	60	850
AlNiCo ₈	0.85	145	55	850
SmCo ₅	0.90	3500	200	720
SmCo ₅ /Sm ₂ Co ₁₇	1.15	3000	260	820
Nd ₂ Fe ₁₄ B	1.52	1500	450	310

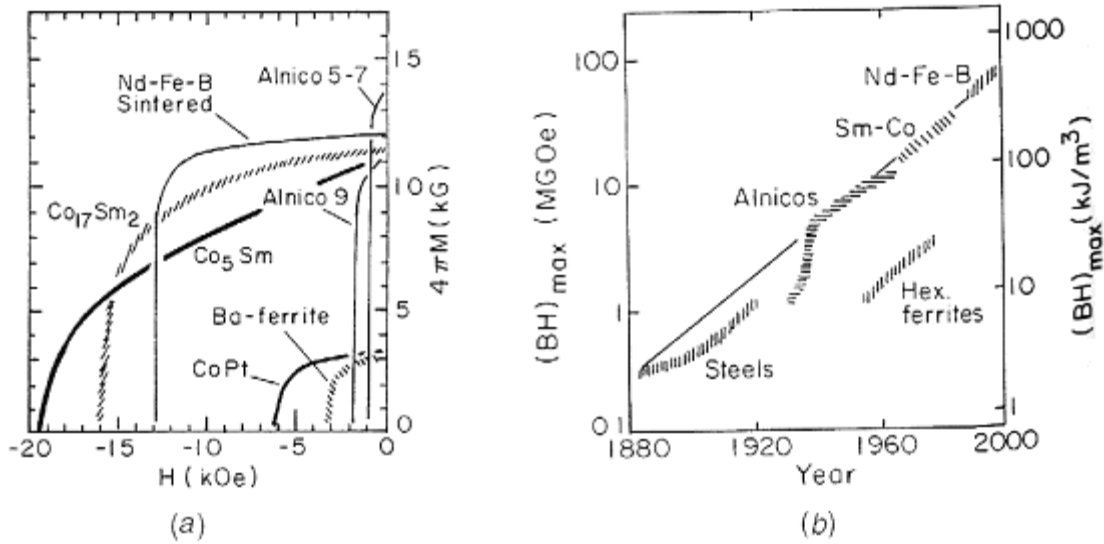


Figure 1.10 The road map of $(BH)_{max}$ product of hard magnets

[O'Handley (1999)]

The $L1_0$ FePt-based permanent magnets are mainly focused on thin film applications. One of the obvious reasons is a large fraction of Pt involved, which makes the material very expensive in the bulk form. One example of application is in magnetic micro-electro-mechanical-systems (Magnetic MEMS) [Niarchos (2003)], which may include magnetic recording, magnetic field sensing, micro-mirrors and biomedical applications. Compared to other permanent magnetic thin films, a major advantage of $L1_0$ FePt thin films is their higher corrosion resistance, due to the Fe-Pt interactions as described previously, which makes them especially useful for practical applications in solid-state devices and biomedicine [Sun (2006)].

Concerning the magnetic properties, however, pure $L1_0$ FePt does not have a large energy product $(BH)_{max}$ (< 13 MGOe), even though it has a very large magnetic anisotropy energy (or coercivity). This is due to the relatively small M_s , determined by the modest

concentration of Fe (50%). “Exchange-spring” or “exchange-coupled” magnets, explored by Kneller and Hawig [Kneller et al. (1991)], are an approach to increase the $(BH)_{max}$ of high H_c materials by adding high M_s soft magnetic phases in the magnets.

Before the discussion of LI_0 FePt based exchange-coupled magnets, the basic principles of exchange coupling are described. Exchange coupling is a very common interface interaction phenomenon in magnetic materials. When two magnetic grains having differently orientated magnetizations are in contact, these two magnetizations will try to be parallel to each other to minimize the exchange energy. The barrier to perfect alignment is the anisotropy energy, which will tend to maintain the magnetization of each grain along an easy axis. Any deviation of the magnetic moments away from the easy axis will increase their magnetic energy. It should be noted that the exchange interaction of neighboring magnetizations is usually limited near the interface, at a distance in the scale of domain wall width, as shown in Figure 1.11. The basic principle of “exchange-spring” magnets is to make a nanocomposite of exchange-coupled hard and soft magnetic phases. When the size of soft phase is small, the magnetization of soft phase can be well coupled along with the hard phase through the exchange interaction. In this condition, the hard phase can provide requisite magnetic anisotropy (thus large H_c) and stabilize the soft phase against demagnetization, while the soft phase can increase the saturation magnetization, M_s , through the increase of transition metal element content. A typical M - H loop of a strongly coupled exchange spring magnet is shown in Figure 12(a), similar to that of a single magnetic phase. However, if the coupling is not strong, two different demagnetizing behaviors will be visible, where soft phase will reverse at a small magnetic field, and hard phase will be reversed at a much higher field, as shown in Figure

1.12(b). The weakly coupled magnets are not helpful to increase the $(BH)_{max}$, because the effective magnetization at large demagnetizing field (H) during demagnetizing process is very small.

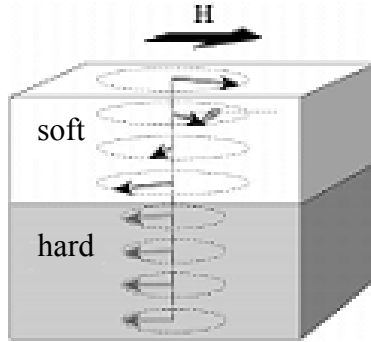


Figure 1.11 Illustration of spring exchange behavior near the hard magnet / soft magnet interface. It indicates that the exchange coupling is very sensitive to the distance.

The fundamental requirements to successfully implement exchange-spring magnets are summarized as follows.

- 1) The size of soft phase must be controlled to be smaller than exchange coupling distance. The critical grain size is found to be roughly twice the width of a domain wall δ_h in the hard phase [Kneller et al. (1991); Skomski et al. (1993); Lieneweber et al. (1997)].

$$\delta_h = \pi \sqrt{A_h / K_h}$$

where A_h and K_h (or K_u) are the exchange and anisotropy constants of the hard phase, respectively. Considering the large values of K_h of permanent magnet materials, this critical size is always in the small nanometer scale [Zeng et al. (2002)]. This value

puts a challenging requirement on most conventional fabrication methods such as melt spinning [Kneller et al. (1991); Skomski et al. (1993); Coehoorn et al. (1989)], mechanical milling [Coey et al. (1997); Ding et al. (1993); Ding et al. (1994)] and sputtering [Withanawas et al. (1994); Withanawas et al. (1995); Wecker et al. (1991)].

- 2) The shape of the hysteresis loop is very important to optimize the magnet properties. The energy product, $(BH)_{max}$, is higher for a more square M-H loop, which for single crystal magnets corresponds to magnetizing the material parallel to the easy axis of the crystal. For polycrystalline magnets, the M-H loop always shows a rounded shoulder. Common approaches to increase the $(BH)_{max}$ in a polycrystalline magnets include trying to obtain a preferred crystallographic orientation of the grains, i.e., a textured structure, and to magnetize the material along the effective easy axis formed by the crystallographic orientation.

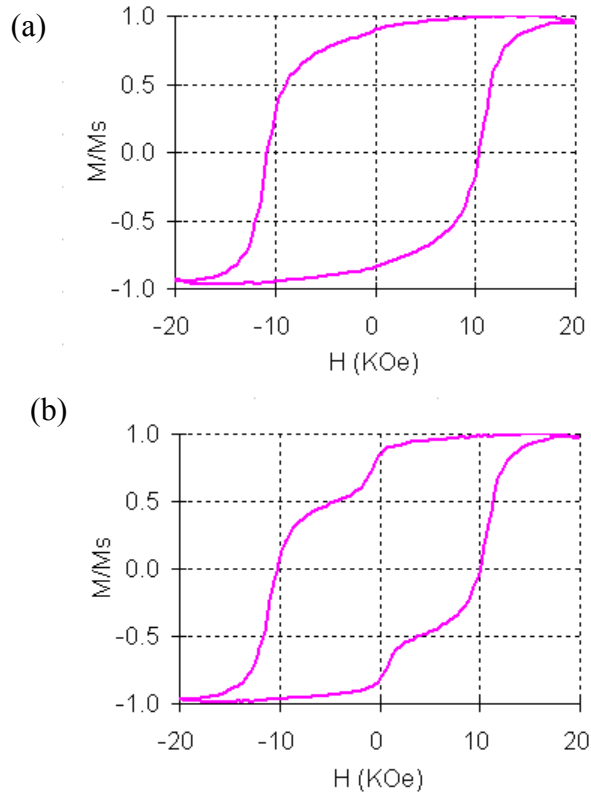


Figure 1.12 Hysteresis loops of spring exchange coupled (a) & uncoupled (b) magnets .

The theoretical simulations of exchange spring magnets, predict a very bright future. However, the experiments show results significantly behind what the theory predicts. For example, it has been predicted that $\text{Sm}_2\text{Fe}_{17}\text{N}_3/\text{Fe}_{65}\text{Co}_{35}$ has a potential $(BH)_{max}$ of 120MGOe, and, similarly 90MGOe for $\text{Nd}_2\text{Fe}_{14}\text{B}/\text{Fe}$ and FePt/Fe , 74MGOe for $\text{Sm}_2\text{Co}_7/\text{Fe}$, and 65MGOe for $\text{SmCo}_5/\text{Fe}_{65}\text{Co}_{35}$ [Fullerton et al. (1999)]. On the experimental side, a large amount of experiments have successfully demonstrated the exchange spring concept. That is to say, the $(BH)_{max}$ of exchange coupled magnets higher than the maximum limit of energy product of the single hard phase has been achieved. However, the $(BH)_{max}$ obtained is still much lower than what the theory predicted. For

example, FePt/Fe₃O₄ exchange coupled nanocomposites have been fabricated using nanoparticle self-assembly. The size of the FePt hard phase region was controlled at 4 nm, and the size of Fe₃O₄ soft phase region was varied from 4 nm to 12 nm. The energy product of 20.1MGOe measured exceeds the theoretical limit of 13MGOe for non-exchange-coupled isotropic FePt by over 50 percent [Zeng et al. (2002)], but is far less than the 90 MGOe that is ideally predicted for FePt-based exchange spring magnets. The most challenging work to achieve high $(BH)_{max}$ in an exchange-coupled magnet is the construction of magnets consisting of highly ordered LI_0 FePt along with the high M_s soft phase. As described earlier, well ordered LI_0 FePt possesses a very large magnetocrystalline anisotropy energy density, and is a perfect candidate of hard magnet in exchange spring magnet to couple the soft magnet phase. Till now, many LI_0 FePt based exchange coupled magnets have been constructed with different soft phases, such as disordered FePt, Fe₃Pt, and Fe₃O₄. Most reported $(BH)_{max}$ values are higher than that of the pure LI_0 FePt phase. However, as to our best knowledge, the reported energy product is still far below the theory predict maximum energy product. A more detailed review will be put in chapter 7, along with our work. The presence of this large gap between the theory predictions and experimental results for LI_0 FePt based exchange coupled permanent magnets, and a much higher processing temperature than desirable (as will be reviewed in chapter 7), partially drives our investigation in this thesis.

1.4 Phase transformation

1.4.1 General introduction

A phase transformation is a process to decrease the system energy by forming a more stable phase (e.g., β) to replace the matrix phase (e.g., α). Based on thermodynamic consideration, they can be classified as first order and second (or higher) order, or discontinuous and continuous phase transformations. At the equilibrium transition temperature (T_c) of the first order phase transformation, the first derivatives of the free energy function, for example

$$\left(\frac{\partial G}{\partial T}\right)_P = -S$$

are discontinuous. In the above equation, T is the temperature, P is the pressure, S is the entropy, and G is the Gibbs free energy. A summary of typical features of first order phase transformation is given below [[Sima \(2004\)](#)].

- 1) Phases are discontinuous in volume (mass density) and entropy (corresponds to the latent heat);
- 2) Phases can coexist and are distinct in equilibrium at T_c ;
- 3) There are interfaces with excess interfacial free energies;
- 4) There is a possibility of existence of metastable phases that are undercooled or superheated (thermal hysteresis);
- 5) The transition proceeds through nucleation and growth of the new phase, and undercooling or superheating is usually necessary to provide enough driving force for nucleation.

Since the first order transition is accomplished through nucleation and growth, and these processes start from local regions within the untransformed regions, these transformations are also called discontinuous phase transformations.

The second (or higher) order phase transformations, are also called continuous transformations. For this kind of phase transformation, the chemical potentials and their first derivatives in the two phases are the same, but their second derivatives are different. In other words, there is no change of the entropy and volume, but the heat capacity is different for two phases. A second order transition has the following characteristics [Sima (2004)]:

- 1) The entropy and mass density are continuous, but the heat capacity at T_c is discontinuous;
- 2) There is no distinction between the phases at T_c ;
- 3) There is no coexistence, no interfaces of phases;
- 4) The concept of nucleation and growth does not apply.

Most solid phase transformations are first order phase transformation, including the disorder to order transformation of FePt, and the formation of $L1_0$ FePt through the reaction of Fe and Pt. Some disorder-order transformation (e.g., CuZn) and conductor-superconductor transitions are second order phase transformation. Without specification, the following descriptions will be limited to the first order phase transformation.

The nucleation and growth of the new phase are the two key components of a discontinuous phase transformation. The process starts from the formation of stable nuclei of a new phase, which can be formed homogeneously, and (perhaps more frequently) heterogeneously. For both types of nucleation, the driving force is the

decrease of the chemical potentials, and the barrier can be the energy of the interface with the new phase, and may include strain energy due to the change of volume or from coherent interfaces. For homogeneous nucleation, the nucleation rate (\dot{N}) can be expressed as:

$$\dot{N} \propto C_o \omega \exp\left(\frac{-\Delta G_{\text{hom}}^*}{k_B T}\right) \exp\left(\frac{-\Delta G_m}{k_B T}\right)$$

where C_o is the number of potential nucleation sites for the new phase per unit volume; ω is the attempt frequency; ΔG_{hom}^* is the nucleation energy barrier; ΔG_m is the activation energy for atomic migration; k is the Boltzmann constant; and T is the absolute temperature.

Heterogeneous nucleation takes advantage of existing surfaces, grain boundaries, dislocations to decrease the nucleation energy barrier at some density of special sites (much less than N_o), thus typically making the process easier. The rates of heterogeneous nucleation must additionally consider the availability of specific types of nucleation sites, and the critical nucleation energy barrier for each type of sites considered.

The study of the growth of the new phase is also important. Phase transformations involving atomic diffusion can be further classified as diffusion controlled and interface controlled growth. Diffusion controlled growth corresponds to the phase formation involving a change of composition for the new phase wherein the growth rate is limited by the diffusion in a local concentration gradient. This growth rate (\dot{R}) can be expressed as:

$$\dot{R} = \alpha \omega \left(1 - \exp\left[-\frac{\Delta G}{k_B T}\right]\right) \exp\left(-\frac{Q_G}{k_B T}\right)$$

where α is an atomic jump distance; ω is a characteristic vibrational frequency; ΔG is the driving force for the phase transformation; and Q_G is the activation energy for growth.

Another type of phase transformation does not involve any change of average composition, such as the disorder-order phase transformation discussed in this thesis. In this case, growth of the new phase is limited by the short-range atomic diffusion at the interface from the disordered matrix to the new ordered phase. Therefore, it is called interface controlled phase growth.

A phase formation can be limited by the nucleation, growth, or both. While nucleation must necessarily precede growth, a nucleation limited phase transition refers to the one with a low nucleation rate or scarce density. The C49-C54 TiSi₂ phase transformation is one example [Ma et al., (1994)]. C54 TiSi₂ can only be nucleated at the triple points of C49 TiSi₂ grain boundaries. The scarcity of such nucleation sites strongly limits the nucleation density of the new phase, and thus limits the formation of the new phase. Even when the new phase nuclei are plentiful, their subsequent growth can also be very difficult, especially at a low processing temperature, due to low atomic mobility. Both an adequate nucleation rate and growth rate of the new phase are needed to accomplish a phase transformation within a given time.

The theoretical modeling and experimental characterization of phase transformations can be used to construct the time-temperature-transformation (TTT) diagram, which is a very valuable tool to guide the phase transformation experiments. The Johnson-Mehl_Avrami_Kolmogorov (JMAK) theory has been commonly used to model phase transformations that occur by nucleation and growth [Johnson and Mehl,

(1939); Avrami, (1939-1941); Kolmogorov, (1937)]. The general form of the JMAK expression is given by.

$$X_V = 1 - \exp(-X_E)$$

where X_V is the actual volume fraction of new phase, X_E is the extended volume fraction. The JMAK model provides a correction accounting for the overlapping regions, as growing phase grains impinge on each other when the phase transformation progresses to completion. The derivation of an analytical expression for X_E considering different nucleation type, shapes of nuclei and grains, and varying nucleation and growth rates can be very difficult, if it is not impossible. For the disorder order transformation of FePt films, analytical JMAK expressions have been derived [Berry, (2007)].

The experimental characterization to determine X_V , the volume fraction of new phase, can be conducted by many approaches. For example, XRD or neutron diffraction may be used to determine the phase fraction in many cases. Microscopy (optical and electron) can be used to directly examine the structure and volume fraction of phases present in a sample. Another approach, probably more convenient, is through the DSC experiments. The latent heat released during the experiment can be correlated with the volume fraction of new phase formed.

1.4.2 Disorder-order phase transformation of FePt

The term “order” in this thesis is restricted to structural disorder-order changes, which are based on the spatial ordering of atoms or molecules. In a disordered structure, as shown in Figure 1.2, the crystal lattice sites are randomly occupied by different atoms, and the probability of one site being occupied by one specific atom is equal to its concentration. For example, in the disordered FePt structure, Fe and Pt atoms will have the equal probability to occupy any site of a unit cell. In the ordered $L1_0$ FePt phase, however, the Fe and Pt will align themselves layer by layer along $\langle 001 \rangle$ direction.

The perfectly ordered structure does not exist, based on entropy considerations, and a long-range order parameter (S) is used to characterize the ordering. For a binary ordered alloy S is given by:

$$S = \frac{P_A^\alpha - X_A}{1 - X_A} = \frac{P_B^\beta - X_B}{1 - X_B}$$

Where, P_A^α is the probability that α sites were occupied by A atoms, and X_A is the fraction of A atoms. Similarly, P_B^β is the probability that β sites are occupied by B atoms, and X_B is the fraction of B atoms. Obviously, the S for a purely random or disordered structure is 0, while that for the perfectly ordered structure is 1.

The long range order parameter, S , can be measured by two techniques for $L1_0$ FePt. The first method is to compare the experimental integrated intensity ratios of selected superlattice and fundamental X-ray diffraction (XRD) peaks to a calculation of the intensity ratio expected for the perfectly ordered phase. In this approach, S can be calculated from:

$$S^2 = \frac{\left(\frac{I_{001}}{I_{002}} \right)_{\text{measured \& corrected}}}{\left(\frac{I_{001}}{I_{002}} \right)_{S=1}}$$

Where 001 is the superlattice peak, and 002 is the fundamental peak. Similar pairs such as 110 and 220 are also commonly used. The value of $\left(\frac{I_{001}}{I_{002}} \right)_{\text{measured \& corrected}}$ is the measured integrated intensity ratio, while $\left(\frac{I_{001}}{I_{002}} \right)_{S=1}$ is the calculated intensity ratio for perfectly ordered (S=1) FePt phase. Details for the calculation can be found in Chapter 5. Another approach is to compare the (c/a) ratio of the ordered LI_0 FePt phase compared to that of the perfectly ordered value. As the ordering induces a tetragonal distortion to the cubic lattice of the disordered phase ($c/a = 1$), the ratio of the lattice parameter in the ordering direction compared to that perpendicular to the ordering direction can also be used to indicate the extent of order. With this approach, S is calculated with the form expressed below.

$$S^2 = \frac{(c/a)_{\text{experiment}}}{(c/a)_{S=1}}$$

The disorder-order phase transformation of FePt is well known to be a first order phase transformation, i.e., through the nucleation and growth. The TTT diagram for certain types of samples have been calculated by Berry and Barmak et al., which gives valuable information to optimize the processing condition [Berry and Barmak, (2007)]. On the kinetics of LI_0 FePt formation through the Fe and Pt thin film multilayer reaction, some interesting studies have been reported [Zotov et al., (2007), Endo et al., (2001, 2003)], as will be reviewed later. However, a clear understanding is still absent. It is

suspected that understanding the $L1_0$ FePt formation in multilayers will be of at least equal interest, compared to that in FePt alloy films.

1.4.3 Phase transformation in thin films

Phase transformation in thin films is different from that in bulk samples considering the nucleation and phase growth of the product phase. For example, an “edge effect” may influence the phase transformation in thin films and a model of this effect can be found elsewhere [Balluffi et al. (2005)]. Figure 1.13 simply illustrates the influence that the edge effect can have on the volume fraction of product phase. Figure 1.13(a) shows the nucleated product phase in the bulk sample, and Figure 1.13(b) shows that in the thin film. It can be seen that the absence of neighboring nuclei in the thin film sample (as labeled as A, B, C, D, and E in the bulk sample) decreases the volume fraction of product phase in the thin film transformation. A correction for film thickness has been reported using the JMAK equations in two dimensions [Balluffi et al. (2005); Lee and Barmak, (2003)] and three dimensions [Berry and Barmak, (2007)].

The growth of the new phase grains in thin films is also different from that in bulk samples. Grain growth in thin films generally starts in both the film thickness direction and in-plane directions to form a columnar structure, wherein single grains extend from the top to the bottom surface of the film. When the in-plane grain size becomes nearly equal to film thickness, further grain growth is inhibited. Higher annealing temperatures are needed to provide the adequate mobility for further in-plane grain growth [Thompson (1990)]. Therefore, the phase transformation is highly dependent on the film thickness. Different grain growth behaviors of product phase, at the expense of matrix phase, in films with different thicknesses result in different volume fractions of new phases, and thus influence the extent of the phase transformation.

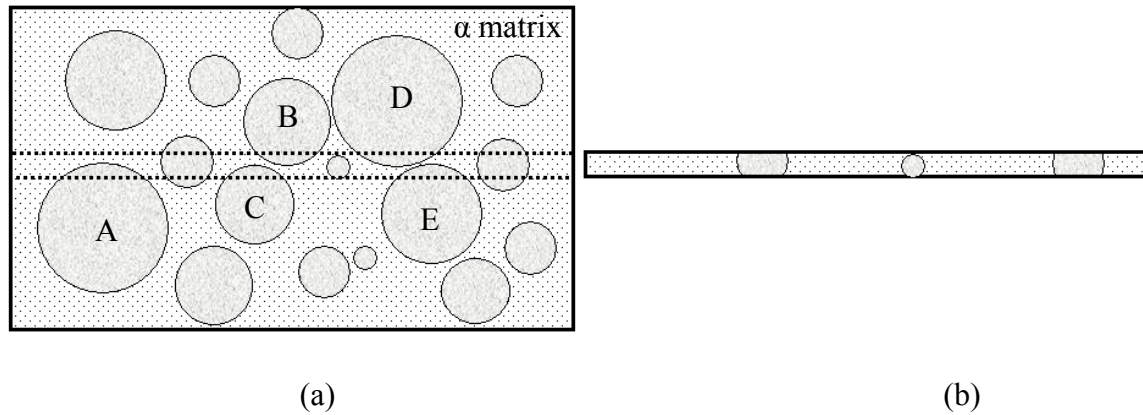


Figure 1.13 The illustration of the influence of “edge effect” on the volume fraction of product phase. The filled circles indicate the nucleated product phase. The absent of neighboring nuclei (A, B, C, D, and E) in thin film (b), as compared to the bulk sample (a), decreases the volume fraction of product phase.

Furthermore, a smaller grain size expected in thin films and the existence of texture may also have a role to distinguish phase transformations in thin films from that in bulk samples.

1.4.4 Phase transformation through thin film multilayer reactions

The basic principles of interdiffusion and reaction of bulk bi-layer or multilayer samples upon heat treatment are well understood. When a bulk diffusion couple A-B is annealed at a certain temperature, the sharp A/B interface evolves into a compositional profile which is consistent with the phase diagram. The equilibrium phases present at the annealing temperature chosen are expected to appear along the compositional profile with well-defined phase boundaries. The product layers grow upon further annealing as the region of compositional change widens. The heat treatment temperature for such interface reactions is usually above $0.5T_m$, and consequently lattice diffusion is usually assumed to dominate the atomic transport. It is expected that the net diffusional transport mainly occurs perpendicular to the interface, while no diffusion is expected in the directions parallel to the interface. As one example, the study of bulk $[\text{Fe}/\text{Pt}]_n$ multilayer films by Verdier et al. [[Verdier et al., \(2005\)](#)] characterized such annealed samples using field emission gun scanning electron microscopy, and found the presence of three distinct product layers, Fe_3Pt , FePt_3 and $L1_0$ FePt, in the reaction zone.

Thin film interfacial reactions are generally believed to be different from that of bulk samples due to both the lower heat treatment temperature and the thin film microstructure. A detailed discussion and an example of a proposed reaction model can be found in Coffey's dissertation [[Coffey \(1989\)](#)]. Briefly, thin film reactions are always conducted at a much lower temperature than their bulk counterparts. As a result, grain boundary diffusion is much stronger than the lattice diffusion, contrary to the bulk sample reaction. Another factor to enhance the grain boundary diffusion is the smaller grain size of thin films (usually at small nanometer scale). A larger fraction of grain boundaries due

to the small grains makes the diffusion along the grain boundaries much easier at the low annealing temperatures. The dominant role of grain boundary diffusion results in a complicated compositional gradient. Because atoms transport along the grain boundaries, the diffusion occurs not only at the direction perpendicular to the interface, but also in directions parallel to the interface, or any other direction where there is a local compositional gradient in the grain boundary network. Therefore, it is expected that the composition is different at different sites of the grain boundaries, or different positions in a single grain, and equilibrium between the grain boundaries and the grain interior regions may not prevail. The lack of equilibrium and the complicated composition distribution in thin films makes it difficult to predict the product phase(s) formed. Contrary to that of the bulk sample reaction, the thin film reactions may not result in distinct product layers.

Another distinct characteristic of thin film reactions is that not all the equilibrium phases may appear in the annealed film. In reality, the prediction of the first compound as well as the sequence of compound formation is usually difficult. For metal-semiconductor (i.e., metal-silicon, metal-germanium) reactions, three rules have been formulated to predict the first compound [Ohring (2002)]. The first rule is “the first phase to nucleate is the most stable congruently melting compound adjacent to the lowest temperature eutectic on the bulk-equilibrium phase diagram” [Walser et al. (1976)]. The second rule states that “if the choice is between two phases, the first to appear is the one which suffers the largest free energy degradation rate” [Zhang et al. (1993)]. The third rule says “the first compound to form is the congruently melting phase with the most negative heat of formation at the concentration of the liquidus minimum of the binary

system” [Pretorius et al. (1999)]. It should also be pointed out that exceptions exist for these rules [Ohring (2002)]. After a first product phase is formed, the subsequent sequence of compound formation seems to be even more difficult to predict. A general rule on this issue has not been reported. Experimental factors, such as annealing temperature and time, composition, film thickness or periodicity, can strongly influence the compound forming first, as well as the following sequence. Till now, the sequence after the initial reaction has only been established in a few silicide systems [Ohring (2002)].

CHAPTER 2 MOTIVATION, OBJECTIVE, AND THESIS OUTLINE

This thesis studied the diffusion and reaction of $[\text{Fe}/\text{Pt}]_n$ multilayer films. The motivation of this study has been mentioned in previous chapter. In summary, $L1_0$ FePt has potential applications as high-density magnetic recording medium and exchange coupled permanent magnets. Heat treatment of $[\text{Fe}/\text{Pt}]_n$ multilayer films is a very promising approach to form the $L1_0$ FePt phase and exchange spring magnets at low temperature, and a minimum processing temperature is highly desirable for these applications. Although some interesting results have been reported on the study of the $[\text{Fe}/\text{Pt}]_n$ multilayer films upon heat treatment, the mechanisms of $L1_0$ FePt phase formations is still far from clear.

The objective of this study is to understand more about the diffusion and reaction of $[\text{Fe}/\text{Pt}]_n$ multilayer films, specifically, to make clear the process-structure-property relations. The fabricated and processed multilayer films having different film composition, periodicity (bi-layer thickness), deposition temperature, thickness, annealing temperature and time. were investigated systematically. A novel technique, based on hollow cone dark field (HCDF) TEM, was developed to quantify the fraction of a sample that had transformed to the $L1_0$ FePt phase. The annealed films were characterized concerning the phase fraction, grain size, interdiffusivity, long-range order parameter, texture, as well as magnetic properties. To explore the potential applications (pure $L1_0$ FePt medium, or exchange coupled magnets), different experiments were designed. To study the formation of pure $L1_0$ FePt phase in the annealed films, the samples with an average composition about $\text{Fe}_{50}\text{Pt}_{50}$ were deposited. For the application

for exchange spring magnets, samples with a higher Fe content were prepared to construct a mixture of soft and hard magnetic phases, in order to achieve a high energy product $(BH)_{max}$ of annealed films.

The novelty and merit of this study comes from several factors. First of all, the theory and modeling of thin film interfacial diffusion and reaction is different from that of bulk samples. On the study of Al/Nb multilayer reactions, as one example, Coffey and Barmak et al. demonstrated that the thin film diffusion and reaction follows a different model due to a much lower annealing temperature and small grain size compared to that of the bulk sample [Coffey et al., (1992) I, II; Barmak et al., (1990), (1992)]. This study of $[\text{Fe/Pt}]_n$ reactions further adds to our understanding of thin film reactions. On the experimental side, the characterization of thin film reactions is not a trivial task, due to their typical feature size in nanometer scale. To address the reaction characterization issue, this work includes the development of a novel technique for quantification of the reaction process. This contribution is significant to advance the understanding of solid-state reactions from bulk samples to thin films, as many standard methods to characterize the interface reaction of bulk samples may not be applied. Further, this thesis makes specific contributions to our understanding of what can, and can not, be achieved for applications of the $L1_0$ FePt phase. The need for future work and discovery to provide enhanced $L1_0$ phase nucleation for magnetic recording applications is quite clear. For permanent magnets, this work has demonstrated that $[\text{Fe/Pt}]_n$ multilayer reactions can provide exchange spring magnets with an energy product, $(BH)_{max}$, higher than that of the pure $L1_0$ FePt phase using low processing temperatures ($\sim 400^\circ\text{C}$), which is very significant for MEMS applications of hard magnets.

This main body of this thesis consists of four closely related research works which will be described separately in chapter 4 , 5, 6, and 7. Each chapter is composed of an introduction, experimental, results and discussion sections. Chapter 3 gives a general description of the instruments used for fabrication, processing, and characterization that are common to all four chapters.

Chapter 4 is presents the cross sectional transmission electron microscopy (XTEM) study of annealed $[\text{Fe}/\text{Pt}]_n$ multilayer films. The XTEM study of annealed multilayers indicates that the Pt layer grows at the expense of Fe during annealing, which is most probably due to the different solubilities of Fe and Pt. A continuous $L1_0$ FePt product layer is not found, instead, the small $L1_0$ FePt grains are distributed mainly at the grain boundaries and Fe/Pt interfaces of the matrix. The annealed films are found to have a mixture of disordered *fcc* FePt and ordered $L1_0$ FePt phase grains. The disordered FePt phase is formed by interdiffusion of Fe into Pt (or through the nucleation of *fcc* FePt and growth), and the ordered $L1_0$ FePt phase is formed by an interface reaction and disorder-order transformation.

Chapter 5 provides a more comprehensive study of annealed $[\text{Fe}/\text{Pt}]_n$ films concerning the phase fraction, grain size, nucleation/grain density, interdiffusivity, long-range order parameter, and texture, as well as magnetic properties. A method based on HCDF TEM is introduced to measure the volume fraction, grain size, and density of ordered $L1_0$ FePt phase grains in the annealed films, and a model based on low-angle X-ray diffraction is used to measure the effective Fe-Pt interdiffusivity. The process-structure-properties relations of two groups of samples with varying substrate temperature and periodicity are reported. The results demonstrate that the processing

parameters (substrate temperature, periodicity) have a strong influence on the structure (effective interdiffusivity, LI_0 phase volume fraction, grain size and density) and magnetic properties. The correlation of these parameters suggests that the annealed $[\text{Fe/Pt}]_n$ multilayer films have limited nuclei, and the following growth of LI_0 phase is very important to the extent of ordered phase formed. A correlation between the grain size of fcc FePt phase and the LI_0 FePt phase fraction (or magnetic properties) strongly suggests that the phase transformation of $fcc \rightarrow LI_0$ is highly dependent on the grain size of the parent fcc FePt phase. A selective phase growth model is proposed to explain the phenomena observed.

Chapter 6 reports an investigation of the influence of total film thickness on the formation of LI_0 FePt phase in $[\text{Fe/Pt}]_n$ multilayer films and compares this to that of FePt co-deposited alloy films. A general trend of greater LI_0 phase formation in thicker films was observed in both types of films. It was further found that the thickness dependence of the structure and of the magnetic properties in $[\text{Fe/Pt}]_n$ multilayer films is much stronger than that in FePt alloy films. This may be related to the higher chemical energy contained in $[\text{Fe/Pt}]_n$ films than FePt alloy films, which is helpful for the LI_0 FePt phase growth. However, the initial nucleation temperatures of $[\text{Fe/Pt}]_n$ multilayers and co-deposited alloy films were found to be similar.

Chapter 7 reports an investigation of LI_0 FePt-based exchange spring magnets. It is known that exchange coupling is an interfacial magnetic interaction and it was experimentally shown that this interaction is limited to within several nanometers of the interface. A higher degree of order of the hard phase is helpful to increase the length scale slightly. Two approaches can be used to construct the magnets. For samples with

composition close to stoichiometric LI_0 FePt, the energy product, $(BH)_{max}$ is limited by the average saturation magnetization, and therefore, a lower annealing temperature is beneficial to increase the energy product, which gives a larger fraction of disordered phase. For sample with higher Fe concentration, $(BH)_{max}$ is limited by the low coercivity of annealed sample. A relatively high annealing temperature is beneficial to increase the ordering and coercivity, and thus to increase the energy product.

The last chapter, chapter 8, will present the conclusions of this thesis and describe suitable directions for future works.

CHAPTER 3 EXPERIMENTAL METHODS

This chapter gives a brief description of the instruments used for film fabrication, processing, and characterization. In this work, magnetron sputtering was used to fabricate the thin films. A tube furnace equipped with a magnet-coupled sample transfer was set up and used to anneal the samples in a reducing atmosphere. Rutherford backscattering spectrometry (RBS) provided an accurate characterization of film thickness and composition. Sample structure characterization by TEM has been used routinely in our study. A special TEM imaging mode, HCDF, was used extensively in this study, and this technique will be described in detail since it is not a commonly used mode. The techniques for plan view and cross-sectional TEM sample preparation will also be briefly introduced. Low and high angle XRD were also used to characterize the multilayer structure, effective Fe-Pt interdiffusivity, and ordering. Finally, the magnetic properties were characterized with an alternating gradient force magnetometer (AGFM).

3.1 DC/RF magnetron sputtering

A state-of-the-art six-gun sputtering system (AJA2200, provided by AJA International Sputtering Inc.) equipped with residual gas analysis, quartz crystal oscillator, substrate cooling and heating, was used to fabricate the sample films. The whole system was controlled by an automated program, which allows a precise control of the deposition process. This automated program is especially useful for preparation of multilayer films. A base pressure in the range of 10^{-8} Torr was achieved before the film deposition. The cooling of the substrate was realized by contacting the substrate holder with a tank filled with liquid nitrogen. The heating of the substrate was accomplished with a high power lamp inside the chamber. The sputtering parameters include: power, power type (DC or RF), gas flow, gas pressure, substrate temperature, and bias condition.

3.2 Modified tube furnace

A tube furnace equipped with a magnet coupled sample transfer, as shown in Figure 3.1, was set up and used to anneal the films. One end of the quartz rod was attached to a magnet with adhesive tape. Outside the tape was wrapped a Ti foil to decrease the friction force between the plastic tape and quartz tube during the sample transfer. The coupling between the magnets in and outside the quartz tube makes the sample transfer possible without opening the tube and disturbing the annealing ambient gas. Before the annealing, the crucible with the sample inside was first set near the door of the furnace, and the rod (one magnet attached) was put inside the tube. After the tube was sealed with two rubber stoppers and a constant gas flow of Ar+(3~5)%H₂ (at one atmosphere pressure) inside the tube was ready, the furnace was turned on and the temperature increased steadily to the desired temperature. When the annealing temperature is stabilized (and the tube suitably purged of residual air by the gas flow), the crucible (with the sample) was set to the center of the tube furnace through the coupled magnets. Because of a much smaller heat capacity of sample crucible compared to that of the tube furnace, the temperature only slightly changes (usually smaller than 5°C) when the sample is introduced. When the annealing is finished, the sample crucible can be pushed to the cooling zone on the other side of the furnace. If the annealing temperature is at or lower than 500°C, the quartz tube in the cooling zone can be wrapped with wet paper towels. In this way, the film temperature will be quenched to the room temperature quickly, usually in minutes.

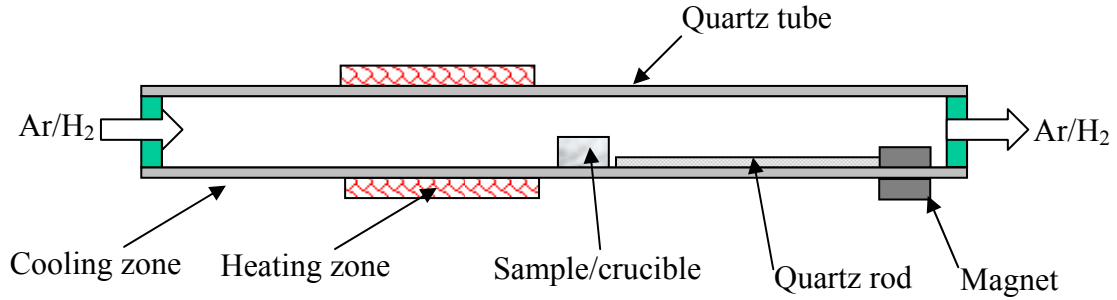


Figure 3.1 A schematic view of a modified tube furnace.

It is interesting to notice that the relative position of the sample film and the crucible is very important. The crucible has a bowl shape, and all samples are supposed to stay at the bottom of the bowl. However, it was found the samples annealed in this way are easy to be oxidized, especially for samples with higher Fe concentration. The author believes that the oxidization is due to the water vapor condensed on the surface of crucible or sample that is released when the crucible is heated. Because the sidewall of the crucible effectively decreases the velocity of gas flow, the water vapor can not be balanced with the Ar/H₂ gas in a quick manner. To avoid this problem, a piece of oxidized Si wafer with a size relatively smaller than the opening of the crucible is set to support the samples, as shown in Figure 3.2. In this way, the annealing samples experience a large velocity of Ar/H₂ gas flow to balance the water vapor.

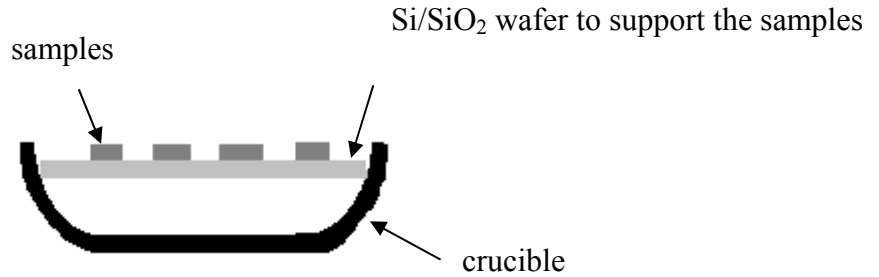


Figure 3.2 The relative orientation of samples, Si wafer, and crucible.

It was further found that the sample orientation on the supporting Si/SiO₂ wafer can also influence the structure and properties of annealed samples. For example, the sample annealed with the film side facing up generally has a slightly higher coercivity than the one with film side facing down. This fact may partially demonstrate the influence of annealing ambient on the formation and ordering of $L1_0$ FePt phase. To make the comparative study meaningful, all samples in each group studied later were annealed in the same condition.

3.3 Rutherford backscattering spectrometry

RBS is a very useful technique to characterize thin film composition and thickness. The basic principle of RBS is using high-energy ions (2.5MeV H^{++}) to bombard thin films and to measure the energy of the ions reflected from the sample. The He^{++} ions collide with atoms in the sample elastically, and are scattered back due to their much smaller mass. The energy of back scattered He^{++} is related to the atomic mass of elements in the film through Equation 3.1. A typical RBS spectrum of FePt film is shown in Figure 3.3. The peak of Fe and Pt in the film, as well as the Si and O peaks in the substrate were identified. The full width at half maximum (FWHM) of the peaks can be used to determine the film thickness, and the area of each peak is proportional to the concentration of the elements. The simulation of the as-acquired spectrum using the RUMP software gives the composition and thickness of samples. This technique provides a highly accurate means to measure film composition and thickness. For FePt films, RBS gives a composition resolution about 0.5% for Fe and Pt, and the thickness resolution is better than 1 nm. Another advantage of this technique is that no reference sample is needed for the measurement.

$$E_1 = \left\{ \frac{\left(M^2 - M_0^2 \sin^2 \theta \right)^{1/2} + M_0 \cos \theta}{M_0 + M} \right\}^2 E_0 \quad (3.1)$$

where M_0 and E_0 are the mass and energy of incident ions (He^{++}), respectively. E_1 is the energy of back-scattered H^{++} ions. M is the mass of atom in the samples to be investigated. θ is the angle between detector and incident ion beam.

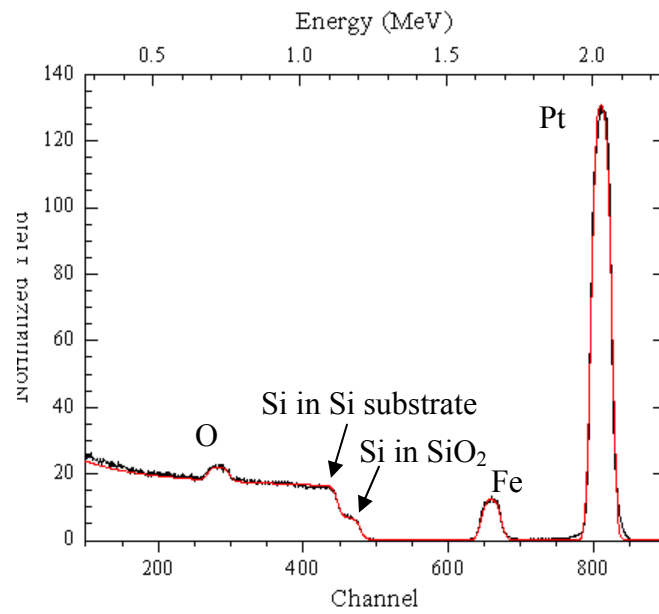


Figure 3.3 A typical RBS spectrum of FePt film on SiO₂/Si substrate. The red line is the simulation curve, and the dark line is the as-acquired spectrum.

3.4 Transmission electron microscopy

A FEI Tecnai F30 analytical TEM/STEM was used extensively to characterize the as-deposited and annealed films. Commonly used modes of TEM/STEM, such as bright field (BF), dark field (DF), high resolution transmission electron microscopy (HRTEM), high angle annular dark field (HAADF), are familiar to most readers, and will not be described here.

Hollow-cone dark field (HCDF) TEM imaging has been proven to be very useful in this study, and is described in detail here. The diffraction pattern of polycrystalline samples is composed of a central spot (undiffracted beam) and a series of diffraction rings, as shown in Figure 3.4 (a). As is well known, the BF TEM technique is to form the image using the objective aperture to select the direct beam, while the conventional DF TEM technique is to select a diffraction spot (for single crystal) or a portion of one or more diffraction rings (for polycrystalline materials) to form the image. The ideal HCDF TEM technique, however, is to select the whole diffraction ring(s) to form the dark field image, shown in Figure 3.4 (b). Because the ideal aperture is not easy to construct, HCDF TEM provides another approach, as shown in Figure 3.4 (c). First the diffraction pattern was deflected on the view screen, so that the centered objective aperture selects a portion of the diffraction pattern. Under the computer control, the diffraction pattern rotates around objective aperture. The whole ring(s) can thus pass through the aperture to form the HCDF images. Because of a large rotation speed (10 rounds/second) and a long integration time of the CCD to form the HCDF image, the image formed with this approach is identical to that from the ideal case, figure 3.4 (b). It should be noted that

the number of ring(s) selected depends upon the relative size of objective aperture used and diffraction pattern on the view screen.

HCDF TEM imaging has been widely used to study the phase distribution in a sample composed of two or more phases. Recently, we demonstrated that high contrast dark field TEM images can be achieved with this mode using multiple reflection rings. Figure 3.5 is a HCDF TEM image of a 40 nm thick Cu film annealed at 600°C to investigate its grain growth. The diffraction rings used to form the image include 111, 200, 220, 311, and 222 reflection rings. The specific applications of the HCDF mode in this thesis include determination of the volume fraction of the ordered of $L1_0$ FePt phase, and studies of the microstructure of $L1_0$ FePt phase, as will be presented.

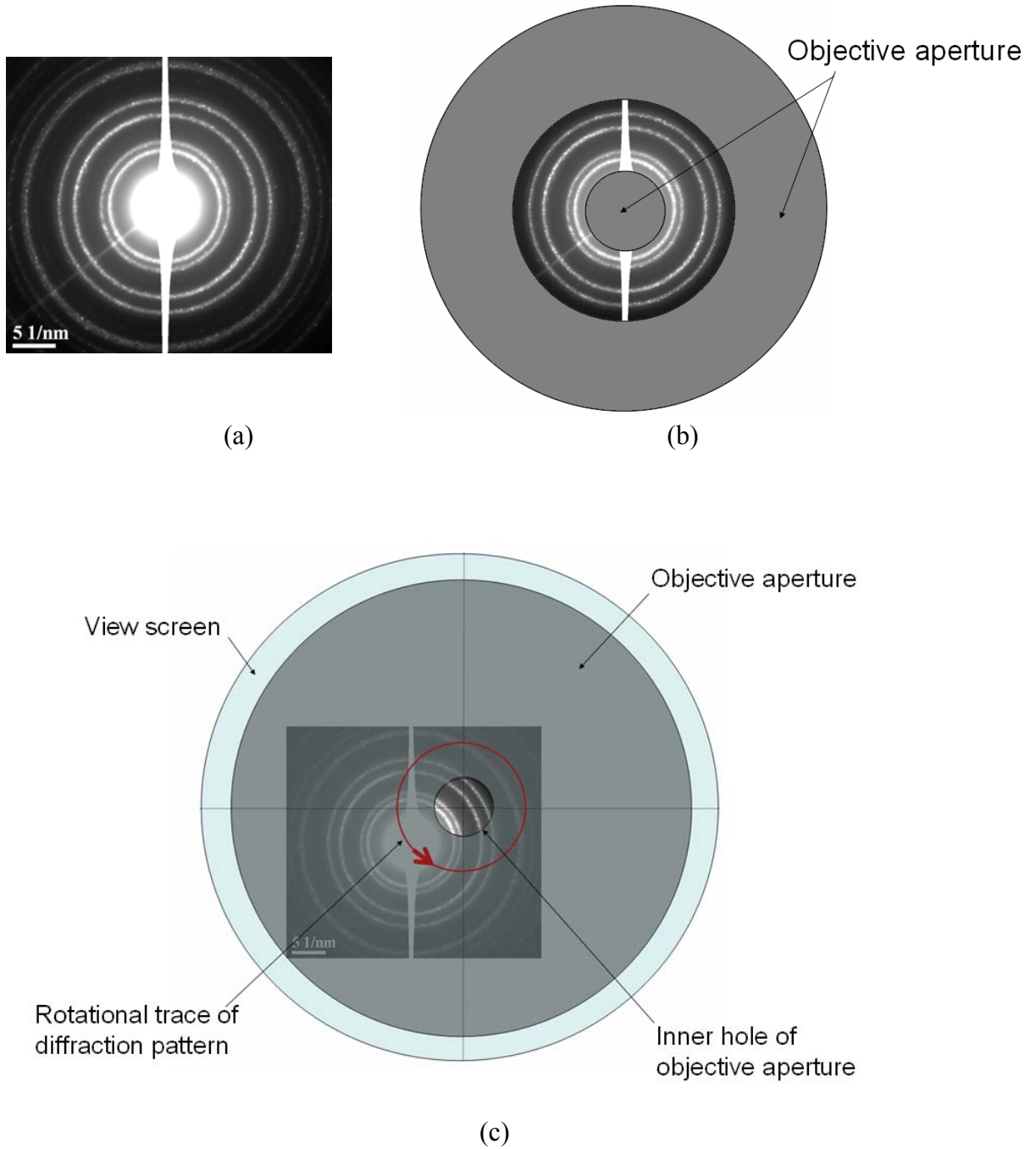


Figure 3.4 (a) diffraction pattern of polycrystalline Cu films; (b) HCDF-TEM with ideal objective aperture; (c) practical operation for HCDF-TEM.

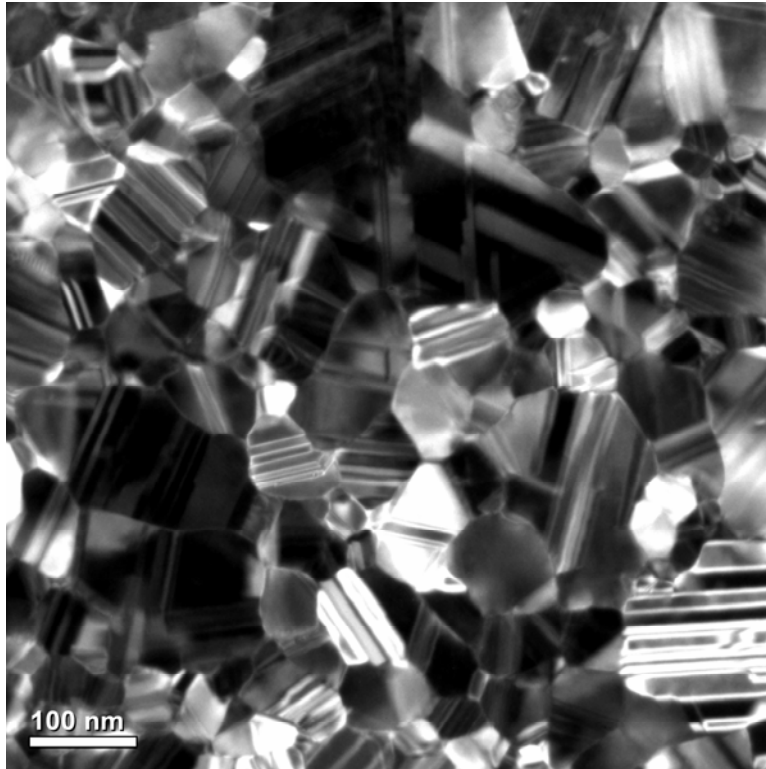


Figure 3.5 A high contrast Cu TEM image with the HCDF-TEM mode

TEM sample preparation, including both plan view and cross sectional view preparations, is always tedious and time-consuming. In our study, a modified back-etch technique is used to provide a rapid way to prepare the plan view TEM samples. The principle of this technique is to etch all the Si substrate away, and leave the film membrane for TEM examination. The film membrane can be further thinned with low angle ion milling until an optically transparent sample is achieved. For metallic samples like FePt, it indicates a thickness about 10 nm. Such thickness well satisfies some special TEM sample requirements in our work, which need the TEM sample to be as thin as

possible. Details of the back etch techniques for TEM sample preparation can be found in the references [[Yao and Coffey, \(2007\)](#); [Yao and Coffey, \(2008\)](#)].

The cross sectional TEM sample preparation of thin films is usually more difficult than that of the plane view samples. Additional problems to prepare XTEM samples of $[\text{Fe/Pt}]_n$ multilayers include the ready delamination due to the absence of strong chemical bonding between film and substrate, different milling rate of Si/SiO₂ and $[\text{Fe/Pt}]_n$, and others. A technique based on the combination of focused ion beam (FIB) milling and tripod polishing is applied to prepare the XTEM samples of these films, which can be used as a generally high throughput approach for XTEM sample preparation of thin films [[Yao and Coffey, \(2008\)](#)]. Briefly, the tripod polishing is used to quickly thin the sample to about 10 μm , and the FIB milling is utilized to further thin the sample from 10 μm to less than 100 nm. Details can be found in the reference.

3.5 X-Ray Reflectometry

High angle XRD is a very useful technique to characterize the phase, structure, stress, and other properties of materials. Because it is familiar to most readers, it is not described here. Another very useful X-ray scattering technique, X-ray reflectometry (XRR) deserves more description.

XRR is essentially a theta-2theta scan at small angle (usually $0^{\circ}\sim 5^{\circ}$). When X-rays strike the film surface at a glancing incidence angle, they reflect off the film surface and the film/substrate interface. These reflected waves construct or deconstruct each other to form the XRR spectrum, as shown in Figure 3.6, a typical XRR spectrum of $[\text{Fe}/\text{Pt}]_n$ multilayers. The reflectivity of X-rays is sensitive to the change of density and roughness. Taking advantage of this effect, XRR can provide information regarding the film thickness, roughness, and the density. Briefly, the critical angle, which is defined as the angle at which the intensity is half of the maximum intensity, can be used to derive the film density. The general decrease in scattered intensity with increasing scanning angle is related to the roughness of the interface, and the period of the oscillatory peaks is used to determine the film thickness. The density, roughness, and thickness of the films are given by the simulation of the acquired spectrum through software provided by Bede Scientific Corp.

In this thesis, XRR was used to examine the multilayer structures, and to determine their effective interdiffusivity. Different from that of a single layer film, the XRR pattern of multilayer film has additional small angle Bragg reflections (as “A” and “B” peaks in Figure 3.6), which can be used to determine the film bi-layer periodicity.

The decrease in the intensity of these first small- angle Bragg reflections (e.g., A and B) during annealing is related to the interdiffusivity. In theory, such peaks due to the repeating layers will also appear near the high angle peaks (e.g., 111). However, their intensities at high angle are generally lower than those at low angle. For convenience, this study will focus on the small angle Bragg reflections. Details will be given in Chapter 5.

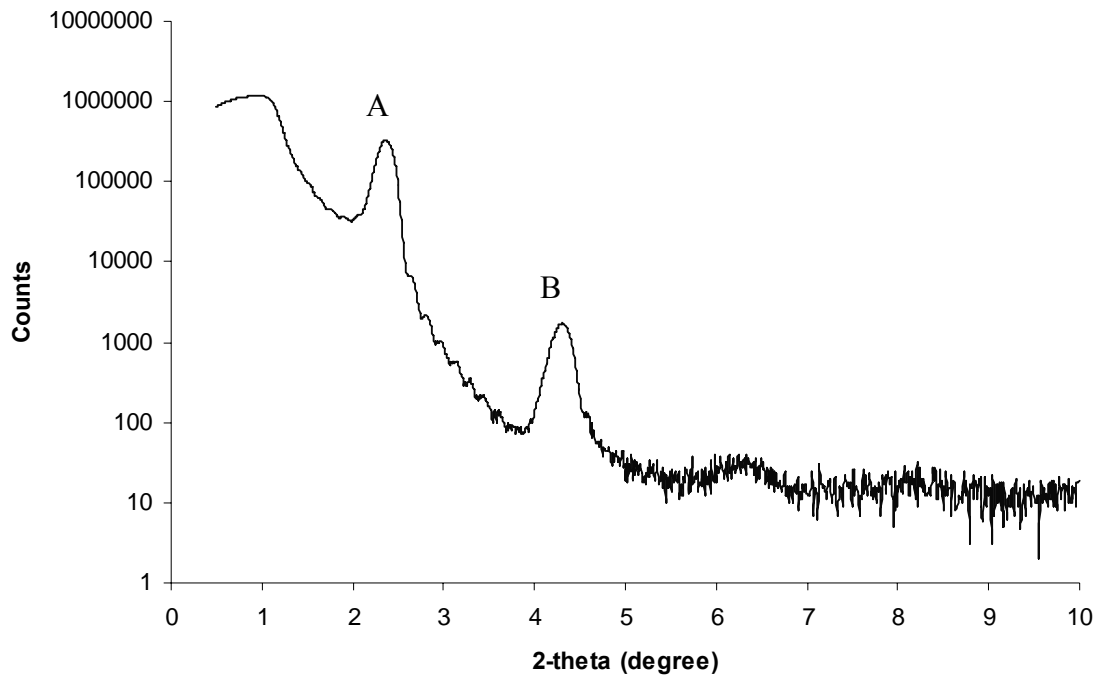


Figure 3.6 A typical XRR spectrum of $[\text{Fe}/\text{Pt}]_n$ multilayer films

3.6 Alternating Gradient Field Magnetometry

The AGFM (MicroMag 2900, provided by Princeton Measurement, Inc.) is widely used to measure magnetic properties. The principle of this instrument is to utilize the fact that the net translational force on a magnetic material depends on the gradient of the magnetic field and the total magnetic moment of a sample. The output of the AGFM is obtained by measuring the amplitude of the motion of the specimen, which depends on the force experienced by the specimen. The average magnetic field is measured by a Hall probe. The force experienced by the sample is determined by a piezoelectric sensor. The magnetic moment is calculated by comparison to a known standard. One advantage of this technique is the high sensitivity of magnetic moment (about μemu). Figure 3.7 shows a picture of the AGFM.

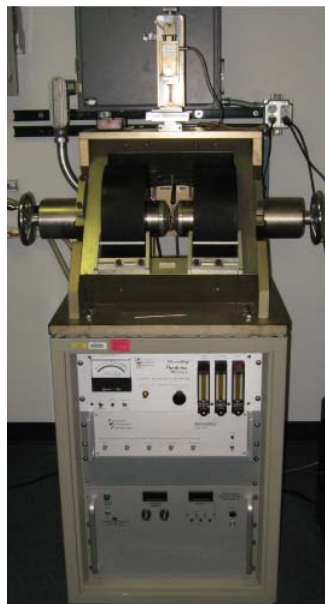


Figure 3.7 MicroMag 2900 AGFM, provided by Princeton Measurement, Inc.

CHAPTER 4 XTEM STUDY ON THE DIFFUSION AND REACTION OF [Fe/Pt]_n MULTILAYER THIN FILMS

4.1 Introduction

Many interesting studies on the diffusion and reaction of [Fe/Pt]_n multilayer thin films have been reported, although a clear understanding is still absent. On the study of the phase formed during the reactions of [Fe/Pt]_n multilayer thin films, it has been reported that the products present in the annealed films are highly dependent on the average composition of annealed films [Ludwig et al. (2006)]. With an average film composition close to Fe₅₀Pt₅₀, the *L1₀* FePt phase was observed. At a composition far from this value, ordered Fe₃Pt or FePt₃ may appear. For [Fe/Pt]_n multilayer films with a large periodicity, however, it has also been found that more than one product phase (i.e., FePt and Fe₃Pt) may appear at the same time [Wang, Berry, and Barmak, unpublished].

Regarding the detailed mechanisms of this solid-state reaction, Endo et al. [Endo et al. (2001); Endo et al. (2003)] reported a larger activation energy for Fe-Pt interdiffusivity than that for *L1₀* FePt phase formation. They concluded that the reaction is diffusion-controlled, i.e., the diffusion of Fe atoms or Pt atoms to the interface is slower than the interface reaction to form the *L1₀* FePt phase. It was further suggested that the *L1₀* FePt phase was the only product of the reaction when the interdiffusion was completed. In an interdiffusion study of [Fe/Pt]_n multilayer films [Zotov et al. (2006)], a reaction-controlled formation was proposed based on the evolution of the *L1₀* superlattice peak intensity with annealing time, which means that the rate of interface reaction to form the *L1₀* FePt phase is smaller than that of the Fe-Pt interdiffusion. From the

magnetic properties of annealed films, Reddy et al. [Reddy et al. (2006)] concluded that a mixture of ordered $L1_0$ and disordered fcc FePt phases co-existed in the annealed nanoscale $[Fe/Pt]_n$ multilayer films. They proposed that the fcc FePt was formed first by interdiffusion, and that the $L1_0$ FePt nucleated from the fcc FePt phase via a disorder-order transformation. A second Fe-Pt interdiffusion study, by Verdier et al. [Verdier et al., (2005)], reported Kirkendall voids within the Pt layer in annealed bulk Fe-Pt multilayer films, suggesting that the diffusion of Pt atoms into the Fe layer is the dominant interdiffusion mechanism. It also indicates that the Fe layers grow at the expense of Pt layer in the diffusion. For thin $[Fe/Pt]_n$ multilayer films, direct examination on the diffusion in nanoscale multilayer samples using microscopy has not been reported, although it has been suggested that the diffusion of Pt atoms into the Fe layer dominates the interdiffusion.

In this chapter, the XTEM studies on the diffusion and reaction of stoichiometric $[Fe_{22nm}/Pt_{28nm}]_6$ multilayer films annealed at 350°C for different times are reported. HCDF TEM imaging is used to characterize the phase distribution of formed $L1_0$ FePt phase in the annealed films. This direct microscopic examination of the structure and phase evolution is helpful to understand the interdiffusion and reaction of $[Fe/Pt]_n$ multilayer thin films.

4.2 Experiments

A $[\text{Fe}_{22\text{nm}}/\text{Pt}_{28\text{nm}}]_6$ multilayer film was sputtered onto a Si(100) substrate having a surface layer of 100 nm of thermally grown SiO_2 . The thickness ratio of 0.78 (Fe:Pt) was chosen to obtain the stoichiometric $L1_0$ composition of 50 at% Fe and 50 at% Pt using the bulk density of Fe and Pt films. A relatively large bi-layer periodicity (50 nm) was chosen in order to examine the intermediate stage of the diffusion and reaction. The deposition rate for Pt was $0.31 \text{ \AA}/\text{sec}$ and that for Fe was $0.48 \text{ \AA}/\text{sec}$, as determined by Rutherford backscattering spectroscopy. The deposition was performed in 4 mTorr of Ar + 3% H_2 . The film samples were annealed in the tube furnace in one atmosphere of flowing Ar + 5% H_2 process gas.

4.3 Results and discussion

As-deposited and annealed $[\text{Fe}_{22\text{nm}}/\text{Pt}_{28\text{nm}}]_6$ films were characterized with XTEM. Figure 4.1 (a) shows the BF TEM image of the as-deposited sample, and Figure 4.1(b) and (c) shows the BF TEM images of the sample annealed at 350°C for 10 and 20 minutes, respectively. The bright stripes in the figures represent the Fe layers (and solid solutions), while the dark layers indicate the Pt layers (and solid solutions). The contrast is mainly due to different mass contrast. The images do not show a distinct product layer in the annealed films. As will be shown later, the product phase has a limited volume fraction, and consists of small grains scattered at the interfaces and grain boundaries of matrix. The evolution of bright and dark stripes is mainly due to the Fe/Pt interdiffusion. By comparing the evolution of Fe and Pt layers upon annealing, it can be seen that the Pt layers grow at the expense of Fe layers. This is consistent with the larger non-equilibrium solubility of Fe atoms in *fcc* Pt (about 75% at 350°C) as compared to that of Pt atoms in *bcc* Fe (15%). These saturation solubilities were estimated from the Fe-Pt equilibrium diagram using two assumptions. One assumption is that the ordered intermetallic phases do not exist, and the (γ Fe, Pt) extends through the whole regions of all ordered intermetallic phases. This assumption of metastable *fcc/bcc* equilibrium is justified by the fact that only a very limited fraction of small $L1_0$ FePt grains scattered widely at the boundaries of matrix. Given this assumption, the solubility of the Fe atoms in *fcc* Pt layers and Pt atoms in *bcc* Fe layers are basically determined with an extrapolation of the *fcc/bcc* phase boundaries from $\sim 600^\circ\text{C}$ to the 350°C annealing temperature (see Figure 1.1). During annealing, the diffusion of Pt atoms into Fe layers

is expected to be limited by the Pt solubility. On the other hand, the diffusion of Fe atoms in the Pt layer should not be limited by solubility for a sample with an overall composition of only 50 at.% Fe. Therefore, once the Pt concentration in the Fe layer reaches saturation, only the interdiffusion of Fe atoms into the Pt layers is expected, which explains the growth of the Pt layers at the expense of the Fe layers.

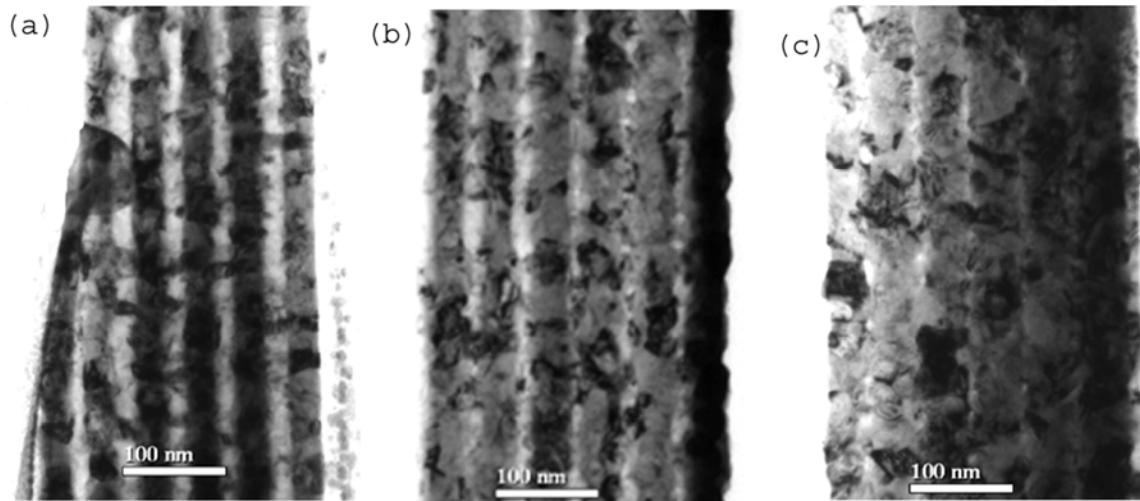


Figure 4.1 The BF XTEM images of sample $[\text{Fe}_{22\text{nm}}/\text{Pt}_{28\text{nm}}]_6$. (a) as-deposited, (b) annealed at 350°C 10 minutes, and (c) annealed at 350°C 20 minutes. The bright stripes represent Fe (or solution) layer, and the dark stripes indicate Pt (or Pt solution).

To further confirm the explanation based on the solubility limitation, the film compositions in the center the Fe layer and Pt layer are measured. Figure 4.2 (a) shows the HAADF STEM image of the film annealed at 350°C for 10 minutes. Figure 4.2 (b), and (c) show the EDX spectrum in the middle of the Fe layer and Pt layer, respectively. As expected, a composition of $\text{Fe}_{79}\text{Pt}_{21}$ was obtain at the Fe layer, and that of $\text{Fe}_{43}\text{Pt}_{57}$ at the Pt layer. It should be pointed out that because of the limited spatial resolution of the

beam probe used in EDX technique, the result may unavoidably be influenced by the surrounding regions. In other words, the Pt composition in Fe layer and Fe composition in Pt layer should be overestimated to some extent. The EDX results showing a much higher composition of Fe in the Pt layer than the Pt in the Fe layer confirms that the Fe-Pt interdiffusion is influenced by the solubility.

A TEM electron diffraction study indicated that $L1_0$ FePt was the only compound formed. Fe_3Pt and $FePt_3$ are not observed. This result is consistent with a previous report [Ludwig et al. (2006)]. The formation of $L1_0$ FePt will be further confirmed with the magnetic properties of the annealed samples, as will be shown later.

It is important to understand the mechanism of *fcc* FePt formation. As shown in the Fe-Pt phase diagram, the *fcc* FePt phase is basically a solid solution of Pt. There might be two possible mechanisms to form the *fcc* FePt phase. The first approach is through the gradual penetration of Fe atoms from the grain boundaries into the Pt grains, as shown in Figure 4.3a. The published bulk diffusivities [Nose et al., (2003); Rein et al., (1978)], however, do not support this mechanism. The estimated diffusion distance, $(Dt)^{1/2}$, is less than 0.003 nm. Therefore, the formation of *fcc* FePt phase is most likely through an alternate mechanism, as shown in Figure 4.3b. In this mechanism, a region of *fcc* FePt forms by nucleation. Its subsequent growth is through the grain boundary diffusion of Pt and Fe atoms. Since this process is generally opposite to that of discontinuous precipitation, we term this “discontinuous dissolution”. Different from that of $L1_0$ phase, the nucleation of *fcc* FePt is expected to have a very small nucleation barrier due to a negligible interfacial energy.

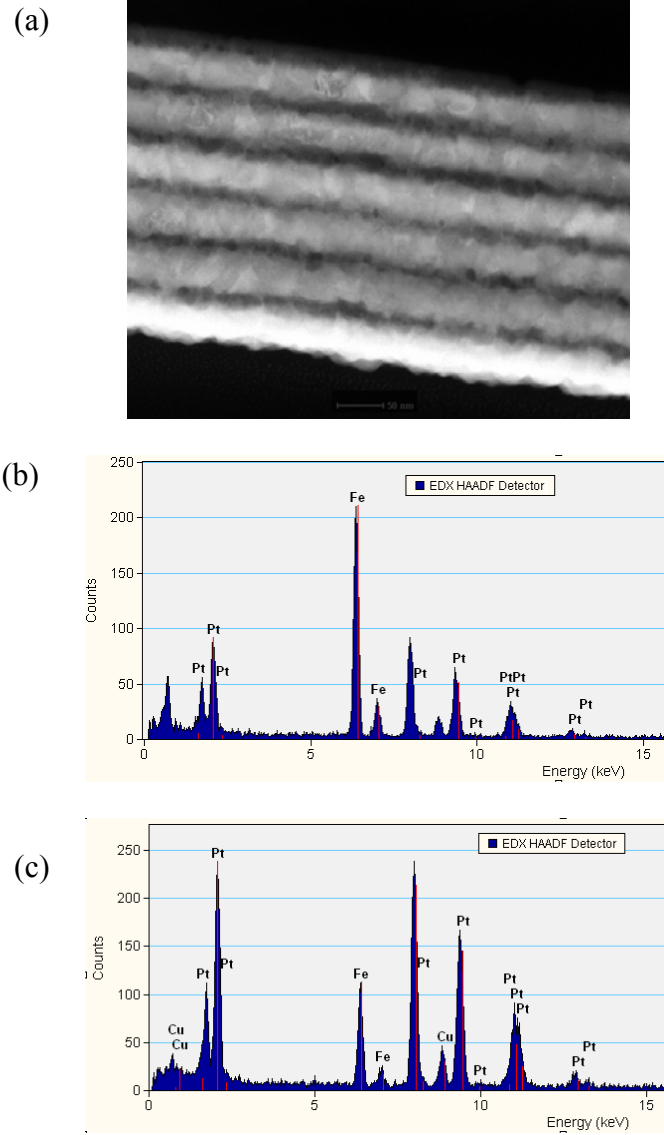


Figure 4.2 (a) The HAADF STEM image of the sample annealed at 350C for 10 minutes, (b) the EDX in the middle of the Fe layer, and (c) the EDX in the middle of the Pt layer.

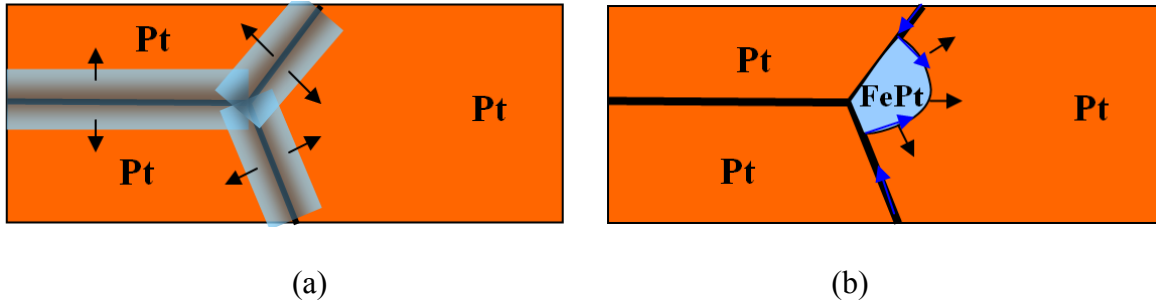


Figure 4.3 The possible *fcc* FePt formation mechanisms. (a) Gradual penetration of Fe atoms into Pt grains, which is not supported by the published diffusivities; (b) Re-nucleation of *fcc* FePt grains and growth by “discontinuous dissolution” via grain boundary diffusion.

The HCDF TEM imaging technique is helpful to examine the location of the product phase within the film sample. Figure 4.4 shows the HCDF TEM images from $L1_0$ 001 and 110 superlattice reflections of the sample annealed at 350°C for 20 minutes, where the small $L1_0$ grains have been circled to differentiate them from single pixel dots due to white noise. The illuminated grains in the image are the $L1_0$ phase grains with 001 or 110 orientations. The HCDF TEM image shows that the $L1_0$ FePt phase grains are widely separated, which is partially due to the fact that only the appropriately orientated $L1_0$ grains are illuminated. However, it can still be concluded that only a small fraction of the sample has transformed to the $L1_0$ FePt phase. In the same figure, it can also be observed that the $L1_0$ phase typically has very small grains located on the grain boundaries and interfaces of matrix. The smaller grain size of the $L1_0$ phase is understood as the result of a recent nucleation event during annealing. These small $L1_0$ grains are also consistent with our plan-view HCDF TEM examination of FePt films annealed at low temperature, as will be shown in Chapter 5. A careful examination of the

TEM image indicates that the $L1_0$ FePt phase grains are distributed somewhat randomly throughout the Fe/Pt bilayer structure and do not consist of well defined layers at the Fe/Pt interfaces. This result is consistent with nucleation of the $L1_0$ phase at sites of low interfacial energy, rather than nucleation events occurring only at the Fe/Pt interfaces due to limited availability of Fe or Pt atoms, i.e., diffusion.

Above results demonstrate that a mixture of $L1_0$ FePt and fcc FePt phases is achieved in the annealed films. The fcc FePt is a solid solution of the initial Pt layer, which is formed by the diffusion of Fe atoms into Pt layer and does not require re-nucleation of grains (although this may occur). The $L1_0$ FePt phase is formed at least partially by nucleation and growth in the disordered fcc matrix and can thus be considered a disorder-order phase transformation.

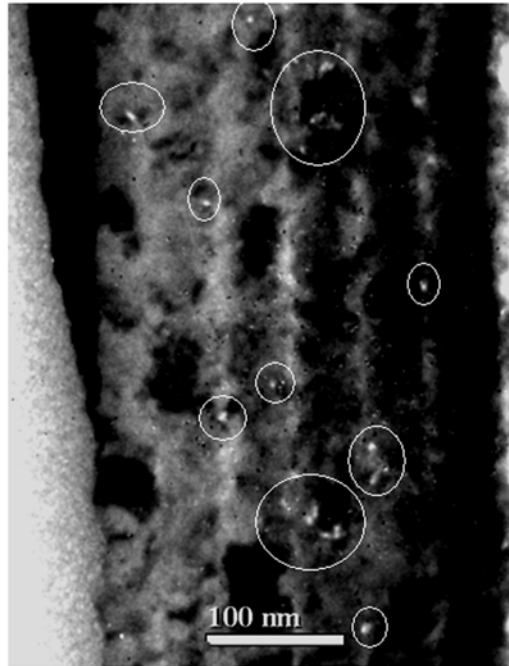
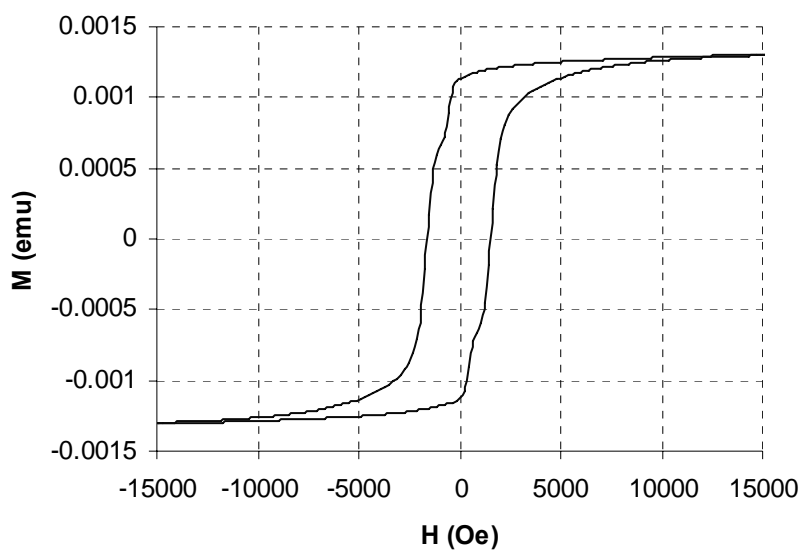


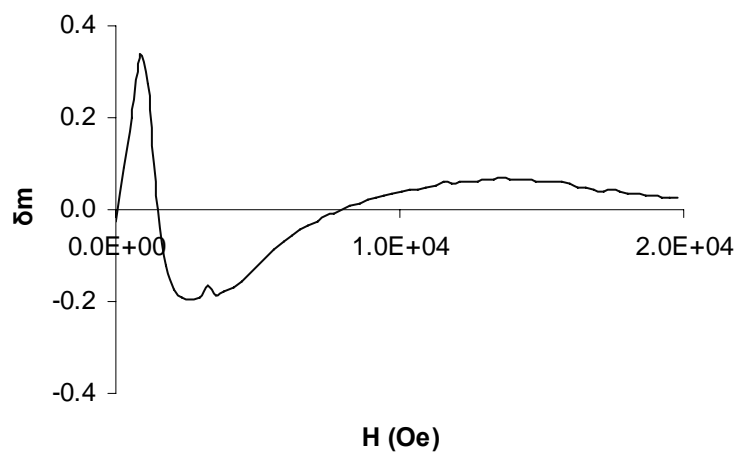
Figure 4.4 HCDF TEM image of sample $[\text{Fe}_{22\text{nm}}/\text{Pt}_{28\text{nm}}]_6$ annealed at 350°C for 20 minutes. The image was formed using the 001 and 110 reflections of $L1_0$ FePt phase. The illuminated $L1_0$ FePt phase grains are circled out to be differentiated from the CCD noise in pixel size.

The magnetic properties the sample annealed at 350°C for 20 minutes are shown in Figure 4.5, including both the M-H hysteresis curves and the Henkel plot of δm . As can be seen from the hysteresis curve (Figure 4.5a), the sample is not saturated until above 10kOe, and has a coercivity of 1.7kOe. The results clearly confirm the appearance of $L1_0$ FePt phase, since it is the only phase having a large magnetocrystalline anisotropy in the Fe-Pt system. The presence of remaining soft phases (Fe or disordered FePt) is evidenced by the kink of the demagnetizing curve near zero field. The kink is formed

because the soft phase can be reversed at a small magnetic field, while the hard phase can only be reversed at higher field. However, the volume fraction of the soft phase can only be roughly estimated from the M-H loop because of the existence of exchange coupling of the soft phase and hard phases, which is clearly demonstrated by the Henkel plot of δm (Figure 4.5b). The Henkel plot of δm is defined as $\delta m = \{ m_d(H_m) - [1-2m_r(H_m)] \}$, where $m_r(H_m)$ is the remanent polarization after application of a field H_m to the thermally demagnetized sample (measured on the magnetization curve) and $m_d(H_m)$ is the remanence after demagnetizing the saturated sample in a reverse field H_m (measured on the demagnetization curve) [O'Grady et al.(1993); Bollero et al.(2002)]. Both the $m_r(H_m)$ and $m_d(H_m)$ were normalized with the remanence of the material after saturation was attempted at high magnetic field. This Henkel plot is commonly used to study the interactions between the grains, where the positive peak is caused by exchange-coupling interactions, while the negative peak is introduced by magneto-static (or dipole) interactions. It can be seen from Figure 4.5(b) that both types of interactions are present in the sample. Since part of the soft phase is exchange coupled with the hard phase, it will be reversed along with the hard phase, and won't contribute to the moment change at the kink point. Therefore, it can be understood that the determination of the soft phase fraction from the M-H hysteresis curve is difficult due to the presence of the exchange coupling.



(a)



(b)

Figure 4.5 (a) The M-H hysteresis curve, and (b) the Henkel plot of δm of sample $[\text{Fe}_{22\text{nm}}\text{Pt}_{28\text{nm}}]_6$ after annealed at 350°C 20 minutes.

4.4 Conclusions

This chapter reports our studies of the diffusion and reaction of a $[\text{Fe}_{22\text{nm}}/\text{Pt}_{28\text{nm}}]_6$ multilayer film annealed at 350°C for two different times with XTEM. It was found that the Pt layers grow at the expense of Fe layers, which indicates that Fe atom diffusion into the Pt layers dominates the diffusion process. The disparity in solubility is used to explain this phenomenon. HCDF TEM is used to identify the $L1_0$ FePt phase grains present in the sample. It was observed that the $L1_0$ phase grains are much smaller than the fcc phase grains, and they are mainly located at the fcc grain boundaries and at the Fe/Pt interfaces of the sample. A mixture of ordered $L1_0$ and disordered fcc FePt phase grains in these annealed films was evident. The fcc FePt is the solid solution of Pt and Fe, and the formation of fcc FePt phase is believed to occur through nucleation and growth at such low annealing temperature. The $L1_0$ FePt phase formation also requires nucleation events, and can be formed through the reaction of the Fe and Pt directly, or via a disorder-order phase transformation from the fcc FePt solid solution.

CHAPTER 5 THE INFLUENCE OF PERIODICITY AND DEPOSITION TEMPERATURE ON THE DIFFUSIVITY, STRUCTURE AND MAGNETIC PROPERTIES OF ANNEALED MULTILAYER FILMS

5.1 Introduction

In Chapter 4, it was concluded that a mixture of $L1_0$ and fcc FePt phases is obtained upon annealing of Fe/Pt multilayer films. The structure (including grain size, volume fraction, and ordering et al.) of the $L1_0$ phase is very important to the properties of films. On the other hand, the structure of $L1_0$ FePt phase in the annealed films is highly dependent on the fabrication and processing of thin films. In this and following chapters, a more comprehensive characterization of the annealed films will be conducted to understand the processing-structure-property relations.

The periodicity (the bi-layer thickness) and the deposition temperature are two important parameters of multilayer films. For films with a fixed thickness, the periodicity determines the diffusion distance, the number of interfaces /layers, and the microstructure of as-deposited films. In multilayer films, the diffusion drives the long-distance atomic transport, which makes the nucleation and growth of new compounds through the interface reaction possible. The layer interface can also serve as favorable nucleation sites of the product compound. Obviously, a small periodicity gives more layers or interfaces, and a large periodicity results in longer diffusion distance and large grains. For epitaxial $[Fe/Pt]_n$ multilayer films, it has been found that the periodicity has a significant influence on the structure and magnetic properties of films. This has been observed in sputtered thin films [Chou et al. (1004) I, II, Hufnagel et al., (1999)] and in

severely plastically deformed multilayer films [Verdier et al., (2005); Han et al., (2002)]. For example, using high-resolution TEM examination, Han et al. found that the stable Fe *bcc* phase layer sequentially becomes a distorted *bcc*, and *fcc* phase as the period is decreased below 76Å [Han et al., (2002)]. Chou et al. investigated the influence of period on the magnetic properties of annealed epitaxial [Fe/Pt]_n multilayer films on [001] Al₂O₃ substrates, and found that both the in-plane and out-of-plane coercivity increase with the decrease of period (in the range of 10Å~6Å) [Chou et al. (1004) I; Chou et al. (1004) II]. For polycrystalline [Fe/Pt]_n films, the magnetic properties [Luo et al., (1995); Raghavendra Reddy et al., (2006); Liu et al., (1998); Seki et al., (2006)] have been widely reported, but comprehensive studies on the influence of periodicity for such films have not been reported.

The deposition temperature of multilayer samples is expected to influence the structure of the interface. For example, if the temperature is high enough, long-distance diffusion occurs during the deposition and multilayer structures will not be achieved. At a medium deposition temperature, local interdiffusion at the interface may occur. At lower temperature, the interface is expected to be sharper. On the other hand, the temperature also influences the grain size of as-deposited films. A small grain size is expected for samples prepared at low temperature. Another factor influenced by the deposition temperature is the stress in the as-deposited films. Higher deposition temperature may be helpful to release the stress caused by the misfit at the interface. During epitaxial multilayer film preparation, the temperature is extremely important to the quality of the single crystal films. For polycrystalline [Fe/Pt]_n multilayer films, the

influence of substrate temperature on the structure and properties has not been previously reported.

This chapter focused on the processing-structure-properties relations of two sets of multilayer films, one with varying deposition temperature and the other with different periodicity. The average film composition and the total film thickness were kept the same. As will be shown, both the deposition temperature and periodicity of $[\text{Fe}/\text{Pt}]_n$ multilayers have a significant influence on the effective Fe-Pt interdiffusivity, the microstructure, and magnetic properties of the annealed films. It will also be shown that the magnitude of the effective interdiffusion coefficient, the Ll_0 grain size, and the long-range order parameter were positively correlated for the samples investigated.

Before the detailed description of the experiment and results, the techniques used to determine the Fe-Pt interdiffusivity, volume fraction of Ll_0 FePt phase, long-range order parameter, the grain size, and the nucleation/grain density of the Ll_0 FePt phase will be described.

5.2 Methods

5.2.1 Interdiffusivity measurement in $[\text{Fe/Pt}]_n$ multilayer films

It has been commonly accepted that the interdiffusion of Fe and Pt at the interface is beneficial for the formation of $L1_0$ FePt at low processing temperature. The investigation of the correlations of interdiffusivity, the structure, and magnetic properties of annealed films is therefore significant. Another reason to study the interdiffusivity is the necessity to design the annealing temperature and time. Because of a limited layer thickness of $[\text{Fe/Pt}]_n$ multilayer thin films, the annealing temperature and time are located in a narrow window in order to find an intermediate stage.

Many efforts [[Endo et al., \(2003\)](#); [Mehrer \(1990\)](#); [Kushida et al., \(2003\)](#); [Nose et al., \(2005\)](#)] have been made to measure the bulk Fe-Pt interdiffusivity and to understand the relationship between interdiffusivity and the formation of $L1_0$ FePt phase in multilayer films. In these studies, bulk diffusion couples (usually in μm scale) of polycrystalline or single crystals are commonly used. The standard Boltzmann-Matano analysis is widely used to determine the diffusivity, and the composition profile of annealed sample was usually measured with Auger Electron Spectroscopy (AES), RBS, et. al.. However, it has been demonstrated in both theory and experiments that the effective interdiffusivity (D_Λ) in nano-scale multilayer films can deviate significantly from the bulk interdiffusivity due to the influence of the steep compositional gradient and coherent strains in multilayers [[Greer \(1997\)](#); [Chang et al., \(1985\)](#); [Gupta et al., \(1988\)](#); [Philofsky et al., \(1969\)](#); [Cook et al., \(1969\)](#)]. In a small local region (i.e., several nanometers) of a bulk diffusion couple, the composition gradient is usually very small

and the interface strain can also be negligible. In multilayer thin films, however, the periodicity is usually several nanometers or even less. The large compositional gradient and the interface strain play a very important role on the free energy and the interdiffusivity. The approach used to study the free energy and the diffusivity in the nanoscale multilayer thin films was originally used for the study of spinodal decomposition, which is essentially the reverse process of homogenization of multilayers. Appendix “A” provides a more detailed understanding of the influence of the compositional gradient and strain on the free energy and the diffusivity. It clearly demonstrates that the measured bulk diffusivity may not be useful to understand the interdiffusion of multilayers. The role grain boundary diffusion in polycrystalline multilayers is a further complication.

However, the effective interdiffusivity in multilayers can be directly determined from the decay rate of the intensity of low angle XRD peaks due to thermal treatments. The repetitive layer pairs of different X-ray scattering strength in the multilayers induce small angle XRD peaks around the (000) reflection (direct beam), and the decay of these peaks due to annealing is directly related to the homogenization of these compositionally modulated layers. The effective interdiffusivity D_A is given by the decay rate of the first small angle peak intensity $I(t)$ during annealing, as shown in Equation 5.1. Appendix “A” gives a derivation of this expression.

$$D_A = -[\Lambda^2/(8\pi^2)] d\{\ln[I(t)/I(0)]\}/dt \quad (5.1)$$

where $I(0)$ is the initial integrated intensity of as-deposited films, Λ is the bi-layer period (i.e., sum of the thickness of a single Pt and a single Fe layer), and t is the annealing time. The values of $I(t)$ and $I(0)$ can be measured through low angle XRD, and

the values of t and L are known. This method has been applied to measure the interdiffusivity of a large variety of material systems such as Si/SiGe[Prokes et al., (1990); Aubertine et al., (2003)], Mo/Si[Nakajima et al., (1988)], Cu/Pd[Philofsky et al., (1969)], GaAs/AlAs[Fleming et al., (1980)], and Au/Ag[Cook et al., (1969)] multilayers. Most recently, Se-Young et al. [Se-Young et al., (2006)] and Zotov et al. [Zotov et al., (2006)] used this approach to measure the effective Fe-Pt interdiffusivity of $[\text{Fe/Pt}]_n$ multilayers. Interestingly, they found that the effective interdiffusivity differed for different Fe-Pt multilayers, which, in part, motivates this more comprehensive study.

5.2.2 Volume fraction of $L1_0$ FePt phase

From the previous chapter, it is understood that the films annealed at low temperature generally give a mixture of disordered fcc phase and the $L1_0$ FePt phase. Because the disordered fcc FePt has a small anisotropy energy, which lacks attractive magnetic properties, the volume fraction of the ordered $L1_0$ FePt phase is therefore very important to the magnetic properties of the annealed films. For example, Ristau and Barmak et al. had demonstrated that the volume fraction of $L1_0$ FePt phase is proportional to the coercivity of the FePt films [Barmak et al., (1996); Ristau et al., (1999)]. For magnetic recording using FePt thin films or nanoparticles, the $L1_0$ phase fraction, along with its grain/particle size, will strongly influence the maximum recording density.

The fraction of an ordered phase present in a two phase mixture of the disordered and ordered phases can be very difficult to quantify in thin films, and this is especially true for films of the FePt $L1_0$ phase. Quantitative X-ray diffraction is of limited utility because the degree of chemical order of the $L1_0$ phase, as well as its volume fraction, result in similar changes to the relative intensity of the fcc FePt peaks as compared to the superlattice peaks of $L1_0$ FePt phase. The tetragonal distortion that occurs with ordering is small, and in fine-grained thin films separate quantification of the intensities of the closely related peaks is difficult. For example, there is typically considerable overlap amongst the fcc $\{002\}$ peak, the $L1_0$ (002) peak, and the $L1_0$ (200)+(020) peak. Effectively, it is impossible to find an individual peak solely from the disordered fcc phase. Transmission electron microscopy (TEM) has been used successfully to determine the phase fraction of $L1_0$ FePt phase in highly (111) textured FePt and CoPt films by Ristau and Barmak et al. [Barmak et al., (1996); Ristau et al., (1999)]. Their

approach is to select individual grains with their 111 zone axis strictly parallel to the electron beam, so that all three $L1_0$ FePt {110} variants potentially nucleated inside one grain are visible, and can be illuminated individually in HCDF TEM images. The sum of all illuminated areas in the DF images from superlattice {110} reflections represents all ordered regions, and the ratio of the area of all ordered regions to that of the whole grain gives the $L1_0$ phase fraction of one single grain. Repeating this process for multiple grains determines the $L1_0$ phase fraction of one sample. It can be seen that this method is very laborious even for highly (111) textured films with large grains (such as films annealed at 700°C). For films with a much smaller grain size, the application of this technique becomes even more difficult.

The ordered $L1_0$ FePt phase has a tetragonal structure slightly distorted from that of the disordered fcc phase. In the disordered phase, each position is occupied by Fe and Pt atoms with the same probability. In the ordered $L1_0$ phase, however, the Fe and Pt atomic layers occupy the structure alternatively along the $\langle 001 \rangle$ direction. Consequently, the “ c ” axis of the $L1_0$ structure is slightly smaller than that of the “ a ” and “ b ” axis. A typical selected area diffraction pattern (SADP) of a film containing both the ordered $L1_0$ and disordered fcc FePt phase is shown in Figure 5.1. Both phases share the same fundamental reflections such as 111, 200, 220, 311, et. al.. Among these, the 200 and 220 rings are each split into two rings due to the reduction of symmetry of $L1_0$ structure compared to that of fcc phase. However, the distortion is so small that the split rings can not be separated effectively. Therefore, for simplicity, the split rings will be handled together, and labeled as $\{200\}_{fcc+L1_0}$, $\{220\}_{fcc+L1_0}$. The remaining reflections in Figure 5.1 are the superlattice reflections scattered solely from the $L1_0$ phase, and labeled

as 001_{L1_0} , 110_{L1_0} , 201_{L1_0} , 112_{L1_0} . Table 5.1 lists the planes contributing to the reflections. It should be noted that the multiplicity of 001_{L1_0} and 110_{L1_0} is only 1/3 that of the $\{200\}_{fcc+L1_0}$, or $\{220\}_{fcc+L1_0}$.

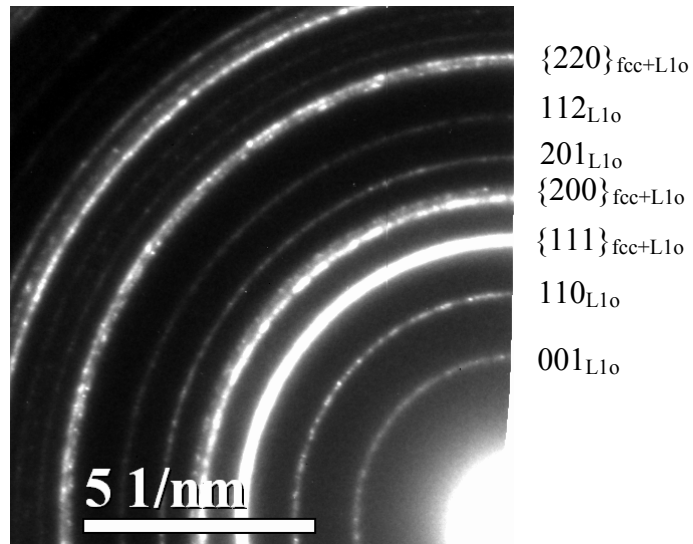


Figure 5.1 Portion of a TEM SADP of a film containing both ordered $L1_0$ and disordered fcc FePt phases.

Table 5.1 The reflections along with the contributing planes

Reflections	Planes contributing the reflection
001_{L1o}	$(001)_{L1o}$
110_{L1o}	$(110)_{L1o}$
$\{200\}_{fcc+L1o}$	$(200)_{fcc}$; $(020)_{fcc}$; $(002)_{fcc}$; $(200)_{L1o}$; $(020)_{L1o}$; $(002)_{L1o}$
201_{L1o}	$(201)_{L1o}$
112_{L1o}	$(112)_{L1o}$
$\{220\}_{fcc+L1o}$	$(220)_{fcc}$; $(202)_{fcc}$; $(022)_{fcc}$; $(220)_{L1o}$; $(202)_{L1o}$; $(022)_{L1o}$

The HCDF TEM technique forms a dark field TEM image using one or more whole ring(s), excluding the direct beam and other reflections. Notationally, we will use HCDF (hkl) to refer to the dark field image formed from the (hkl) diffraction ring. For example, HCDF (001_{L1o}) indicates the dark field TEM image using the 001 superlattice ring of $L1_0$ FePt phase. The grains illuminated in HCDF (001_{L1o}) indicate all the $L1_0$ FePt grains having (001) planes parallel to the electron beam. Correspondingly, the illuminated grains in HCDF ($\{200\}_{fcc+L1o}$) represent all the fcc and $L1_0$ phase grains with their (200), (020), and (002) planes parallel to the electron beam.

The technique introduced in this paper is based on the measurement of the illuminated grain areas in HCDF TEM images generated from specific diffraction rings. In theory, for polycrystalline samples consisting of a single layer of randomly oriented grains (without strong texture), the volume fraction of $L1_0$ FePt phase (f_{L1o}) can be decided by Equation (5.1).

$$f_{L1o} = \frac{3 \times \text{area}_{HCDF(001_{L1o})}}{\text{area}_{HCDF(\{200\}_{L1o+fcc})}} \quad (5.1)$$

where the $area_HCDF()$ function is defined as the total illuminated grain area in the HCDF TEM images from the specific reflection(s), or planes in the brackets.

For quantitative implementation of Equation (5.1), the assumptions implicitly used in its derivation need to be considered. One such assumption is that for the $L1_0$ FePt phase, the $(001)_{L1_0}$ oriented grains illuminated in HCDF (001_{L1_0}) are also the same illuminated as $(002)_{L1_0}$ in HCDF $(\{200\}_{fcc+L1_0})$, as stated in Equation (5.2).

$$area_HCDF(002_{L1_0}) = area_HCDF(001_{L1_0}) \quad (5.2)$$

Another implicit assumption of Equation (5.1) is that 200_{L1_0} , 020_{L1_0} , and 002_{L1_0} planes have the same probability to be illuminated, as stated in Equation (5.3).

$$area_HCDF(200_{L1_0} + 020_{L1_0} + 002_{L1_0}) = 3 \times area_HCDF(002_{L1_0}) \quad (5.3)$$

This assumption holds true for random or slightly orientated samples, but may not be appropriate for highly textured films. The nature of texture in thin films is that certain preferred planes (i.e., 111) lie in the film plane; and the film may possess a distribution of random grains and textured grains for weakly textured films. During TEM examination, the TEM samples can be tilted away from the texture axis so that the textured grains do not satisfy the Bragg reflection [[Tang and Laughlin \(1996\) I; II](#)]. In the tilted orientation (10 degree away in this thesis), the illuminated grains can thus be assumed to be randomly oriented. In the general case, the volume fraction of ordered phase present in the sample can be calculated if it is assumed that the ordered fraction of the randomly oriented grains is equal to the ordered fraction of the textured grains, or it may be assumed that the volume fraction of textured grains is negligible. For the work presented here, the plan view samples were tilted away from the texture direction to minimize the

potential influence of textured grains, although no detectable textures were found for the samples.

Another practical problem is to distinguish the closely positioned rings for dark field imaging, specifically the $\{200_{L10+fcc}\}$ ring and the $112_{L10} + 201_{L10}$ rings. At the normal operating voltage (300 kV) of the microscope used in this study (Tecnai F30) the available objective apertures were too large to select only the $\{200_{Lcc+fcc}\}$ reflection while excluding neighboring reflections. Two solutions were developed and used and are described in detail below.

The first solution is to reduce the beam voltage to 100 kV, which increases the relative size of SADP to the objective aperture. While this improvement is insufficient to allow the $\{200_{Lcc+fcc}\}$ ring to be individually selected, it does allow individual selection of the $112_{L10} + 201_{L10}$. Equation (5.4) is then used to calculate the total illuminated grain area of the $\{200_{L10+fcc}\}$ ring as the difference between the illuminated grain area of the combined $\{200_{L10+fcc}\}$ and $112_{L10} + 201_{L10}$ rings and illuminated grain area of the $112_{L10} + 201_{L10}$ ring.

$$\begin{aligned} & area_HCDF(\{200\}_{L10+fcc}) \\ &= area_HCDF(\{200_{L10+fcc}\} + 201_{L10} + 112_{L10}) - area_HCDF(201_{L10} + 112_{L10}) \end{aligned} \quad (5.4)$$

The determination of the area of illuminated grains in a dark field TEM image requires the accurate separation of the illuminated grains from the background based upon contrast (i.e., intensity). Because of the uniform (not bimodal) distribution of grain contrast present in the images, the selection of an intensity level to distinguish the illuminated grains from the background intensity is subject to arbitrary variation by the operator, and hence uncertainty in the illuminated grain area in the image and potential error in the ordered fraction calculated. To eliminate this potential source of error in the

calculation of the ordered fraction, only the $\text{HCDF}(\{200\}_{L10+fcc}+201_{L10}+112_{L10})$ image is manually contrast selected to identify the illuminated grains. All other HCDF images (from the (001_{L10}) ring and from the $(201_{L10}+112_{L10})$ ring) are projected onto the contrast selected $\text{HCDF}(\{200\}_{L10+fcc}+201_{L10}+112_{L10})$ binary image and areas calculated based only on grains present in the initial $\text{HCDF}(\{200\}_{L10+fcc}+201_{L10}+112_{L10})$ image. In this way, all the illuminated grains experienced the same initial contrast selection uncertainty and the relative uncertainty of area fractions are unaffected.

Details of the image processing will be described below with a specific example. For each TEM field of view, three HCDF images, $\text{HCDF}(\{200\}_{L10+fcc}+201_{L10}+112_{L10})$, $\text{HCDF}(201_{L10}+112_{L10})$ and $\text{HCDF}(001_{L10})$, were obtained as above. Figure 5.2 shows a bright field and the three HCDF TEM images of a typical view. The following processing steps were used to determine the volume fraction of $L1_0$ FePt phase present.

(1) The $\text{HCDF}(\{200_{L10+fcc}\}+201_{L10}+112_{L10})$ image, Figure 5.2(b), was contrast selected to separate illuminated grains from the background. This contrast selected image is shown as Figure 5.2(e). A comparison of $\text{HCDF}(\{200_{L10+fcc}\}+201_{L10}+112_{L10})$, $\text{HCDF}(201_{L10}+112_{L10})$, and $\text{HCDF}(001_{L10})$ reveals that the illuminated grains in $\text{HCDF}(201_{L10}+112_{L10})$, Figure 5.2(d), have a much weaker intensity. This is not coincidental, as will be discussed in detail later. The lower intensity of the $(201_{L10}+112_{L10})$ orientated grains in the $\text{HCDF}(\{200_{L10+fcc}\}+201_{L10}+112_{L10})$ image allows them to be separated out from the $(\{200\}_{L10+fcc})$ grains by contrast, using the $\text{HCDF}(201_{L10}+112_{L10})$ image as a guide to the appropriate contrast level to be used. The effectiveness of the approach can be clearly confirmed by a comparison of Figure 5.2(d) and Figure 5.2(e).

- (2) The enlarged contrast selected binary image, i.e., Figure 5.2(e) in the example, was printed on a transparency film, and the enlarged HCDF(001_{L10}) (Figure 5.2c) image was printed on a paper. The same magnifications are used.
- (3) The next step is to overlap the printed transparent films, showing the {200}_{fcc+L10} illuminated grain, onto the printed paper showing the (001)_{L10} illuminated grains. On the transparency film all the (001)_{L10} grains were circled out. The 001_{L10} grains were identified by the fact that they are illuminated on both the transparency film and paper. This step accomplishes the projection of the (001)_{L10} illuminated grains onto the {200}_{fcc+L10} illuminated grain.
- (4) The circled 001_{L10} grains were changed to a different grey level (light grey level in example) with the software, as shown in Figure 5.2(f). Therefore, the light grey level in Figure 5.2(f) shows 001_{L10} grains, while the light grey level and dark grey level together give {200_{L10+fcc}} grains. The area fraction of 001_{L10} grains to {200_{L10+fcc}} grains gives the volume fraction of $L1_0$ FePt phase based on Equation (5.1). The volume fractions of different grey levels were measured with Image J software.
- (5) For each sample, multiple views (usually above 5) are necessary to get an acceptable standard deviation (<5%).

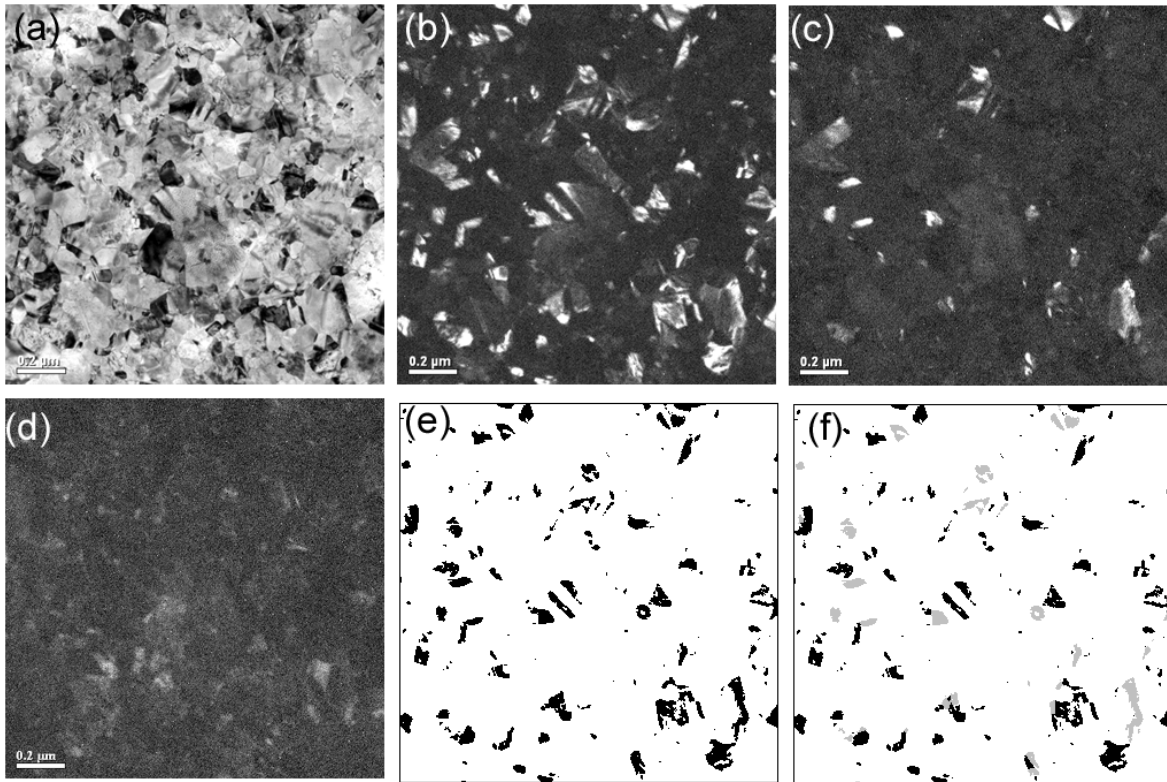


Figure 5.2 The (a) bright field, (b) $\text{HCDF}(\{200_{L10+fcc}\}+201_{L10}+112_{L10})$, (c) $\text{HCDF}(001_{L10})$, (d) $\text{HCDF}(201_{L10}+112_{L10})$, (e) contrast selected $\text{HCDF}(\{200_{L10+fcc}\}+201_{L10}+112_{L10})$, and (f) processed binary TEM images of a typical multilayer sample annealed at 500°C for 30 minutes. In the processed image, the light grey level grains indicate $L1_0$ phase grains with 001 planes illuminated, and the dark grains indicates all fcc grains with $\{200\}$ family planes illuminated, as well as the $L1_0$ grains with 200 or 020 planes illuminated.

A second solution is based upon Equation (5.5), as a modified technique applicable to samples processed at lower temperature ($\leq 500^{\circ}\text{C}$). In this approach, only two HCDF images, $\text{HCDF}(001_{L10} + 110_{L10})$ and $\text{HCDF}(\{200+220\}_{L10+fcc} + 112_{L10} +$

201_{L10}) are required at each view, and it is assumed that contrast can be used to eliminate the 112_{L10} and 201_{L10} oriented grains from inclusion in the {200+220}_{L10+fcc} grain area determination.

$$f_{L10} = \frac{3 \times \text{area_HCDF}(001+110)_{L10}}{\text{area_HCDF}(\{200+220\}_{L10+fcc})} \quad (5.5)$$

This assumption has been confirmed as valid by both TEM image observations and calculations of scattered electron intensity at both 100kV and 300kV. During implementation of the first solution (described above) it was observed that the illuminated grains from 201_{L10} and 112_{L10} reflections had much lower intensities than that from 001_{L10}, 110_{L10}, {200+220}_{fcc+L10} reflections. This observation spanned a total of more than 50 views and 10 samples annealed at or below 500°C. A simple diffraction intensity evaluation of the different reflections using Howie-Whelan equations was conducted [Williams et al., (1996)] and the results are shown in appendix “B”, which are very consistent with the experimental observations. For films annealed at or below 500°C, the *L10* FePt phase has a relatively lower long range order parameter (S) and a much lower illumination intensity from the 201_{L10} and 112_{L10} reflections is induced by their small scattering abilities and their reduced extent of chemical order. Accordingly, an appropriate selection of contrast level to distinguish the illuminated grains from background can also be readily used to distinguish the {200+220}_{fcc+L10} illuminated grains from the 201_{L10} and 112_{L10} illuminated grains, without reference to a separate HCDF(201_{L10} + 112_{L10}) image. This minimizes the effort required for measurements, as only two HCDF images are now required to calculate the ordered fraction present. The TEM image acquisition and processing otherwise follow the same procedures as described for the first solution above.

It is worth noting that for films annealed at high temperature (i.e, 700°C), the films may be highly ordered with S close to 1 and correspondingly, the intensity of $(201+112)_{L10}$ illuminated grains in the dark field image may be comparable to that of $(001+110)_{L10}$, and $\{200+220\}_{L10+fcc}$. In this case, the use of contrast to distinguish the grains can not be used and the third HCDF image is required.

5.2.3 Long-range order parameter

The measurement of the LI_0 volume fraction answers the question how much of the sample is the ordered phase. The long-range order parameter is used to determine how well the LI_0 FePt phase present in the sample is ordered.

Three techniques will be applied to examine the extent of chemical ordering. The first one, as shown in equation 5.6, is based on the integrated intensity ratio of selected pair of superlattice and fundamental peaks.

$$S^2 = \frac{\left(\frac{I_{001}}{I_{002}} \right)_{\text{measured \& corrected}}}{\left(\frac{I_{001}}{I_{002}} \right)_{S=1}} \quad (5.6)$$

where 001 is the superlattice peak, and 002 is the fundamental peak. Similar pairs such as 110 and 220 are also commonly used. The value of $\left(\frac{I_{001}}{I_{002}} \right)_{\text{measured \& corrected}}$ is the measured integrated intensity ratio through curve fitting, while $\left(\frac{I_{001}}{I_{002}} \right)_{S=1}$ is the calculated intensity ratio for perfectly ordered ($S=1$) FePt phase.

Before applying above equation, the XRD instrument was first calibrated with standard Si powders provided by NIST. The instrument calibration was based on the measured peak intensity and calculated peak intensity of standard Si powders. The Si powders were mixed with epoxy, and then pasted on a piece of glass and baked at 80°C in a flow of reducing gas for one hour. The Si powders have a size of about 2.60~8.13µm. The scanned XRD pattern is shown in Figure 5.3. The extracted integrated peak intensity was shown in Table 5.2.

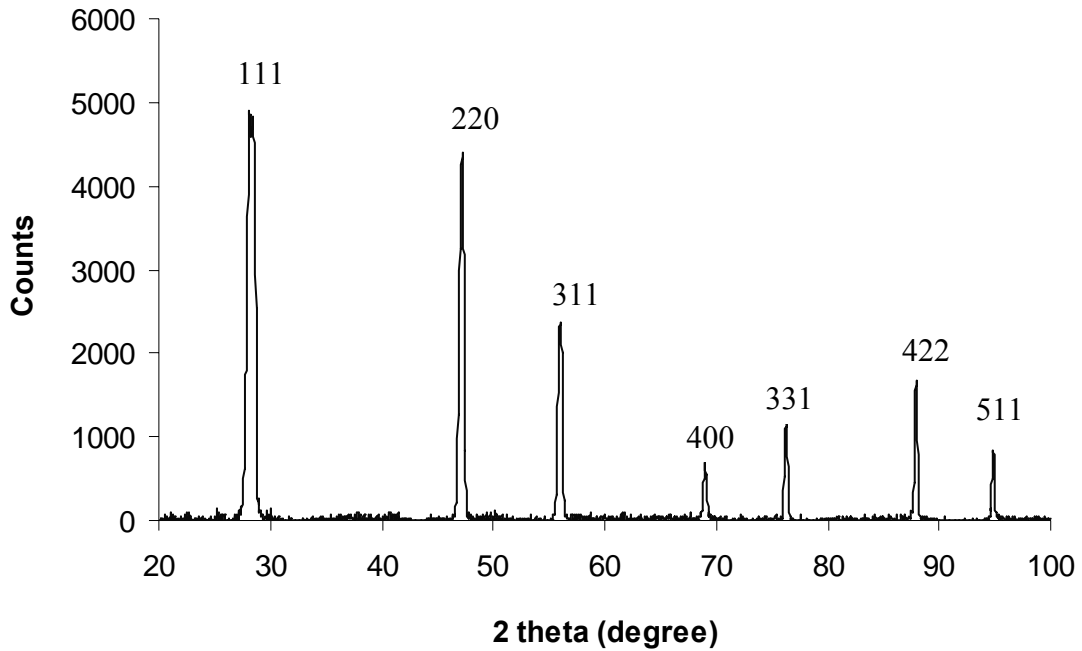


Figure 5.3 XRD of standard Si powder

The calculation of the integrated peak intensity of Si peaks is based on equation 5.7.

$$I = |F|^2 p \left(\frac{1 + \cos^2 2\alpha \cos^2 2\theta}{\sin^2 \theta \cos \theta} \right) e^{-2M} \quad (5.7)$$

where F is the structure factor, p is the multiplicity factor, 2α is the diffraction angle in the graphite monochromator (26.38°), $\left(\frac{1 + \cos^2 2\alpha \cos^2 2\theta}{\sin^2 \theta \cos \theta} \right)$ is the Lorentz-polarization factor, and e^{-2M} is the temperature factor. Because the Si paste has a thickness of several milli-meters, it can be considered to be “infinitely thick”. In this case, the absorption factor is independent of θ , and does not come into the expression. The values of all terms and calculated integrated intensity of Si peaks are listed in Table

5.2. All terms in the table, except the temperature factor, are easy to determine. The temperature factor of Si in the table is from the reference [Zhang et al., (1990)], which is derived from the neutron diffraction of Si material.

Table 5.2 The calculated and measured XRD peaks of Si powders

Peak	2θ	$ F ^2$	p	L-P	M	$I_{\text{calculated}}$	I_{measured}
111	28.44	3329.0	8	27.704	0.011	721044	84341
220	47.30	4821.9	12	9.288	0.031	505483	45783
311	56.12	2124.2	24	6.399	0.042	299854	22821
400	69.13	3586.6	6	4.157	0.061	79140	5023
331	76.38	1631.1	24	3.477	0.073	117670	8698
422	88.03	2800.1	24	2.883	0.092	161204	10873

The ratios of measured to calculated intensity of Si peaks, after normalization to 1 at Si (111) peak (2θ of 28.44°), are shown in Figure 5.4. The calibration factor is defined as the normalized ratio here. It can be seen that an ideal horizontal line at 1 was not achieved; instead, the measured peak intensity drops with the increase of scanning angle. The curve in Figure 5.4 was fitted to serve as the instrument calibration curve in order to determine the S of LI_0 FePt phase.

Considering the instrument calibration factor, Equation 5.6 was modified as the form of Equation 5.8, used to determine S of LI_0 FePt. The coefficient of 0.691 is determined from the calibration curve (Figure 5.4) at 2θ value of 001 and 002 peaks of LI_0 FePt phase at 24° and 49° , respectively.

$$S^2 = \frac{0.691 \times \left(\frac{I_{001}}{I_{002}} \right)_{measured}}{\left(\frac{I_{001}}{I_{002}} \right)_{S=1}} \quad (5.8)$$

The integrated intensity ratio for perfectly ordered FePt, $\left(\frac{I_{001}}{I_{002}} \right)_{S=1}$, was calculated based on Eq. 5.9.

$$\left(\frac{I_{001}}{I_{002}} \right)_{S=1} = \frac{\left\{ A_{001} |F|^2 p \left(\frac{1 + \cos^2 2\alpha \cos^2 2\theta}{\sin^2 \theta \cos \theta} \right)_{001} \cdot e^{-2M} \right\}_{001}}{\left\{ A_{002} |F|^2 p \left(\frac{1 + \cos^2 2\alpha \cos^2 2\theta}{\sin^2 \theta \cos \theta} \right)_{002} \cdot e^{-2M} \right\}_{002}} \quad (5.9)$$

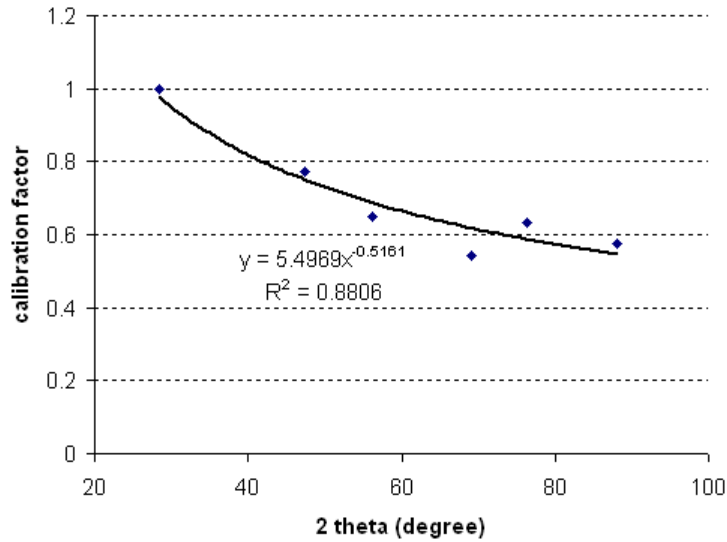


Figure 5.4 The intensity ratio of calculated and measured Si peaks, after normalized at the peak intensity of all peaks with refers to Si (111) peak.

Compared to Equation (5.7), it can be seen that the absorption factor (A_{001} and A_{002}) was added to calculate the integrated intensity of XRD peaks of thin films, due to the limited thickness of thin film. All other terms have the same physical meaning as

above. The absorption in the equation $(A(\theta)) = \exp(-2\mu t / \sin(\theta))$ is related to the film thickness, t . The linear absorption coefficient (μ) for $\text{Fe}_{50}\text{Pt}_{50}$ was calculated to be 3229cm^{-1} . All other terms are constant, and are listed in table 5.3, where the value of temperature factor is from the reference [Barmak et al., (2005)].

Table 5.3 The calculated 001 and 002 XRD peaks of $L1_0 \text{Fe}_{50}\text{Pt}_{50}$ ($S=1$)

Peak	2θ	$ F $	p	L-P	e^{-2M}
001	24.0	81.0	2	39.61	0.95
002	49.0	137.2	2	8.58	0.80

A reference FePt film, with a composition close to stoichiometric $L1_0$ FePt, was annealed at 700°C for 2 hours. Its XRD pattern was shown in Figure 5.5. Based on above approach, the long-range order parameter was calculated to be 0.92 ± 0.05 .

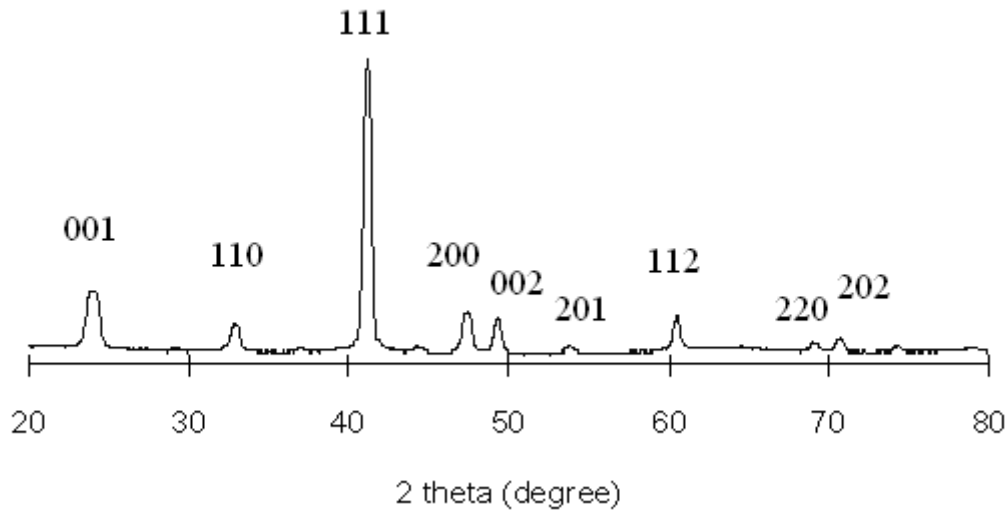


Figure 5.5 The XRD of a reference highly ordered FePt film. The long –range order parameter was characterized to be 0.92 ± 0.05 .

The second approach is a modified version of above technique. In the first approach, the I_{002} was determined through curve fitting. For samples containing a significant amount of disordered *fcc* FePt phase, the determined value of I_{002} will unavoidably be influenced by the 200 peak of *fcc* phase. Since the volume fraction of *fcc* FePt phase can be determined independently in this work, the I_{002} was determined using another approach, given by

$$I_{002} = I_{\{200/002\}L1_0\&fcc} \times f_{L1_0} \times 0.34$$

where the coefficient of “0.34” is the integrated intensity ratio of 002 peak to that of 200 peak for $L1_0$ FePt phase. One assumption is that the sample has no strong texture, especially $\langle 001 \rangle$ fiber texture.

The third approach to derive the S is from the c/a ratio of $L1_0$ phase, given by

$$S^2 = \frac{(c/a)_{\text{experiment}}}{(c/a)_{S=1}}$$

where the c/a ratio for perfectly ordered $L1_0$ phase is taken to be 0.964 [Roberts, (1954)]. For samples studied in our work, the c/a ratio is determined from the 001 and 110 $L1_0$ superlattice reflections. This approach may bring a significant uncertainty since it requires three or four significant digits, and requires a high resolution of the instrument.

5.2.4 Grain size and nucleation/grain density of the $L1_0$ FePt phase

As discussed earlier, the grain size of $L1_0$ FePt based thin films is very important to its applications. For magnetic recording, very small grain size (<10 nm) is desired to increase the recording density. For exchange spring magnets, it is required that the grain size of the soft phase must be small enough to ensure a strong soft-hard magnetic phase coupling. The grains in thin films may not possess a spherical shape. For example, a columnar structure can be achieved in as-deposited and annealed films. Consequently, the grain size in the film thickness direction may be different from that in the film plane. During annealing, the grain dimension in the thickness direction is limited by the film thickness. In the film plane, the grains can continue to grow depending upon the annealing temperature and time. In this work, the grain size of interest is in the film plane rather than that in the film thickness direction.

Scherrer's formula for XRD peak width has been commonly used to determine the grain size of polycrystalline materials; however, it has limited utility to characterize the grain size in the film plane. The main reason is that the planes satisfying the XRD Bragg diffraction conditions with the commonly used theta-2theta scan are parallel to the film plane, and the measured grain size using this approach is in the dimension of the film thickness. One approach to acquire the in-plane grain size is to scan the sample with both the X-ray source and detector at a glancing angle to the sample surface so that the planes nearly perpendicular to the film surface satisfy the Bragg diffraction, and the extracted grain size is the grain size in the film plane. With this approach, a high intensity X-ray source (e.g., from a synchrotron source) is usually preferred. Andrew Warren in our group is using this approach to study the plan view grain size of Cu films

and the correlation of this in plane grain size to the grain size observed by TEM is not linear.

For thin films, it is more convenient to get the grain size information with BF plan view TEM images. FePt films processed at low temperature usually have a mixture of ordered phase and disordered phase, and the ordered $L1_0$ FePt phase has much smaller grains than the disordered fcc phase, as shown in chapter 4. For this reason, the BF TEM images alone are not able to provide information of the structure of $L1_0$ FePt phase.

The HCDF TEM images, as described previously, are very useful to examine the structure of $L1_0$ FePt phase. It can be easily understood that if the $L1_0$ FePt superlattice reflections are selected to form the dark field images, the illuminated grains are the $L1_0$ FePt phase with certain specific orientation.

The nucleation/grain density of $L1_0$ FePt phase can be calculated from the measured $L1_0$ FePt phase fraction and its average grain size. The nucleation density can be the same as, or different from grain density. At the beginning of the phase transformation, prior to significant growth and coalesce of grains, the nucleation density is expected to be the same as the grain density. When a large fraction of $L1_0$ FePt phase has formed, the grain density is smaller than the nucleation density due to the growth of large grains at the expense of small grains. The nucleation/grain density examined here is basically the grain density, but the nucleation density can also be estimated based on the extent of the phase transformation and grain growth. The nucleation/grain density can be classified as an areal density and/or a volume density. The areal nucleation/grain density can be expressed as Equation (5.10).

$$L1_0 \text{ nucleation/grain areal density} = L1_0 \text{ phase fraction} / (\pi r^2) \quad (5.10)$$

For films having an average grain size for the LI_0 FePt phase smaller than the film thickness, a spherical shape of LI_0 phase is assumed, and Equation (5.11) is used for a volume density calculation. Otherwise, a columnar structure of LI_0 phase grains is assumed, and Equation (5.12) is used for the volume density calculation.

$$LI_0 \text{ nucleation/grain density} = LI_0 \text{ phase fraction} / (4\pi r^3/3) \quad (5.11)$$

$$LI_0 \text{ nucleation/grain density} = LI_0 \text{ phase fraction} / (\pi r^2 t) \quad (5.12)$$

where r is the average radius of LI_0 phase grains, and t is the film thickness.

5.3 Experiments

Two sets of $[\text{Fe}/\text{Pt}]_n$ samples were sputtered onto oxidized Si substrates, as listed in table 5.4. The first set of samples (labeled as “ML_TMP_N50”, “ML_TMP_25”, “ML_TMP_150”, “ML_TMP_200”, and “ML_TMP_250”) have the same layer structure, $[\text{Fe}_{2.3\text{nm}}\text{Pt}_{2.9\text{nm}}]_{12}$, but different deposition substrate temperatures, in the range of -50°C to 250°C . Among them, samples “ML_TMP_N50”, “ML_TMP_25”, and “ML_TMP_200” were selected to examine the influence of deposition temperature on the effective interdiffusion coefficient. The second set of samples, labeled as “ML_PDT_11”, “ML_PDT_21”, “ML_PDT_43”, “ML_PDT_86”, and “ML_PDT_172”, have the same common deposition temperature, 250°C , but varying periodicity, in the range of 11\AA to 172\AA . Among them, samples “ML_PDT_21”, “ML_PDT_43”, and “ML_PDT_86” were chosen to determine the influence of the periodicity on the interdiffusivity. The multilayer film samples were annealed in the tube furnace in one atmosphere of flowing Ar + 5% H_2 process gas. To study the effective interdiffusivity, the films were annealed at 275°C , 300°C , and 325°C for different times. To study the structure and magnetic properties, all samples were annealed at 400°C for 30 minutes. The results of a higher temperature (i.e., 500°C) anneal were also obtained, and some of them are shown in this chapter. However, the samples annealed at 400°C are the focus because a minimum processing temperature is desirable for their applications.

Table 5.4 A list the [Fe/Pt]_n multilayer films

Sample ID	Multilayer structure	Period (nm)	Deposition Temperature (°C)	Composition	Thickness (nm)
“ML_TMP_N50”	[Fe _{2.3nm} Pt _{2.9nm}] ₁₂	5.0	-50	Fe _{49.2} Pt _{50.8}	62.0
“ML_TMP_25”	[Fe _{2.3nm} Pt _{2.9nm}] ₁₂	5.0	25	Fe _{49.2} Pt _{50.8}	62.0
“ML_TMP_150”	[Fe _{2.3nm} Pt _{2.9nm}] ₁₂	5.0	150	Fe _{49.2} Pt _{50.8}	62.0
“ML_TMP_200”	[Fe _{2.3nm} Pt _{2.9nm}] ₁₂	5.0	200	Fe _{49.2} Pt _{50.8}	62.0
“ML_TMP_250”	[Fe _{2.3nm} Pt _{2.9nm}] ₁₂	5.0	250	Fe _{49.2} Pt _{50.8}	62.0
“ML_PDT_11”	[Fe _{0.4nm} Pt _{0.6nm}] ₄₈	1.1	250	Fe _{47.1} Pt _{52.9}	51.5
“ML_PDT_21”	[Fe _{0.9nm} Pt _{1.3nm}] ₂₄	2.1	250	Fe _{47.1} Pt _{52.9}	51.5
“ML_PDT_43”	[Fe _{1.8nm} Pt _{2.5nm}] ₁₂	4.3	250	Fe _{47.1} Pt _{52.9}	51.5
“ML_PDT_86”	[Fe _{3.5nm} Pt _{5.0nm}] ₆	8.6	250	Fe _{47.1} Pt _{52.9}	51.5
“ML_PDT_172”	[Fe _{7.1nm} Pt _{10.1nm}] ₃	17.2	250	Fe _{47.1} Pt _{52.9}	51.5

5.4 Results

5.4.1 Multilayer structure

The layer structure of the films deposited at 250°C (samples “ML_PDT_11”~”ML_PDT_172”) was examined with the XRR, and the spectra are shown in Figure 5.6, wherein the period (Λ) is defined as sum of the thickness of one Fe and one Pt layer. The presence of strong Bragg reflections confirms the compositional layering in the unannealed samples. The first peak of sample “ML_PDT_11” is at a higher angle ($2\theta= 8.4^\circ$), and is shown in an inset in the upper right corner of the figure.

By comparing the XRR peak locations, we can see that the positions and number of peaks correspond well to the designed layer structures. These spectra indicate that the Fe-Pt interdiffusion during deposition at 250°C is still weak, which does not destroy the multilayer structures with a small periodicity. Following the ex-situ annealing of these samples, it was found that the homogenization can occur easily at temperature 350°C or above, judged by the decrease (loss) of the Bragg reflection peak intensity after annealing. For all the annealed samples, the multilayer structure disappears after annealing at higher temperature and the XRR spectra lack any Bragg reflections, indicating that compositional homogeneity has been achieved. An example of this is also shown in the figure, where the small, closely spaced peaks are understood as the interaction of reflected waves from film/ambient and film/substrate interfaces, which can be used to determine the total film thickness.

The XRR spectra of samples “ML_TMP_N50”, “ML_TMP_25”, “ML_TMP_150”, “ML_TMP_200”, “ML_TMP_250” were also acquired, but not shown here. These samples have the same periodicity, and similar XRR spectra are obtained.

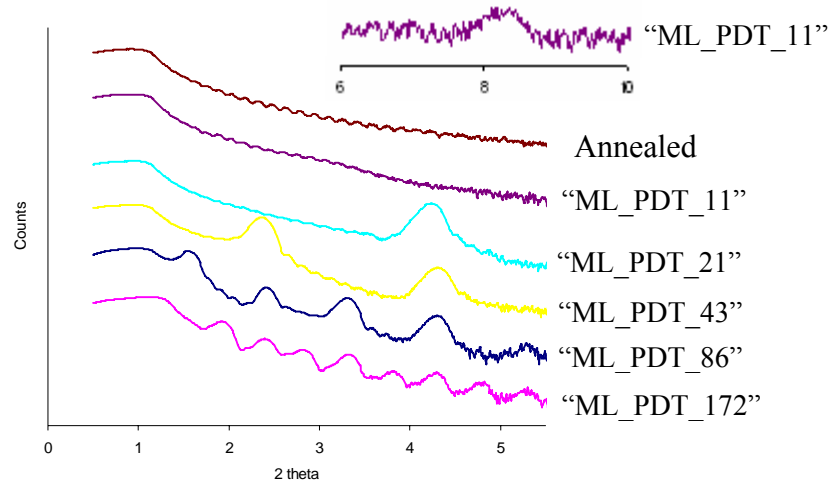


Figure 5.6 XRR of the as-deposited and annealed samples “ML_PDT_11” , “ML_PDT_21”, “ML_PDT_43”, “ML_PDT_86”, and “ML_PDT_172” deposited at 250°C with different periodicity.

5.4.2 Effective interdiffusivity

In this section, the influence of deposition temperature and periodicity of multilayer films on the interdiffusivity will be demonstrated. As mentioned above, the effective interdiffusivity (D_{Λ}) in nano-scale multilayer films can deviate significantly from the bulk interdiffusivity due to the presence of the steep compositional gradient, small grain size, and coherent strains in multilayers. It may not be useful to use the measured bulk diffusivity to understand the interdiffusion of multilayers. Instead, Equation (5.1), based on the decay rate of the intensity of the first small angle X-ray diffraction peak due to thermal treatments, is used to determine the effective interdiffusivity in multilayer films.

Figure 5.7 shows the evolution of the small angle X-ray diffraction pattern for sample “ML_PDT_86” (a representative example) annealed for different times at 325°C. The intensity of the satellite peak decreases with annealing time due to the interdiffusion of Fe and Pt. Figure 5.8 shows plots of $\ln[I(t)/I(0)]$ versus t for samples “ML_PDT_21”, “ML_PDT_43”, and “ML_PDT_86” annealed for different times at 325°C. It can be seen that $\ln[I(t)/I(0)]$ falls almost linearly with the annealing time after the first anneal. The fitted lines do not meet the Y axis at 0, due to an initial drop in intensity, which has been widely observed and investigated in many systems [[Zotov et al., \(2006\)](#)]. As a common practice, the linear decay after the initial rapid drop is taken to determine the effective interdiffusivity for each sample at the annealing temperature studied.

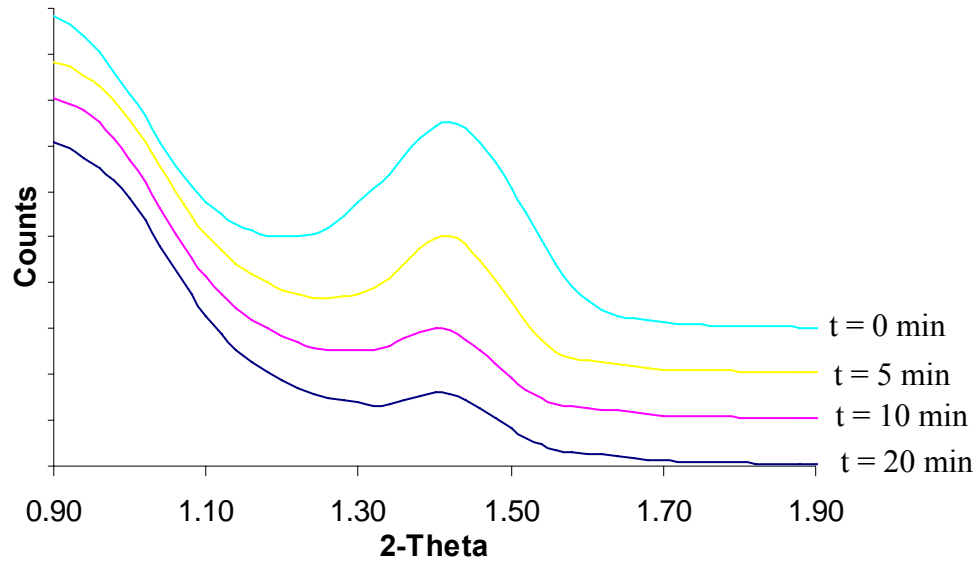


Figure 5.7 The decay of the first satellite peak due to annealing for sample “ML_PDT_86” annealed at 325°C.

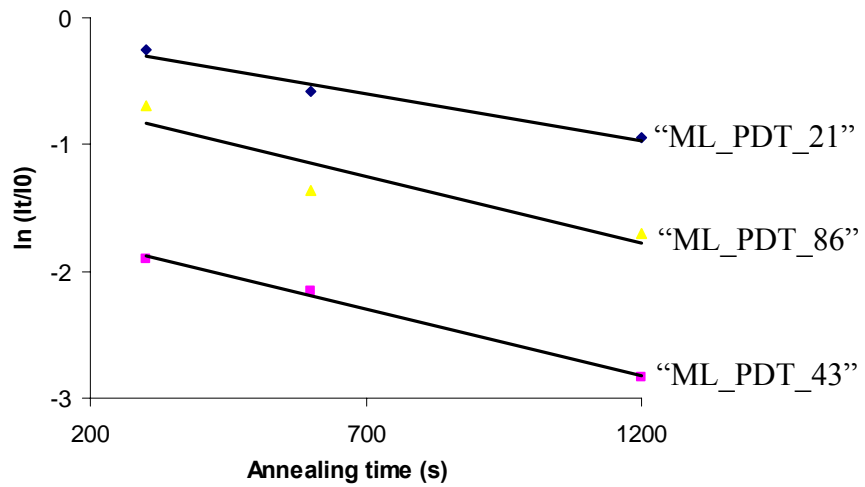


Figure 5.8 The $\ln(I(t)/I(0))$ versus annealing time for samples “ML_PDT_21”, “ML_PDT_43”, and “ML_PDT_86”.

Sample “ML_TMP_N50”, “ML_TMP_25”, “ML_TMP_200” were selected to study the influence of the deposition temperature, and sample “ML_PDT_21”, “ML_PDT_43”, “ML_PDT_86” were chosen to investigate the influence of periodicity on the Fe-Pt interdiffusivity. All six samples were annealed for different times at 275°C, 300°C, and 325°C. The measured effective interdiffusivities, according to Equation (5.1), are shown in Figure 5.9 in the form of $\ln(D_{eff})$ plotted as a function of $1/T$. It can be seen from Figure 5.9(b) that the effective interdiffusivity increases with the increase of periodicity for samples “ML_PDT_21”, “ML_PDT_43”, and “ML_PDT_86”, with approximately similar interdiffusion activation energies (ranging from 1.3 to 1.8eV). This trend is consistent with the greater effective interdiffusivity reported for larger periodicity $[\text{Fe/Pt}]_n$ multilayers by Zotov et al. [Zotov et al. (2006)]. In the other set of samples deposited at different temperatures, as shown in Figure 5.9 (a), sample “ML_TMP_N50” (deposited at -50°C) has a lower interdiffusivity and activation energy, while the effective interdiffusivity of samples “ML_TMP_25” and “ML_TMP_200” are similar in magnitude and temperature dependence (activation energy). The measured diffusivity, extracted D_{eff} and Q in Arrhenius form, are also shown in table 5.5.

The measured diffusivity and activation energy for diffusion in $[\text{Fe/Pt}]_n$ multilayers are much smaller than that of bulk systems [Kaiser et al., (2008)]. For example, the activation energy for bulk diffusivity ranges from 2.5 eV to 3.0 eV, and the characteristic diffusion distance at 350°C for 1 hour is estimated to be in the range of 0.001 nm to 0.02 nm. For $[\text{Fe/Pt}]_n$ multilayer films, the measured activation energy ranges from 1.5 eV to 2.0 eV, and complete composition homogenization under the same annealing condition is achieved over distances from 1 nm to 22 nm. The

disparity of these values suggests that the formation of *fcc* FePt is through the nucleation of alloyed grains and the growth of these grains via grain boundary diffusion. In this manner the composition of the initial *fcc* Pt grains is changed by the motion of an interface across the grains, rather than by lattice diffusion from the grain boundary into the interior volume of the grain.

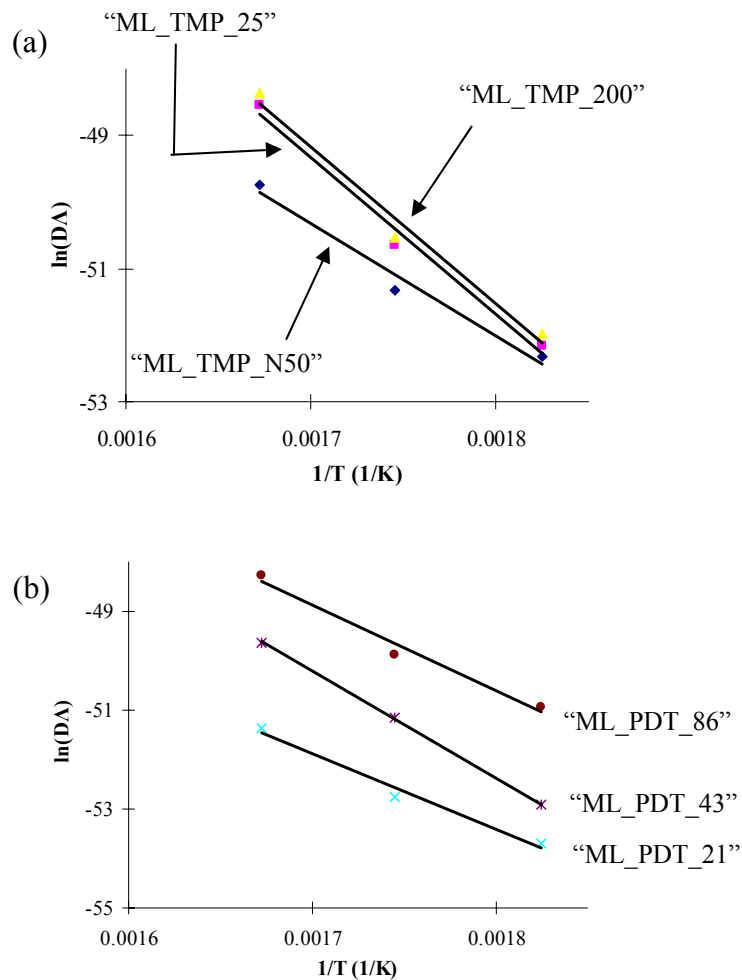


Figure 5.9 (a) The $\ln(D_A)$ versus $(1/T)$ for samples "ML_TMP_N50", "ML_TMP_25", and "ML_TMP_200". (b) The $\ln(D_A)$ versus $(1/T)$ for samples "ML_PDT_21", "ML_PDT_43", and "ML_PDT_86". D_A has the unit of m^2/s .

Table 5.5 The diffusivities measured and the Arrhenius expressions

Sample	Annealing Temp. (°C)	$d\ln[I(t)/I(0)]/dt$ (1/s)	D_{Λ} (m ² /s)	Arrhenius expressions (m ² /s)
“ML_TMP_N50”	275	5.98×10^{-5}	1.893×10^{-23}	$3.84 \times 10^{-10} \exp(-1.5 \text{ eV/kT})$
	300	1.63×10^{-4}	5.161×10^{-23}	
	325	7.90×10^{-4}	2.501×10^{-22}	
“ML_TMP_25”	275	7.00×10^{-5}	2.216×10^{-23}	$1.13 \times 10^{-4} \exp(-2.0 \text{ eV/kT})$
	300	3.17×10^{-4}	1.004×10^{-22}	
	325	2.62×10^{-3}	8.296×10^{-22}	
“ML_TMP_200”	275	8.43×10^{-5}	2.669×10^{-23}	$1.06 \times 10^{-4} \exp(-2.0 \text{ eV/kT})$
	300	3.60×10^{-4}	1.140×10^{-22}	
	325	3.10×10^{-3}	9.815×10^{-22}	
“ML_PDT_21”	275	7.26×10^{-5}	4.780×10^{-24}	$5.06 \times 10^{-12} \exp(-1.5 \text{ eV/kT})$
	300	1.88×10^{-4}	1.238×10^{-23}	
	325	7.46×10^{-4}	4.912×10^{-23}	
“ML_PDT_43”	275	3.95×10^{-5}	1.040×10^{-23}	$1.18 \times 10^{-6} \exp(-1.9 \text{ eV/kT})$
	300	2.33×10^{-4}	6.136×10^{-23}	
	325	1.05×10^{-3}	2.765×10^{-22}	
“ML_PDT_86”	275	7.20×10^{-5}	7.601×10^{-23}	$4.49 \times 10^{-9} \exp(-1.3 \text{ eV/kT})$
	300	2.06×10^{-4}	2.175×10^{-22}	
	325	1.04×10^{-3}	1.098×10^{-21}	

5.4.3 Microstructure of annealed [Fe/Pt]_n multilayer films

The as-deposited films were found to consist of *fcc* phase Fe and Pt (except samples “ML_PDT_86” and “ML_PDT_172” which have a *bcc* phase Fe present) while the annealed films showed evidence of both *fcc* and *L1₀* phases, but lacked evidence of the Fe₃Pt and FePt₃ *L1₂* phases that have been reported by others in much larger periodicity [Fe/Pt]_n multilayers [Verdier et al., (2005)]. We hypothesize that the absence of the *L1₂* phases is due to a lack of driving force for their nucleation in our small periodicity samples.

No *L1₀* phase was observed until an annealing temperature at or above 300°C was utilized, similar to previous reports [Verdier et al., (2005); Endo et al., (2001); Endo et al., (1003); Chou et al., (2004) I, II; Luo et al., (1995); Reddy et al., (2006)]. Figure 5.10 shows the evolution of *L1₀* structure of sample “ML_PDT_172” (a representative example) annealed at 300°C to 700°C for 30 minutes. It is obvious that the grain size of the *L1₀* phase is very sensitive to annealing temperature. Also evident in Figure 5.10 and throughout this work is the common occurrence for the smaller *L1₀* phase grains located on boundaries between larger grains. This result is consistent with the role of grain boundaries as favorable nucleation sites for the ordered phase. Figure 5.11 (a) shows the location of *L1₀* phase grains on a network of visible grain boundaries traced from the HCDF image (Figure 5.11 c) and the bright field image at the same view (Figure 5.11 b). Although the traced network is not completed, and only identifies part of the grain boundary network, it clearly shows the heterogeneous nucleation of most *L1₀* grains on the grain boundaries.

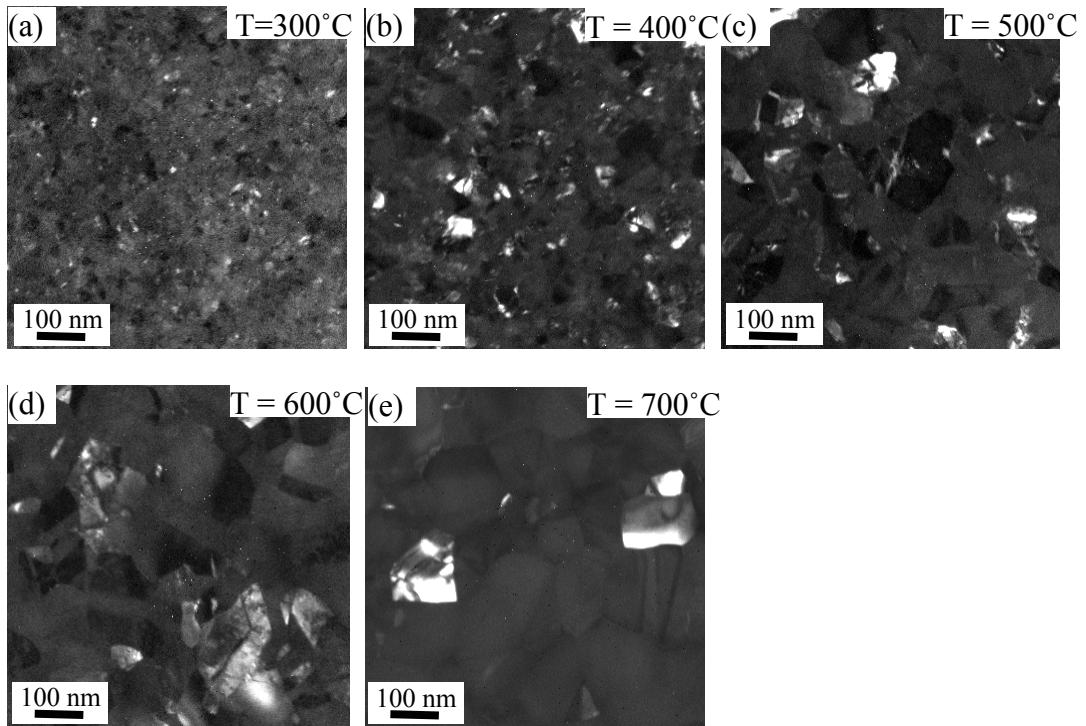


Figure 5.10 Plan view HCDF TEM images of the sample “ML_PDT_172”, $[\text{Fe}_{71}\text{ÅPt}_{101}\text{Å}]_3$, annealed at different temperatures.

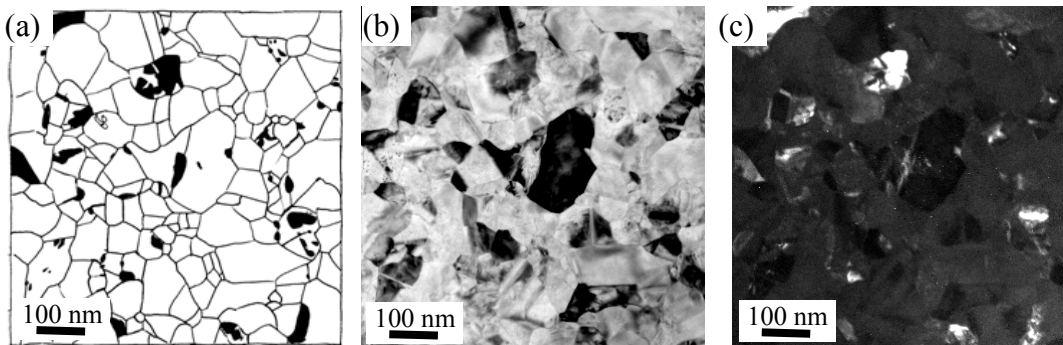


Figure 5.11 (a) shows the location of $L1_0$ phase grains on a network of visible grain boundaries traced from the enlarged HCDF image (Figure 5.11 c) and the bright filed image at the same view (Figure 5.11 b) for sample “ML_PDT_172” annealed at 500°C for 30 minutes.

The influence of substrate temperature on the $L1_0$ phase grain size (sample “ML_TMP_N50”, “ML_TMP_25”, “ML_TMP_150”, “ML_TMP_200”, and “ML_TMP_250”) is demonstrated in Figure 5.12 and Figure 5.13. All samples were annealed at 400°C for 30 minutes. It can be seen that the samples deposited at low temperature (Figure 5.12 a) and high temperature (Figure 5.12e) have a very small grain size for the $L1_0$ phase. Samples “ML_TMP_150” and “ML_TMP_200” have a similar, larger grain size, and sample “ML_TMP_25” has intermediate size grains. The results will be discussed later.

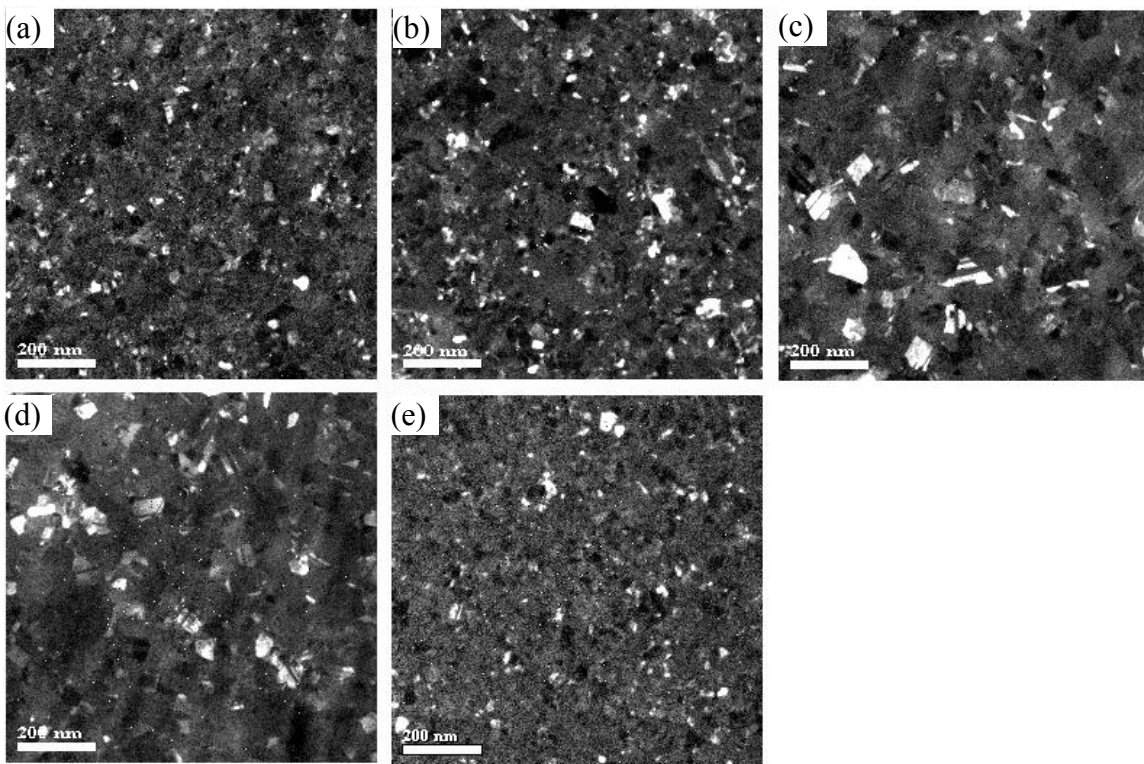


Figure 5.12 (a) to (e) The plan view HCDF TEM images from $L1_0$ 001 and 110 superlattice reflections of samples “ML_TMP_N50”, “ML_TMP_25”, “ML_TMP_150”, “ML_TMP_200”, and “ML_TMP_250” annealed at 400°C for 30minutes, respectively.

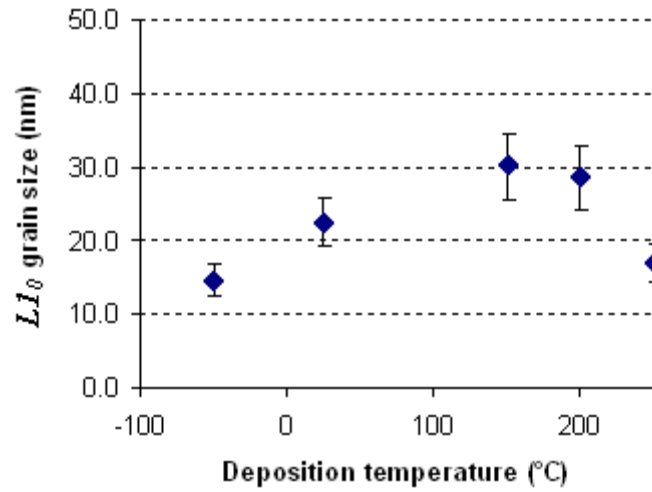


Figure 5.13 The measured grain size of $L1_0$ FePt phase versus the deposition temperature for samples “ML_TMP_N50” ~ “ML_TMP_250” annealed at 400 °C for 30 minutes.

Samples “ML_PDT_11”, “ML_PDT_21”, “ML_PDT_43”, “ML_PDT_86”, and “ML_PDT_172” were annealed at 400°C for 30 minutes to study the influence of periodicity. Figure 5.14 shows the HCDF TEM images obtained from the 001 and 110 $L1_0$ FePt superlattice reflections, and Figure 5.15 shows the measured grain size versus periodicity. The size of the $L1_0$ FePt phase grains is observed to increase with the increase of bilayer period.

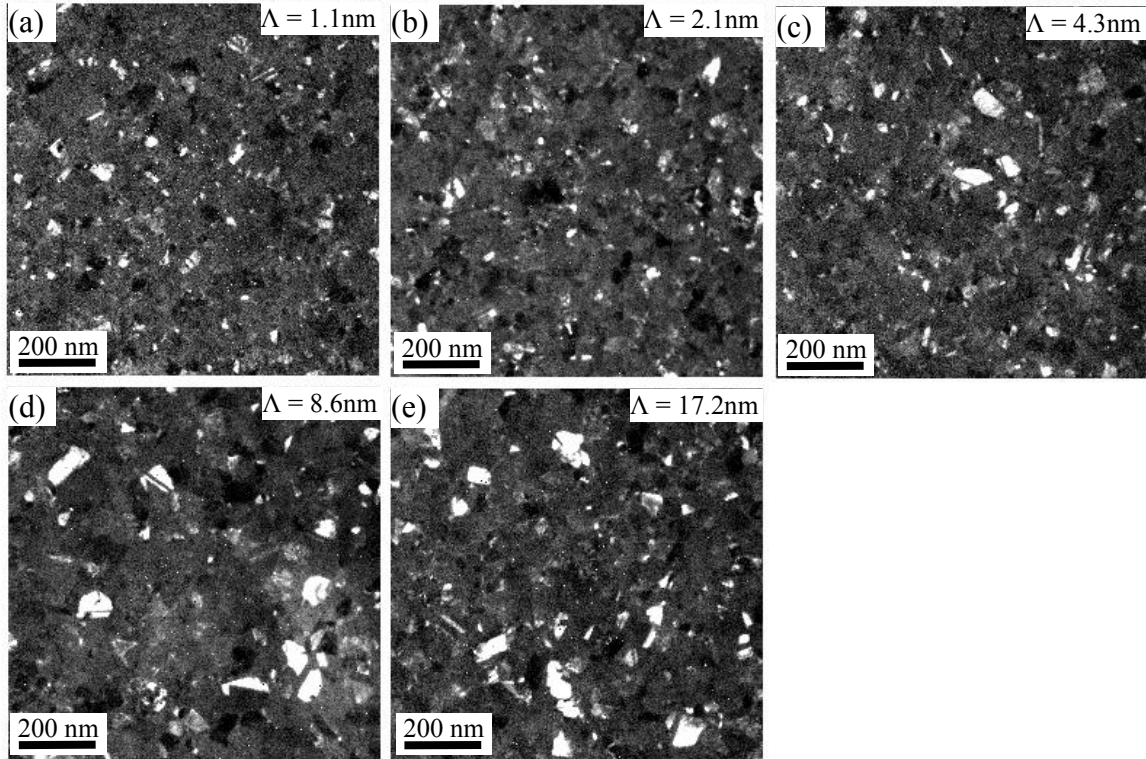


Figure 5.14 (a) to (e) plan view HCDF TEM images of samples “ML_PDT_11” to “ML_PDT_172” annealed at 400°C for 30minutes from 001 and 110 superlattice diffraction rings.

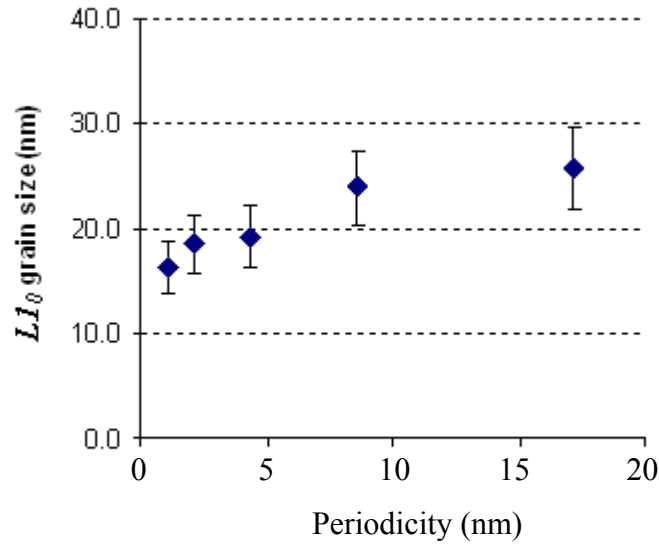


Figure 5.15 The measured grain size of LI_0 FePt phase versus the periodicity for samples “ML_PDT_11” ~ “ML_PDT_172” annealed at 400°C for 30minutes.

The LI_0 phase grains shown in the above HCDF images (Figure 5.10 to Figure 5.12, Figure 5.14) demonstrate a very interesting size distribution. In each figure, there are a few large grains, but most of the grains are much smaller and located at the grain boundaries. A large number of the small LI_0 FePt grains were also observed for samples annealed at high temperature, where the fraction of LI_0 FePt phase is close to 1. The LI_0 FePt phase growth is generally interface controlled, i.e., the jumping of atoms from the *fcc* phase to the LI_0 phase at their interface. The atomic mobility and energy barrier for this atomic jumping at the interface is believed to be related to the misorientation, similar to other material systems [Aaronson et al., (1977); Shewmon, (1969)]. The larger LI_0 grains are assumed to have resulted from having a rapidly moving inter-phase boundary

(higher mobility and lower energy barrier). The small grains, however, most probably have the growth inhibited interfaces.

Texture is another concern for annealed films. The formation of texture in thin films can be understood as the crystallographic planes orientated relative to the film plane to decrease the surface energy or strain energy of the film. The most commonly observed texture plane in thin films of *fcc* phase is (111) because of fewer dangling bonds between adjacent (111) planes and therefore lower surface energy. In thicker films where the strain energy becomes dominant, the (100) texture is also common. Because the $\langle hkl \rangle$ direction in cubic systems is normal to the (hkl) plane, the above textures are usually noted as $\langle 111 \rangle$ or $\langle 100 \rangle$ fiber textures. The $L1_0$ FePt is a slightly distorted structure of the *fcc* cubic; consequently, it will be treated as cubic here.

A standard approach to quantify thin film texture is through XRD pole figures. For films deposited on amorphous substrates, the texture formed is mostly a fiber texture. In other words, there is no preferred crystallographic direction in the film plane, as would be the case for a sheet texture. For fiber textures, a simple XRD rocking scan can be used to quantify the texture, wherein the detector is fixed at the appropriate 2θ value for the (hkl) plane of interest, and the sample orientation scanned in a small range around θ .

In this work, the texture is examined using TEM, for convenience. The texture of a film can be determined by the evolution of the electron diffraction pattern as the sample tilt angle is varied. The principle of this technique is briefly described below. Details of the theory and examples can be found in the references [[Tang and Laughlin, \(1996\) I; II](#)]. For a strong 111 textured film, as one example, the 111 ring in the electron diffraction pattern should be very weak but 110 should be very strong. The reason is that

the 111 crystallographic planes are parallel to the film plane, in which case they do not satisfy the Bragg diffraction condition for the electron beam perpendicular to the film plane. The 110 planes, normal to the 111 texture planes, can be found parallel to the electron beam, and satisfy the Bragg diffraction. However, if the film is tilted 19.5 degree along one direction (i.e., α tilt), two strong arcs of the 111 ring in the diffraction pattern will become visible. The reason is that the angle between some $\{111\}$ planes, for example, (111) and ($\bar{1}11$) plane, is 70.5. When the sample is tilted 19.5 degree, certain orientations of $\{111\}$ planes (parallel to the tilt axis) are now parallel to the electron beam, and therefore able to satisfy the Bragg diffraction condition. In the diffraction pattern, this appears as two strong arcs. In the diffraction pattern of polycrystalline films, the (111), ($\bar{1}11$), and other $\{111\}$ planes share the same diffraction ring. The quantity of $\{111\}$ planes satisfying the diffraction will influence the intensity of the ring. Figure 5.16 shows the diffraction pattern of a slightly $\langle 111 \rangle$ -fiber textured Cu film, which can be understood from above analysis. The image was shown in a reversed grey level because it is easier to judge the contrast.

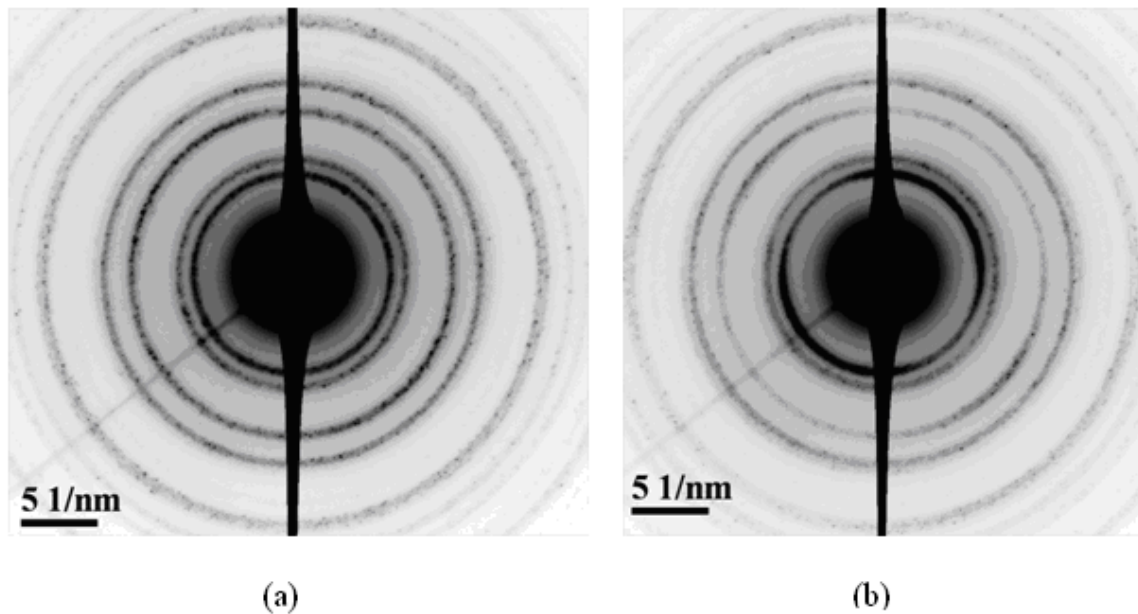


Figure 5.16 The TEM diffraction pattern of a slightly textured Cu film examined (a) 0 tilted, and (b) 19.5 degree tilted condition. The diffractions rings were indexed as 111, 200, 220, 311, 222 starting from the center.

The textures of $[\text{Fe/Pt}]_n$ films annealed at 400°C and 500°C for 30minutes were examined, and no strong textures were observed. Figure 5.17 is the diffraction pattern acquired at 0 degree and tilted 19.5 degrees of sample “ML_PDT_172” annealed at 500°C for 30 minutes, as a typical example. As can be seen from the figure, there is a very weak arc present in the tilted diffraction pattern, which indicates that there is no strong $\langle 111 \rangle$ fiber texture for the samples examined. The possibility of a $\langle 100 \rangle$ fiber texture was also examined and not observed.

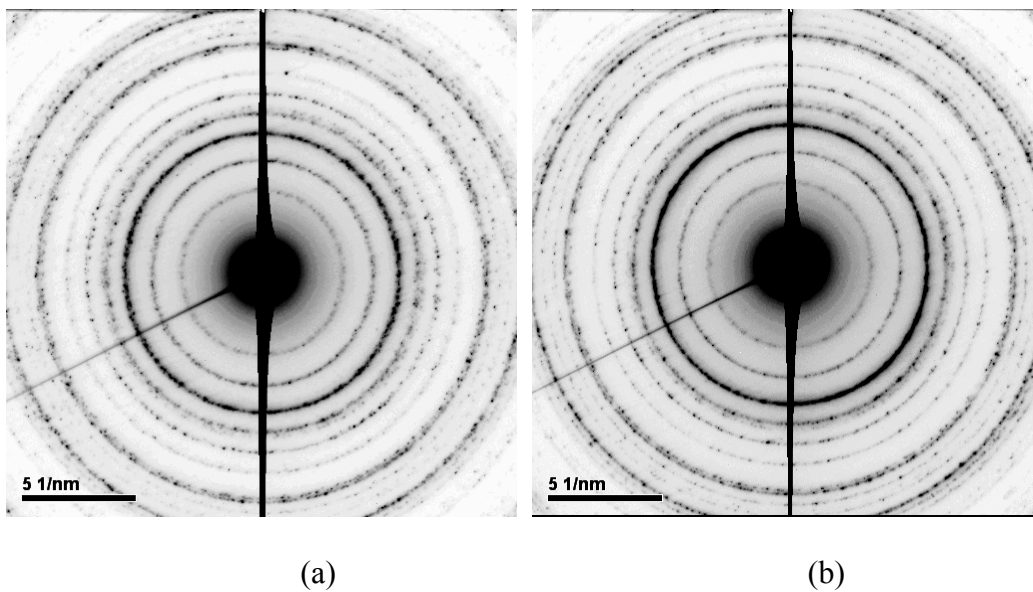


Figure 5.17 The TEM diffraction pattern of a sample “ML_PDT_172”, annealed at 500°C for 30 minutes and examined at (a) 0 tilted, and (b) 19.5 degree tilted condition.

5.4.4 Long-range order parameter

The long-range order parameter of the $L1_0$ FePt phase, S , was quantitatively determined using the methods described above using XRD. Figures 5.18 and 5.19 show the XRD patterns of two sets of samples with varying substrate temperature and periodicity, respectively. All samples were annealed at 400 °C for 30 minutes. The unlabeled extra peaks as shown at 30°, 36°, and 45° are understood as from the substrate or mounting clay, as similar reflections corresponding to these extra peaks are not observed in the SADP patterns. Three methods will be applied to determine S . In this first approach, the integrated intensity of 001 and 002 peaks were extracted with the software “Jade” (provided by Materials Data Inc.) by curve fitting. For the samples with a lower ordering, the 002 peak overlaps other peaks, including $\{200\}_{\text{fcc}}$, and $\{200\}_{L1_0}$, which results in a relatively large uncertainty. In this second approach, the integrated intensity of $\{200\}_{\text{fcc}\&L1_0}$ was measured which gives the I_{002} indirectly by considering the volume fraction of $L1_0$ phase and ratio of I_{002}/I_{200} for $L1_0$ phase. In third approach, the measured c/a ratio of the $L1_0$ FePt phase is used to estimate the extent of ordering. Figure 5.20 (a) and (b) shows the measured c/a ratio versus the deposition temperature and the periodicity, respectively, for two sets of samples. The value of c/a was determined from the superlattice reflections (001, 110 et al.) of the $L1_0$ FePt phase in the XRD patterns. The measured value of S , using three different techniques, was shown in Figure 5.21 (a), and (b) for two sets of sample, respectively.

Figure 5.21 shows the same trend of the ordering versus the deposition temperature and periodicity. For the set of samples deposited at different substrate temperatures, it can be noted that the cold deposited sample has a lower ordering, and the

more highly ordered samples are those deposited at 150°C and 200°C. The other set of samples with varying periodicity, the ordering generally increases with the increase of the periodicity.

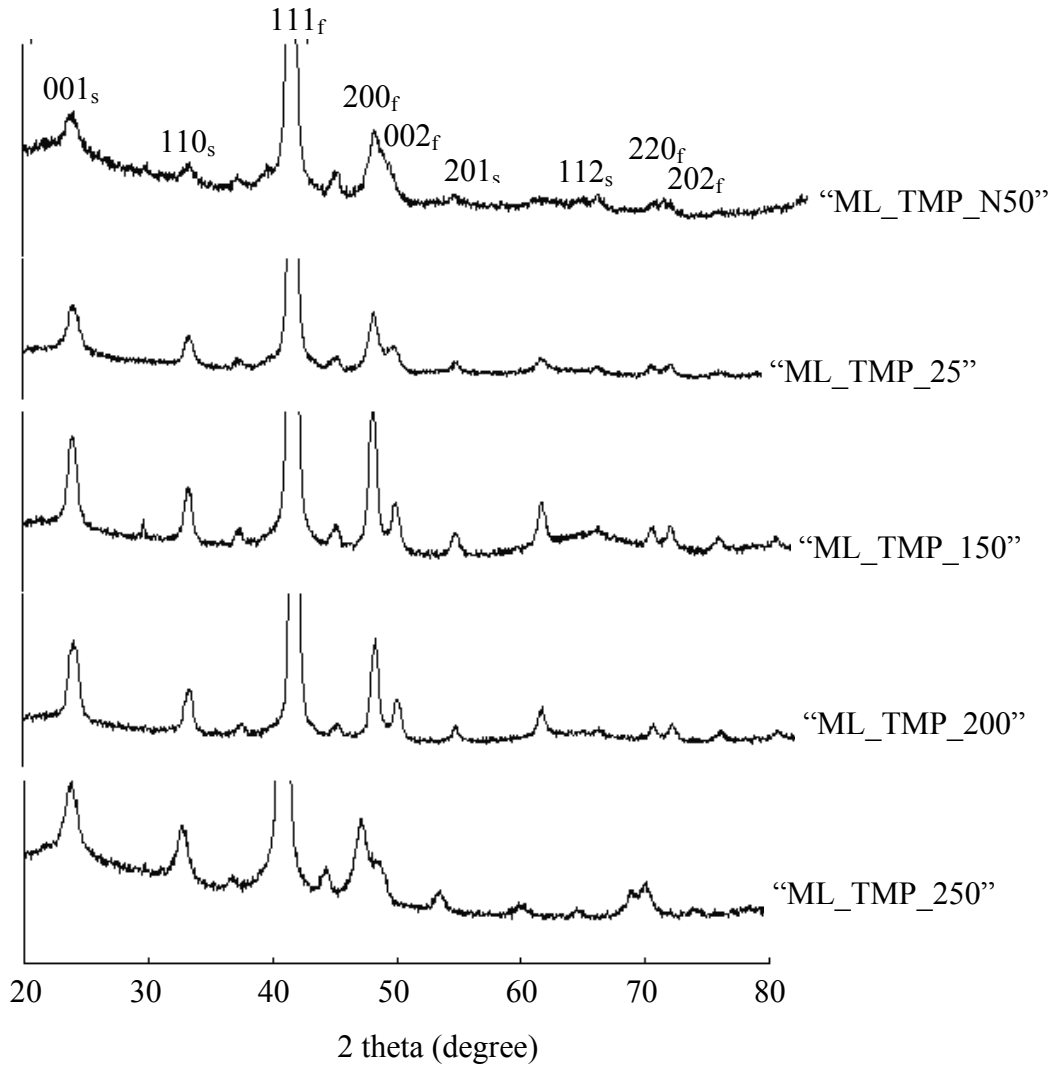


Figure 5.18 shows the XRD of sample “ML_TMP_N50”, “ML_TMP_25”, “ML_TMP_150”, “ML_TMP_200”, and “ML_TMP_250” annealed at 400 °C for 30 minutes, from the top to bottom sequentially.

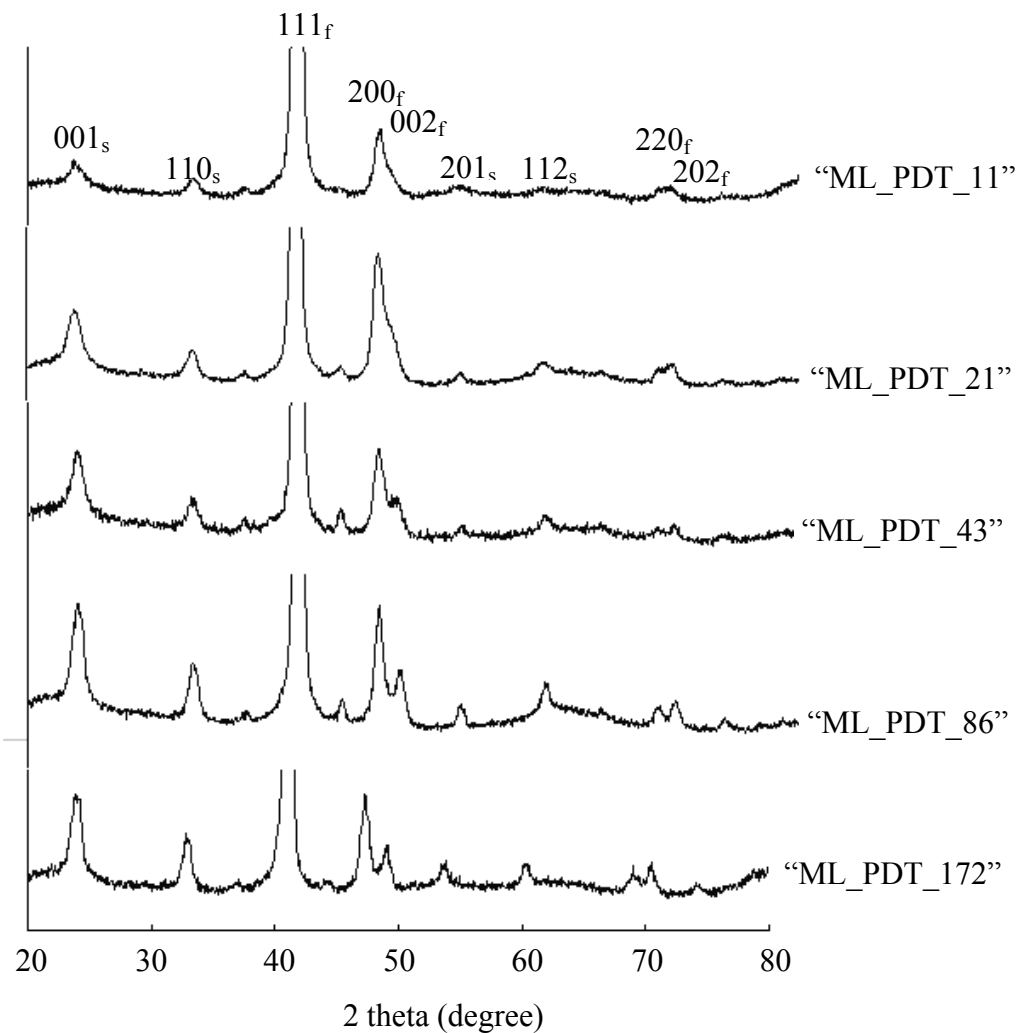


Figure 5.19 shows the XRD of sample “ML_PDT_11”, “ML_PDT_21”, “ML_PDT_43”, “ML_PDT_86”, and “ML_PDT_172” annealed at 400 °C for 30 minutes, from the top to bottom sequentially.

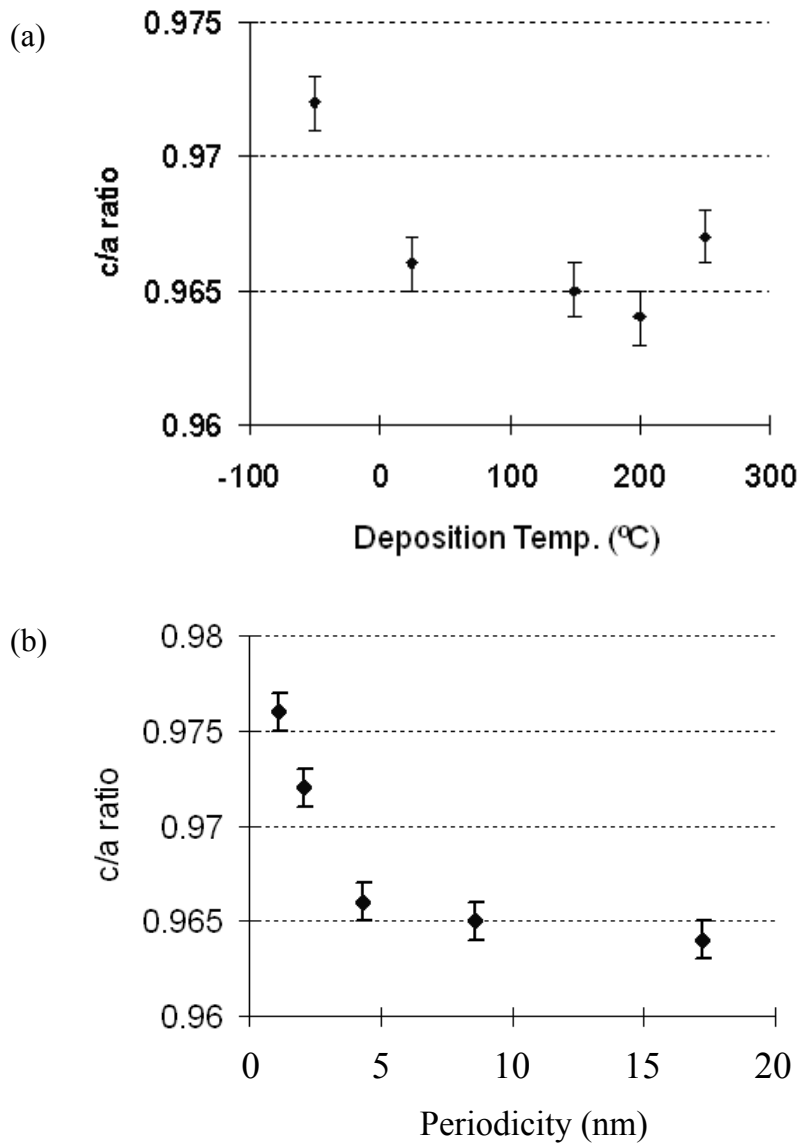


Figure 5.20 (a) the c/a ratio versus deposition temperature for samples “ML_TMP_N50”, “ML_TMP_25”, “ML_TMP_150”, “ML_TMP_200”, and “ML_TMP_250” annealed at 500°C for 30 minutes. (b) the c/a ratio versus periodicity for samples “ML_PDT_11”, “ML_PDT_21”, “ML_PDT_43”, “ML_PDT_86”, and “ML_PDT_172” annealed at 400°C for 30 minutes. The c/a ratio was determined from the superlattice reflections of $L1_0$ FePt phase in the XRD patterns.

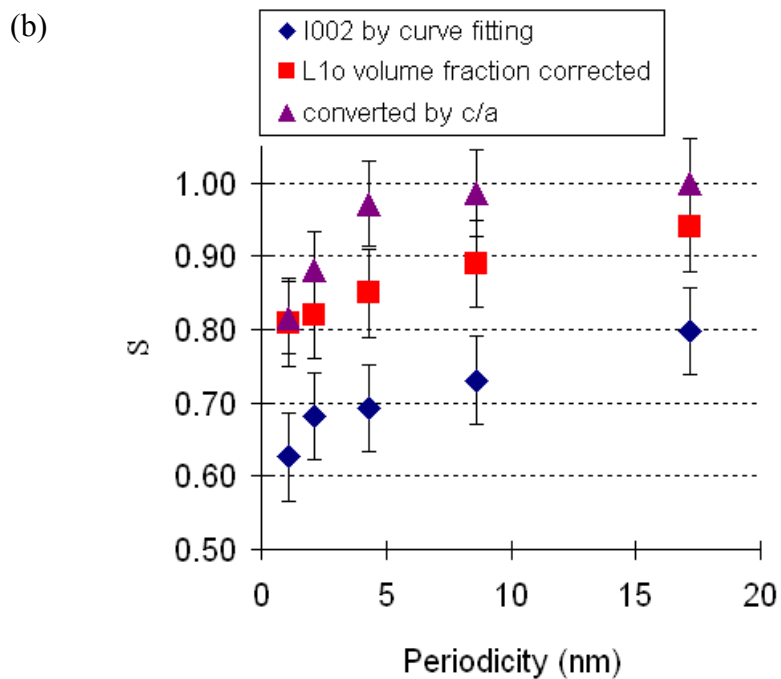
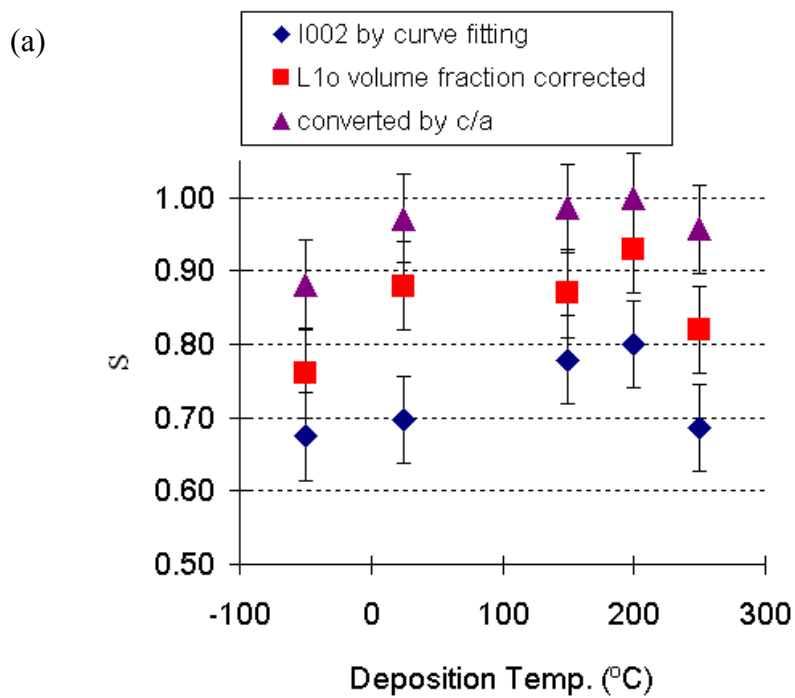


Figure 5.21 The measured value of S versus (a) the deposition temperature and (b) the periodicity of two sets of samples annealed at 400°C for 30 minutes.

5.4.5 Volume fraction and nucleation/grain density of $L1_0$ FePt phase

The volume fraction of $L1_0$ FePt phase, determined using the technique described above, is shown in Figure 5.22 (a) and (b), respectively. Both sets of samples were annealed at 400°C for 30 minutes.

The influence of deposition temperature on the $L1_0$ FePt volume fraction is demonstrated in Figure 5.22 (a). The samples deposited at low temperature (-50°C) and high temperature (250°C) do not show promising results. The samples giving the maximum $L1_0$ volume fractions are those deposited at 150°C and 200°C. The room temperature deposited sample has a medium value.

Figure 5.22(b) shows the influence of layer periodicity on the $L1_0$ phase volume fraction. For samples with periodicity smaller than 10 nm, the $L1_0$ phase volume fraction drops quickly with the decrease of periodicity. The volume fraction tends to be stabilized for samples with periodicity higher than 10 nm.

Figure 5.23 (a) and (b) show the measured $L1_0$ FePt phase nucleation/grain density for two sets of samples. They generally have the reverse trend of the volume fraction and grain size of the $L1_0$ phase. A possible reason is grain coalescence during the grain growth which decreases the measured density. However, it should be pointed out that in figure 5.23 (b), the increase in grain density as the bilayer period is reduced by a factor of fifteen (from 17.2 nm to 1.1 nm) is only a factor of two (from $\sim 1 \times 10^{17}/\text{cm}^3$ to $\sim 2 \times 10^{17}/\text{cm}^3$). The real difference in nucleation density as a function of bilayer period may be even less than the factor of two, as the thicker films have a higher volume fraction transformed (see Figure 5.22 (b)) and hence may suffer a greater extent of grain coalesce.

The measured LI_0 FePt grain/nucleation density is well consistent with published data. For example, Berry and Barmak calculated a nucleation density of $3.76 \times 10^{17} \text{ cm}^{-3}$ for sample $\text{Fe}_{47.5}\text{Pt}_{52.5}$ [Berry and Barmak, (2007)]. Ding and Majetich reported a value of $1 \times 10^{17} \text{ cm}^{-3}$ and $4 \times 10^{17} \text{ cm}^{-3}$ for 13 nm and 8 nm nanoparticles, by measuring the magnetic switching field distribution from remanent hysteresis loops [Ding and Majetich, (2006)]. As the annealed [Fe/Pt] $_n$ multilayer films have a high LI_0 phase volume fraction, the comparison of our measured LI_0 phase nucleation density with published data indicates that the LI_0 grain growth in our samples may not significantly decrease the grain/nucleation density. Therefore, the measured LI_0 phase nucleation/grain density may be used to approximately represent the LI_0 phase nucleation density

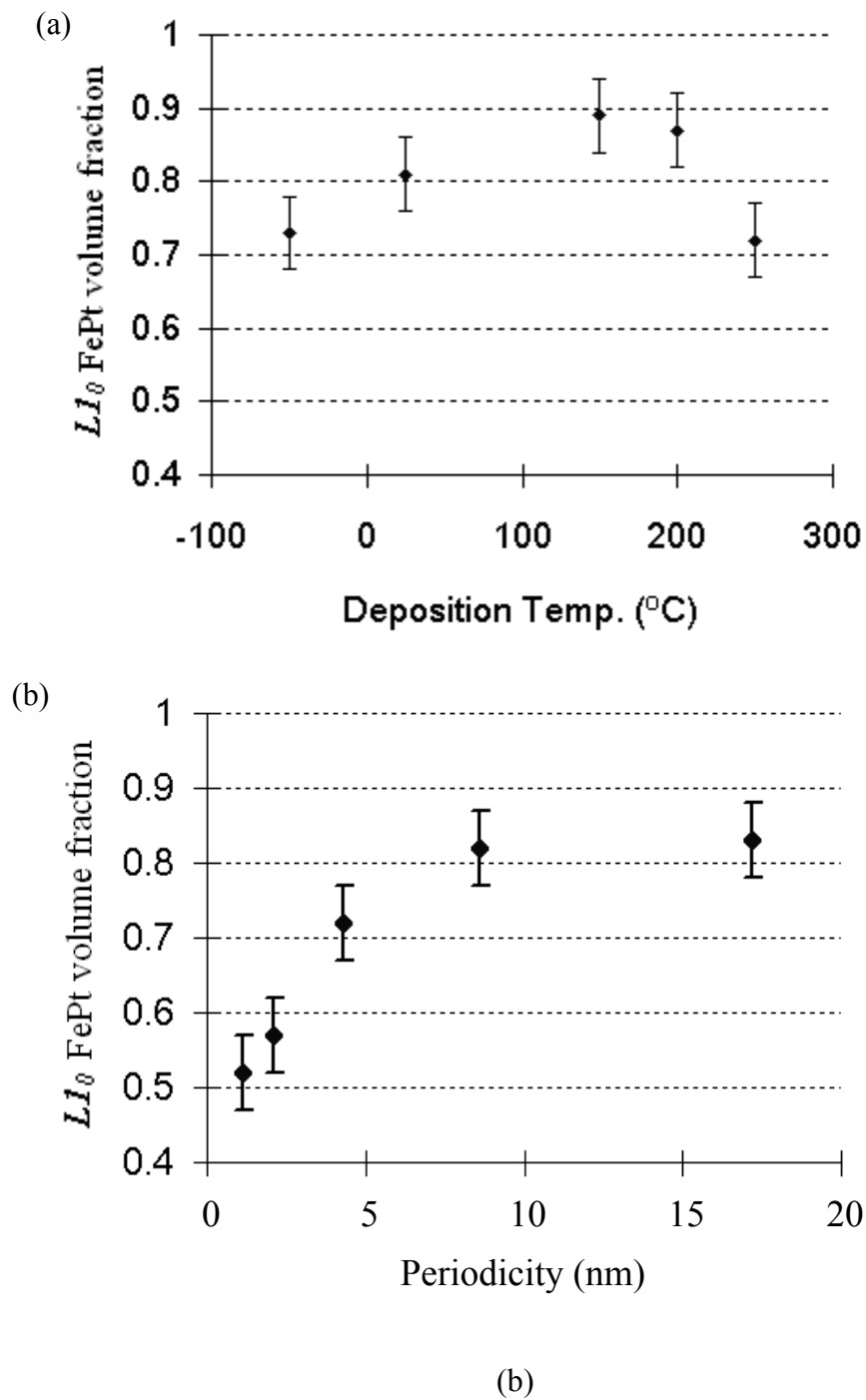
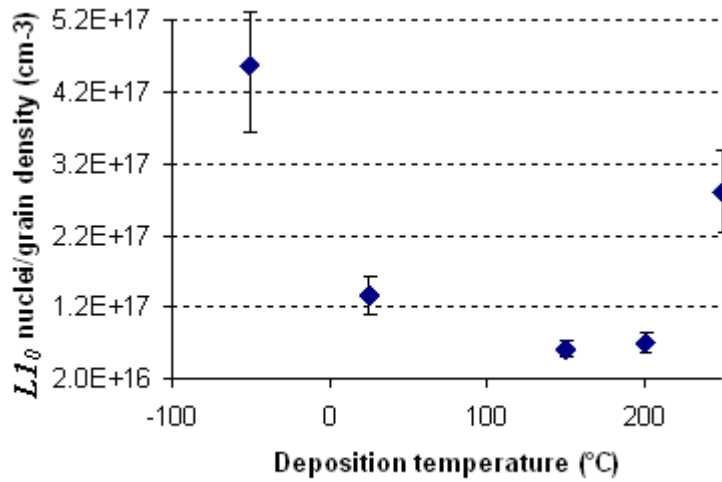
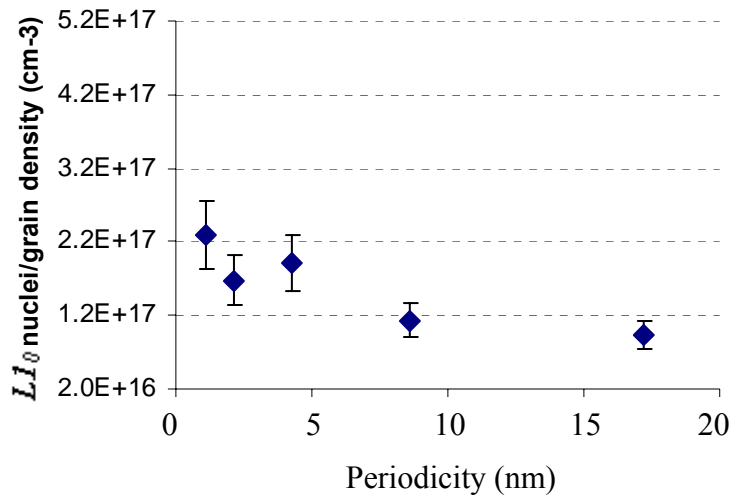


Figure 5.22 The measured volume fraction of LI_0 FePt phase versus (a) the deposition temperature and (b) the periodicity of two sets of samples annealed at 400°C for 30 minutes.



(a)

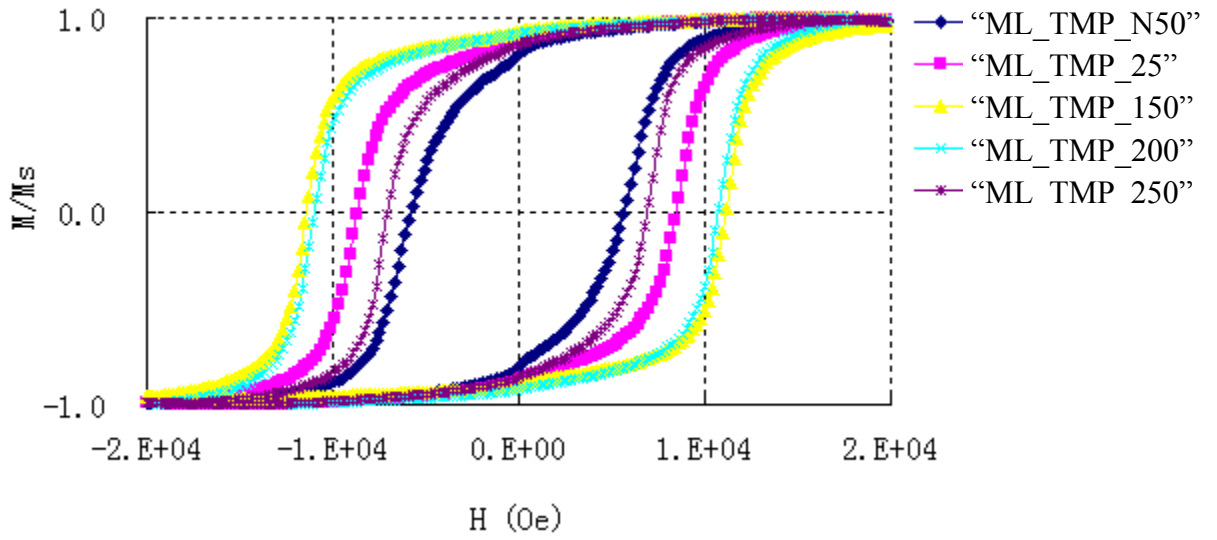


(b)

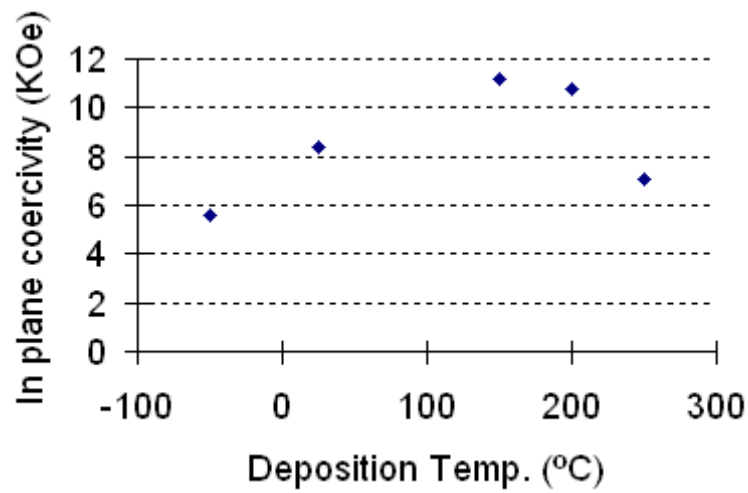
Figure 5.23 The measured LI_0 FePt phase nuclei/grain density versus (a) the deposition temperature and (b) the periodicity of two sets of samples annealed at 400°C for 30 minutes.

5.5 Magnetic properties

The in-plane magnetic properties of 400°C-annealed samples were measured. The results show that both the deposition temperature and periodicity of films have a significant influence on magnetic properties. Figure 5.24 (a) shows the M-H loops of sample “ML_TMP_N50”, “ML_TMP_25”, “ML_TMP_150”, “ML_TMP_200”, and “ML_TMP_250”, and Figure 5.24(b) shows the coercivity versus the deposition temperature for these samples. The sample deposited at 150°C has a maximum coercivity, while those deposited at low and high temperature (-50°C and 250°C, respectively) have a low coercivity. Figure 5.25 (a) shows the M-H loops of sample “ML_PDT_11”, “ML_PDT_21”, “ML_PDT_43”, “ML_PDT_86”, and “ML_PDT_172”, and Figure 5.25(b) shows the coercivity versus the periodicity for these samples. It is obvious that the coercivity increases with the increase of the periodicity.

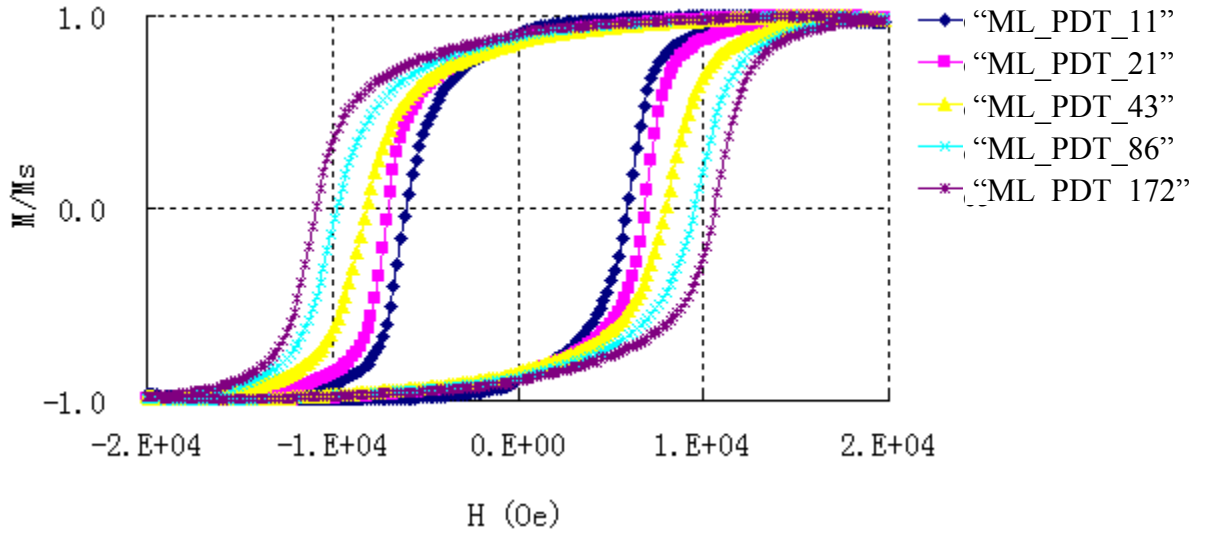


(a)

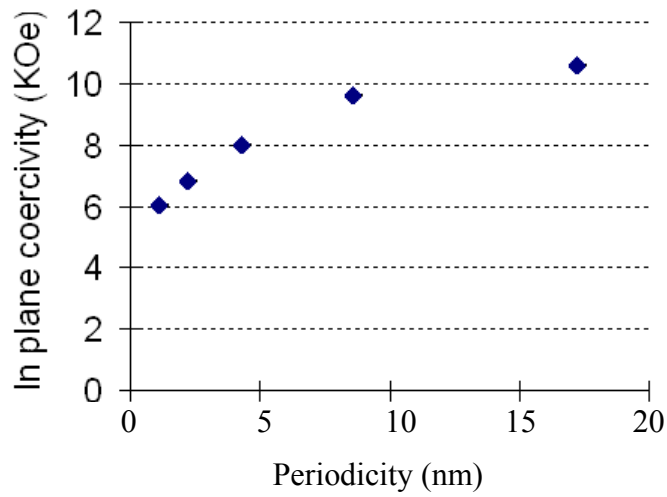


(b)

Figure 5.24 (a) The M-H curves, and (b) the in-plane H_c versus the deposition temperature for samples “ML_TMP_N50”, “ML_TMP_25”, “ML_TMP_150”, “ML_TMP_200”, and “ML_TMP_250”. All samples were annealed at 400°C for 30 minutes.



(a)



(b)

Figure 5.25 (a) The M-H curves, and (b) the in-plane H_c versus the periodicity for samples “ML_PDT_11”, “ML_PDT_21”, “ML_PDT_43”, “ML_PDT_86”, and “ML_PDT_172”. All samples were annealed at 400°C for 30 minutes.

5.6 Discussion

(a) The correlations among effective interdiffusivity, Ll_0 FePt grain size and volume fraction, order parameter (S), and magnetic properties

A correlation between the coercivity and the Ll_0 volume fraction is readily demonstrated. Figure 5.26 shows the in-plane coercivity versus the measured volume fraction of Ll_0 FePt phase for the two sets of samples. The fitted lines indicate that the coercivity of the annealed samples generally increases with the volume fraction for samples in each group, consistent with previous reports [[Barmak et al. \(1996\)](#); [Ristau et al. \(1999\)](#)]. Figure 5.26 also shows that each set of samples has a different rate of coercivity increase with Ll_0 phase fraction, suggesting differences in microstructure and/or extent of ordering between the two sample sets.

Table 5.6 gives a summary of measured parameters for the two sets of samples. A strong positive correlation among effective interdiffusivity, Ll_0 FePt grain size, volume fraction, long range order parameter (measured with the first approach), and magnetic properties is demonstrated. Specifically, samples with larger coercivities generally have larger interdiffusivities, larger Ll_0 FePt grains, larger volume fraction of Ll_0 FePt phase, and larger long-range order parameters (or smaller c/a ratio).

It is well understood that a larger volume fraction and higher degree of ordering of the Ll_0 FePt phase will provide a larger coercivity. In general, for thermally stable grains, a larger grain size is associated with an easier magnetic reversal and hence a lower coercivity. The larger Ll_0 phase grains observed with higher coercivity samples in this study indicates that the growth of Ll_0 FePt phase at the expense of fcc FePt phase is

helpful to increase the volume fraction and ordering. This leads to the conclusion that the development of high coercivity in these annealed films is limited by the density of LI_0 FePt phase nuclei. As is evident from the simultaneous observation of a larger volume fraction of LI_0 FePt phase with a lower grain density, it is the growth of these nuclei that determines the volume fraction transformed.

One question is why some samples show better results (large grain, volume fraction, and higher ordering), while other samples do not. It is understood that the result (e.g., the volume fraction) is determined by the nucleation and growth of LI_0 phase, but the question remains as to why the nucleation and growth of the LI_0 FePt phase is different for these samples. This may be related to the effective interdiffusivity. However, the interdiffusivity alone cannot explain all the results because it has no physical significance when the compositional gradient disappears, which is expected to occur quickly during annealing. This question will be discussed further in the following section.

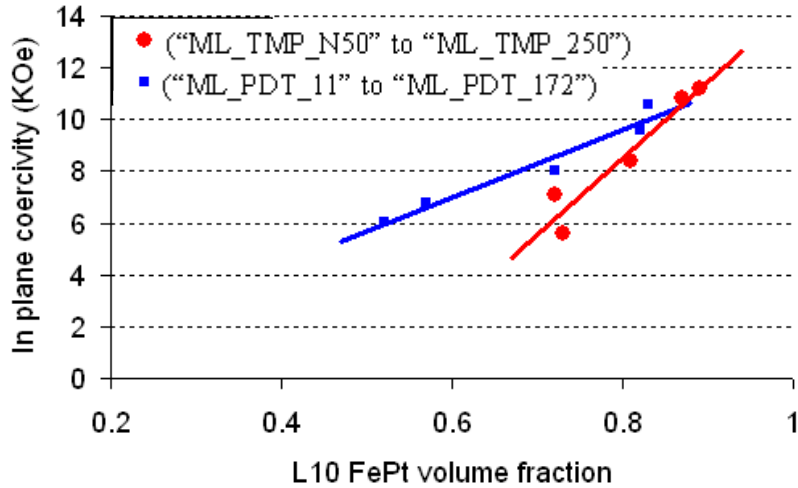


Figure 5.26 The in-plane coercivity versus the $L1_0$ FePt volume fraction of two set of samples with varying substrate temperature (“ML_TMP_N50” to “ML_TMP_250”) and bi-layer periodicity (“ML_PDT_11” to “ML_PDT_172”). All samples were annealed at 400°C for 30 minutes.

Table 5.6 A summary of measured structure and properties of samples

Sample ID	Effective Interdiffusivity (m^2/s)	$L1_0$ phase grain size	$L1_0$ phase fraction	c/a	S	Coercivity (kOe)
“ML_TMP_N50”	$3.84 \times 10^{-10} \exp(-1.5eV/kT)$	small	0.73	0.972	0.683	5.6
“ML_TMP_25”	$1.13 \times 10^{-4} \exp(-2.0 eV/kT)$	medium	0.81	0.966	0.707	8.4
“ML_TMP_150”	N/A	large	0.89	0.965	0.79	11.2
“ML_TMP_200”	$1.06 \times 10^{-4} \exp(-2.0 eV/kT)$	large	0.87	0.964	0.81	10.8
“ML_TMP_250”	N/A	medium	0.72	0.965	0.695	7.1
“ML_PDT_11”	N/A	small	0.52	0.976	0.634	6.01
“ML_PDT_21”	$5.06 \times 10^{-12} \exp(-1.5eV/kT)$	small	0.57	0.972	0.691	6.81
“ML_PDT_43”	$1.18 \times 10^{-6} \exp(-1.9eV/kT)$	medium	0.72	0.966	0.702	8
“ML_PDT_86”	$4.49 \times 10^{-9} \exp(-1.3eV/kT)$	large	0.82	0.965	0.741	9.59
“ML_PDT_172”	N/A	large	0.83	0.964	0.809	10.6

(b) The influence of substrate temperature

The results demonstrate that the deposition temperature of samples strongly influences the Fe-Pt interdiffusivity, microstructure, and magnetic properties. Interestingly, the cold deposited sample (“ML_TMP_N50”) has a lower interdiffusivity, lower ordering, smaller volume fraction, and poor magnetic properties. It was originally thought that a smaller grain size of cold deposited sample should be helpful for the $L1_0$ FePt phase nucleation. The reason is that more grain boundaries, commonly accepted as the ideal heterogeneous nucleation sites, are present in the cold deposited sample. Although it was observed that the nucleation/grain density is higher in the cold deposited films, the phase fraction is small. A very probable reason is that the small grains of *fcc* phase are not helpful for the growth of $L1_0$ phase, as will be explained in detail later.

The annealed sample deposited at 250 °C (“ML_TMP_250”) has poor magnetic properties. The most probable reason is that the deposition at such temperature gives a diffuse interface, since the long distance diffusion can be detected for samples annealed at or above 275°C. On the other hand, the multilayer structures are still intact, as evidenced by the small angle XRD data. This indicates that the interfacial diffusion may happen locally at the interfaces. The reason why the diffuse interfaces influence the phase transformation may be better understood by a comparative study of a set of $[Fe/Pt]_n$ multilayers and FePt alloy films in a subsequent chapter.

Samples deposited in the range of room temperature to 200°C (“ML_TMP_25”, “ML_TMP_150”, “ML_TMP_200”) generally have a similar structure and properties, while the higher temperature deposited sample generally show a greater extent of transformation.

(c) The influence of periodicity

On the influence of periodicity, it was found that the samples with larger periodicity generally have larger interdiffusion, higher ordering, larger $L1_0$ FePt phase grain size and volume fraction, and better magnetic properties. The sample with smaller periodicity, interestingly, does not yield better results. As originally expected, the sample with smaller periodicity has more interfaces given the same total film thickness. Therefore, the sample with smaller periodicity should have more Fe-Pt interfaces, and more nucleation sites since the interfaces can be favored heterogeneous nucleation sites. However, figure 5.23 (b) demonstrates that there is not a large difference in the nucleation/grain density. The smaller periodicity sample has poor $L1_0$ phase formation and magnetic properties.

The set of periodicity samples were deposited at 250°C. It has been suggested from the other samples that this temperature may have a diffuse interface resulting in an inhibited phase transformation. To further confirm the results of the periodicity study, another set of samples with varying periodicity were deposited at room temperature, as shown in table 5.7. This set of samples was annealed, and their magnetic properties were measured. As expected, the same influence of periodicity on the magnetic properties was achieved, as shown in Figure 5.27. Because of the strong correlations of structure and properties, a complete study of the structure of this sample set was not repeated.

An understanding of why samples with large periodicity yield better results is not trivial. It can not be simply explained with the measured effective interdiffusivity, although the Fe/Pt interdiffusion plays a significant role during this process. In our

understanding, as will be explained detail, the growth of LI_0 phase at the expense of fcc phase is more important to determine the final structure and properties.

Table 5.7 A list the $[Fe/Pt]_n$ multilayer films

Sample ID	Multilayer structure	Period (nm)	Depo. Temp. (°C)	Composition	Thickness (nm)
“ML_PDT_RT_10”	$[Fe_{0.5nm}Pt_{0.6nm}]_{48}$	1.0	RT	$Fe_{49}Pt_{51}$	50.0
“ML_PDT_RT_21”	$[Fe_{0.9nm}Pt_{1.2nm}]_{24}$	2.1	RT	$Fe_{49}Pt_{51}$	50.0
“ML_PDT_RT_42”	$[Fe_{1.8nm}Pt_{2.3nm}]_{12}$	4.2	RT	$Fe_{49}Pt_{51}$	50.0
“ML_PDT_RT_83”	$[Fe_{3.7nm}Pt_{4.7nm}]_6$	8.3	RT	$Fe_{49}Pt_{51}$	50.0
“ML_PDT_RT_167”	$[Fe_{7.3nm}Pt_{9.4nm}]_3$	16.7	RT	$Fe_{49}Pt_{51}$	50.0
“ML_PDT_RT_500”	$Fe_{21.9nm}Pt_{28.1nm}$	50.0	RT	$Fe_{49}Pt_{51}$	50.0

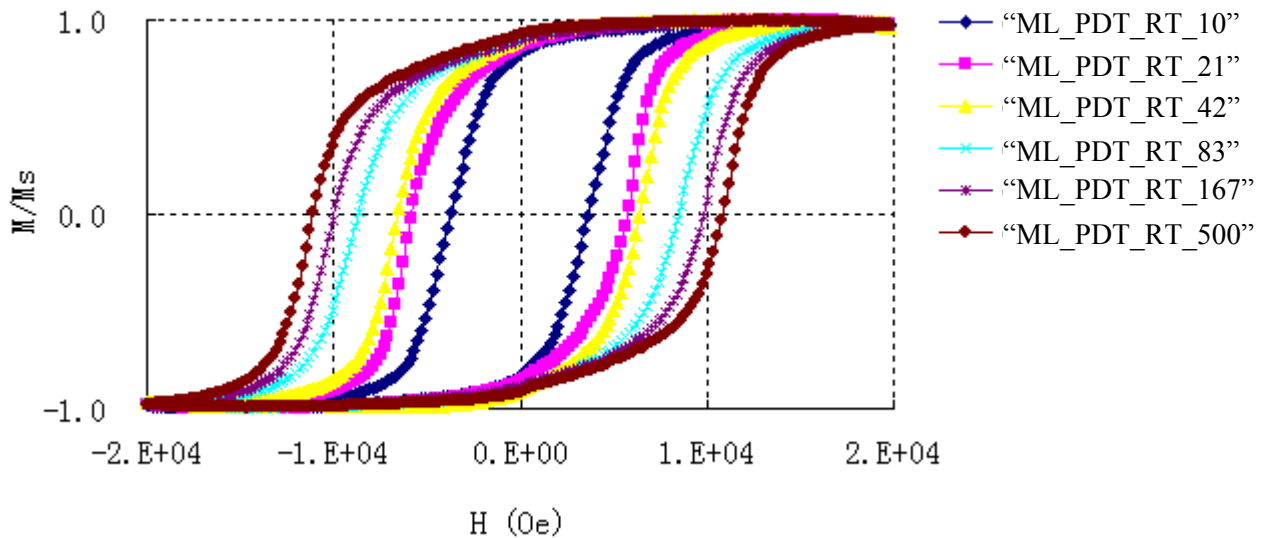


Figure 5.27 The coercivity versus periodicity for a set of samples with varying periodicity at room temperature.

(d) Growth of LI_0 FePt phase

As discussed above, nucleation density is unable to explain the volume fraction transformed and the magnetic properties of these samples. The growth of LI_0 FePt phase plays an important role to determine its volume fraction. This is clearly evident in that all samples with larger volume fraction (also higher ordering and larger H_c) of LI_0 phase also have larger LI_0 grain size. The presence of correlations amongst larger LI_0 grain size, larger volume fraction, higher ordering, and larger coercivity need not be discussed further. The focus of this section is to understand why the LI_0 phase grows faster in some samples, instead of the others.

A review of above samples indicates that all samples having a large grain size and volume fraction of LI_0 phase also have larger grain size for the fcc FePt phase. For the set of sample with varying deposited substrate temperature, samples deposited at 150°C and 200°C obviously have larger grain size of fcc phase than those deposited at room temperature and cold condition. The one deposited at 250°C is an exception, which must be attributed to the diffuse interfaces. That the samples deposited at higher temperature have a larger grain size than those deposited at low temperature is well understood as the grain growth within the initial Pt layer during the deposition is faster at higher temperature. The other set of samples with varying periodicity are also easy to comprehend. During the deposition of polycrystalline multilayers, the nucleation of Fe or Pt occurs at the beginning of the deposition of each layer. The grain size of each layer is closely related to the layer thickness. The as deposited films with larger Pt grain size are expected to have a larger grain size of fcc FePt phase, by as the residual composition gradient serves to limit the fcc FePt growth.

The correlation between *fcc* FePt phase grain size and LI_0 FePt phase grain size (or volume fraction) should not be considered as a coincidence because it is evidential across all samples. Thus it suggests a cause and effect relationship between *fcc* and LI_0 grain size.

The LI_0 FePt phase growth is generally interface controlled, i.e., the jumping of atoms from the *fcc* phase to the LI_0 phase at their interface. The atomic mobility and energy barrier for this atomic jumping at the interface is believed to be related to the misorientation, similar to other material systems [Aaronson et al., (1977); Shewmon, (1969)]. Consequently, different LI_0 grains with different interphase boundary misorientations are very likely to have different growth rates. The HCDF TEM images, (e.g., Figure 5.10), support this explanation. It was observed that several large LI_0 grains, comparable to those of the matrix, coexist with many tiny LI_0 FePt grains mainly located at the grain boundaries. The large LI_0 grains are believed to result from the rapid growth of LI_0 nuclei that have advantageously orientated interphase boundaries, while the much smaller LI_0 grains on the grain boundaries are less advantageously oriented LI_0 grains.

A large variance of growth rate of LI_0 phase grains also explains the correlation between the grain size of *fcc* FePt phase and the LI_0 FePt phase that subsequently grows at its expense. For samples with large *fcc* FePt grain size, there is a greater ability for a LI_0 phase grain with a favorable heterophase interface orientation to consume the large *fcc* FePt grain, but this rapid growth does not extend to neighboring *fcc* FePt grains. This forces a correspondence between the size of the larger LI_0 FePt phase grains and that of the *fcc* FePt grains.

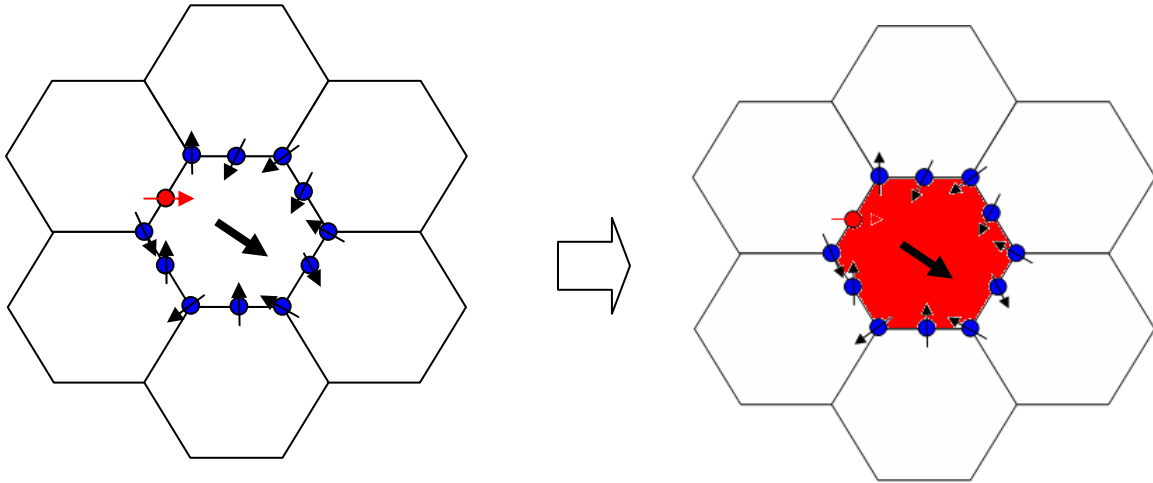


Figure 5.28 A schematic to demonstrate the different growth rates of $L1_0$ FePt grains.

We expect that a similar mechanism may also be invoked for the correlation of *fcc* Pt to *fcc* FePt grain size, if it is assumed that the *fcc* FePt forms by nucleation and growth.

5.7 Conclusions

A more comprehensive study of annealed $[\text{Fe/Pt}]_n$ films is provided concerning the phase fraction, grain size, nucleation/grain density, interdiffusivity, long-range order parameter, and magnetic properties. A method based on hollow cone dark field TEM is introduced to measure the volume fraction, grain size, and density of ordered $L1_0$ FePt phase grains in the annealed films, and a model based on low-angle X-ray diffraction is used to measure the effective Fe-Pt interdiffusivity.

The process-structure-properties relations of two groups of samples with varying substrate temperature and periodicity are reported. The results demonstrate that the processing parameters (substrate temperature, periodicity) have a strong influence on the structure (effective interdiffusivity, $L1_0$ phase volume fraction, grain size and density) and magnetic properties. The correlation of these parameters suggests that the annealed $[\text{Fe/Pt}]_n$ multilayer films have limited nuclei, and the following growth of $L1_0$ phase is very important to the extent of ordered phase formed. A correlation between the grain size of fcc FePt phase and the $L1_0$ FePt phase fraction (or magnetic properties) strongly suggests that the phase transformation of $fcc \rightarrow L1_0$ is highly dependent on the grain size of the parent fcc FePt phase. This phenomenon results from the higher (several orders) growth rate of special incoherent interphase boundaries.

CHAPTER 6 THE INFLUENCE OF THE FILM THICKNESS ON THE FORMATION OF L_{10} FePt PHASE

6.1 Introduction

In chapter five, it has been demonstrated that the periodicity and substrate temperature have a significant influence on the structure and magnetic properties of annealed films. All of the films described in chapter 5 have the same film thickness and average composition. In this chapter, the influence of total film thickness is studied, while the deposition temperature and periodicity are kept the same.

The study of the influence of the film thickness on L_{10} FePt phase formation has the same significance, if not greater, than the previously described studies. First of all, the potential applications of the L_{10} FePt phase motivate the study of films with different thicknesses. For example, films for magnetic recording are required to be very thin, usually below 10 nm (in longitudinal mode, as example) and potentially as thin as 2 to 3 nm. For magnetic MEMS applications, however, a much greater thickness, in μm scale, is usually necessary. The other significance of this study is to further understand the reaction mechanisms of the multilayers and formation of L_{10} FePt. Previously, we demonstrated that the growth of L_{10} FePt phase is strongly correlated to the structure and magnetic properties of the samples. Grain growth in thin films is highly correlated with film thickness and thus the total sample thickness can be expected to have a significant influence on the structure and magnetic properties of annealed samples, even when the bi-layer periodicity is unchanged.

For co-sputtered FePt alloy films, the relationships between sample thickness and the sample structure and magnetic properties have been widely reported [Berry et al. (2007); Lim et al. (2004); Toney et al. (2003); Minh et al. (2004); Chena et al. (2004)]. For example, Berry and Barmak et al. [Berry et al. (2007)] modeled the TTT diagram of $fcc \rightarrow LI_0$ phase transformation based on DSC experiments, which, along with the experimentally measured LI_0 phase fraction of annealed FePt films (10 nm thick) by Ristau and Barmak et al. [Barmak et al. (1996); Ristau et al. (1999)], demonstrated that the phase transformation is more difficult in thin FePt alloy films (10 nm and 50 nm) than that in thick films (1 μm). Most other studies [Lim et al. (2004); Toney et al. (2003); Minh et al. (2004); Chena et al. (2004)], mainly based on the magnetic properties, reported a similar trend wherein thinner films show a lower coercivity upon annealing.

In this chapter, the film thickness dependence of structure and magnetic properties of annealed $[\text{Fe}_{4\text{nm}}/\text{Pt}_{5.13\text{nm}}]_n$ ($n=1, 3, 6, 9, 12$) multilayer films were carefully studied. A similar study on the total film thickness effects in multilayers has not been previously reported. Also in this chapter, the thickness effects of the multilayer samples and co-sputtered alloy film samples are compared.

6.2 Experiments

The samples sputtered for the investigation are listed in table 6.1. It can be noted that all films have the same Fe/Pt ratio (therefore the same composition of the annealed samples). The multilayer films (“ML_THK_8” to “ML_THK_100”) have the same bi-layer periodicity. A large bi-layer periodicity about 8 nm is chosen based on the previous studies indicating that samples with larger periodicity have a larger LI_0 phase fraction, higher long-range order parameter, higher coercivity after the same heat treatment.

All samples were sputtered onto Si (100) substrates having a surface layer of 200 nm of thermally grown SiO_2 at room temperature. The deposition rate for $[\text{Fe/Pt}]_n$ multilayer films is 0.31 Å/sec for Pt and that for Fe is 0.48 Å/sec. For FePt alloy films, the deposition rate is 0.96 Å/sec. The deposition rate of Fe and Pt was characterized with RBS. All depositions were performed in 4 mTorr of Ar + 3% H_2 , and controlled by an automated program.

Table 6.1 A list of samples sputtered at room temperature for investigation

Short ID	Film structure	Composition	Thickness (nm)
“ML_THK_8”	[Fe _{3.6nm} Pt _{4.7nm}] ₁	Fe _{49.0} Pt _{51.0}	8
“ML_THK_25”	[Fe _{3.6nm} Pt _{4.7nm}] ₃	Fe _{49.0} Pt _{51.0}	25
“ML_THK_50”	[Fe _{3.6nm} Pt _{4.7nm}] ₆	Fe _{49.0} Pt _{51.0}	50
“ML_THK_73”	[Fe _{3.6nm} Pt _{4.7nm}] ₉	Fe _{49.5} Pt _{50.5}	73
“ML_THK_100”	[Fe _{3.6nm} Pt _{4.7nm}] ₁₂	Fe _{49.5} Pt _{50.5}	100
“A1_THK_7”	Fe ₅₀ Pt ₅₀	Fe _{50.0} Pt _{50.0}	7
“A1_THK_25”	Fe ₅₀ Pt ₅₀	Fe _{50.0} Pt _{50.0}	25
“A1_THK_50”	Fe ₅₀ Pt ₅₀	Fe _{50.0} Pt _{50.0}	50
“A1_THK_73”	Fe ₅₀ Pt ₅₀	Fe _{50.0} Pt _{50.0}	73
“A1_THK_100”	Fe ₅₀ Pt ₅₀	Fe _{50.0} Pt _{50.0}	100
“A1_THK_200”	Fe ₅₀ Pt ₅₀	Fe _{50.0} Pt _{50.0}	200

6.3 Results

6.3.1 Multilayer samples (“ML_THK_8” to “ML_THK_100”)

(a) Grain size and $L1_0$ phase fraction

Figure 6.1 and Figure 6.2 show the HCDF TEM images from the 001_{L1_0} and 110_{L1_0} superlattice reflections for multilayer samples “ML_THK_8” to “ML_THK_100” annealed at 400 °C and 500 °C for one hour, respectively. Clearly demonstrated is the increase of $L1_0$ phase grain size with the increase of film thickness.

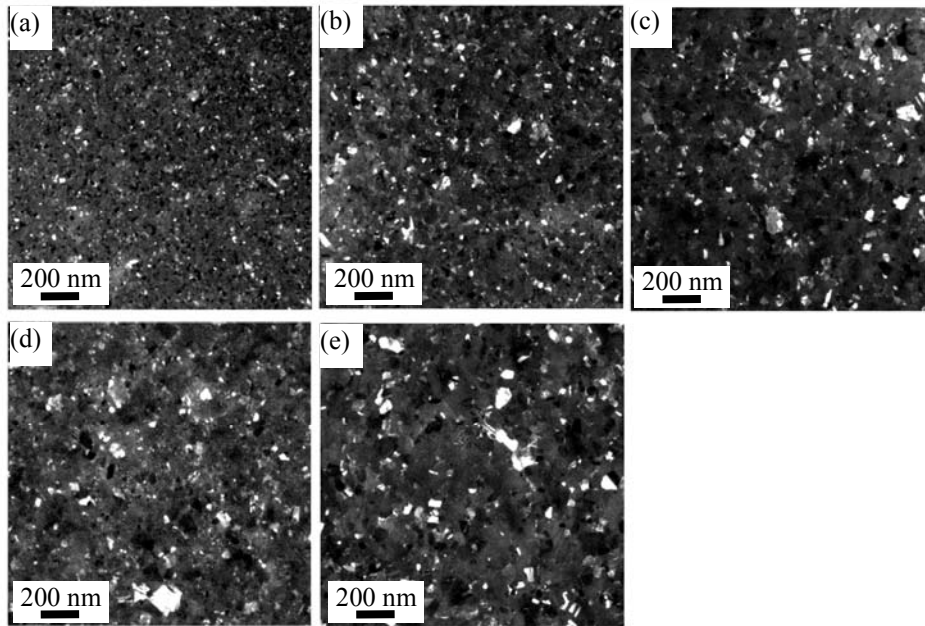


Figure 6.1 (a) to (e) are the plan view HCDF TEM images using 001 and 110 reflections of $L1_0$ FePt phase for samples “ML_THK_8”, “ML_THK_25”, “ML_THK_50”, “ML_THK_73”, and “ML_THK_100” annealed at 400 °C for 1 hour, respectively.

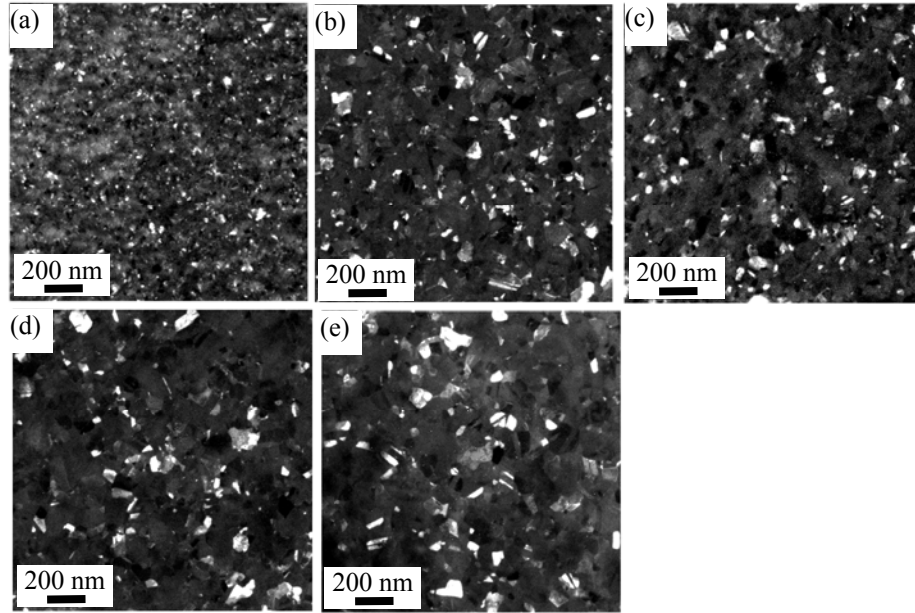


Figure 6.2 (a) to (e) are the plan view HCDF TEM images using 001 and 110 reflections of $L1_0$ FePt phase for samples “ML_THK_8”, “ML_THK_25”, “ML_THK_50”, “ML_THK_73”, and “ML_THK_100” annealed at 500 °C for 1 hour, respectively.

The technique described in chapter five for the $L1_0$ FePt phase volume fraction determination was used to study these samples, as well. For each sample, the HCDF TEM images from $(201+112)_{L1_0}$, $(001+110)_{L1_0}$ and $(201+112)_{L1_0} + \{200+220\}_{fcc+L1_0}$ reflections were acquired to confirm the lower image contrast of $(201+112)_{L1_0}$ illuminated grains, in order to safely apply the technique. Figure 6.3 (a), (b), (c), and (d) shows the bright field (BF), HCDF TEM images from $(001+110)_{L1_0}$, $(201+112)_{L1_0}$, and $(201+112)_{L1_0} + \{200+220\}_{fcc+L1_0}$ reflections of sample “ML_THK_100” annealed at 500°C for 1 hour, the best ordered example in the studied group.

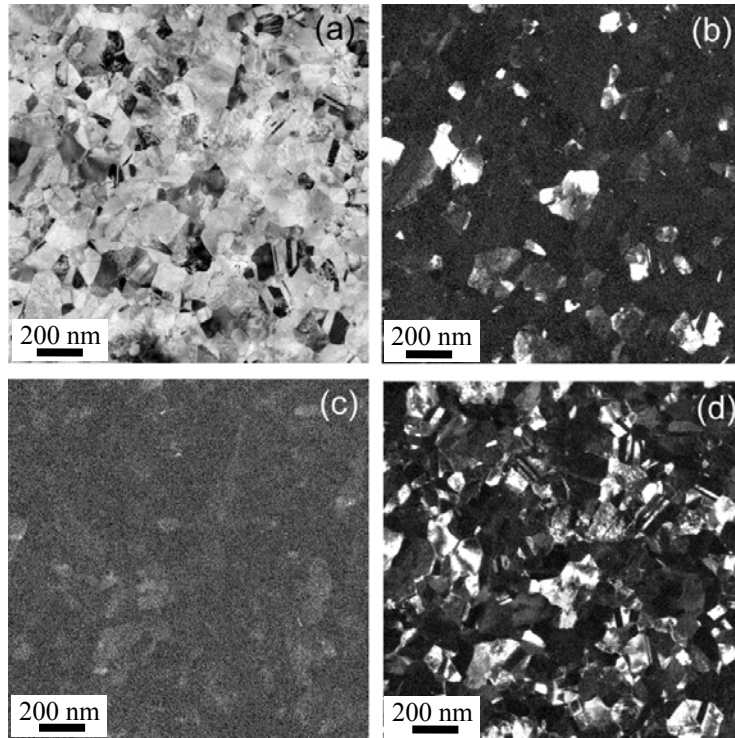


Figure 6.3 (a), (b), (c), and (d) shows the BF, HCDF TEM images from $(001+110)_{L1_0}$, $(201+112)_{L1_0}$, and $(201+112)_{L1_0} + \{200+220\}_{fcc+L1_0}$ reflections of sample “ML_THK_100” annealed at 500°C for 1 hour. The same CCD integration time (32 seconds) is applied. A much lower illumination intensity of $(201+112)_{L1_0}$ grains compared to that of $(001+110)_{L1_0}$ grains or $\{200+220\}_{fcc+L1_0}$ is well demonstrated.

Figure 6.4 shows the $L1_0$ FePt phase fraction versus film thickness of multilayer samples annealed at 400°C and 500°C for one hour. It clearly demonstrates a strong thickness dependence of $L1_0$ phase fraction in the annealed films. A phase fraction close to 1 was achieved for sample “ML_THK_100” annealed at 400 °C for 1 hour, which indicates that a complete $L1_0$ FePt phase can be formed relatively easily in thicker $[Fe/Pt]_n$ films. On the other side, the fraction is small in annealed 8 nm thick Fe/Pt bi-

layer film, sample “ML_THK_8”. It only has a LI_0 phase fraction of 0.36 for the 400°C annealed sample. All samples except sample “ML_THK_8”, annealed at 500°C, have a volume fraction close to 1. The thinnest one, however, still has a very limited LI_0 FePt phase (59%).

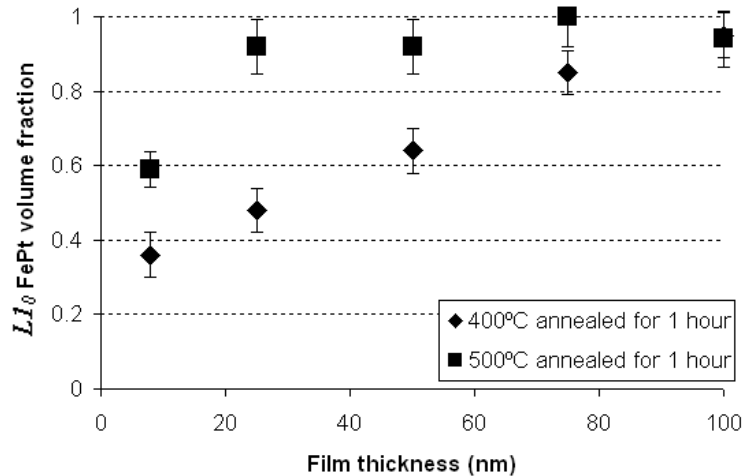


Figure 6.4 The LI_0 FePt phase fraction of versus film thickness for samples “ML_THK_8”, “ML_THK_25”, “ML_THK_50”, “ML_THK_73”, and “ML_THK_100” annealed at 400 °C and 500 °C for 1 hour.

(b) c/a ratio and long-range order parameter

Figure 6.5 shows the XRD patterns of samples “ML_THK_25”, “ML_THK_50”, “ML_THK_73”, “ML_THK_100” annealed at 400°C for 1 hour. The pattern of the thinnest one, sample “ML_THK_8”, is unavailable due to its thickness of only 8 nm. The extra peaks as shown at two theta degree of 30, 36, 45 are from the substrate or mounting clay. Similar reflections corresponding to these extra peaks are not observed in the SADP of samples. The long-range order parameters of these samples are shown in

Figure 6.6. The S determined with the second approach (I_{002} modified with LI_0 volume fraction) shows a value higher than 1. This is probably due to the presence of some $\langle 001 \rangle$ fiber texture, as justified by a similar intensity of 002 peak and 200 peak for sample “ML_THK_25” and “ML_THK_50”. For purely ordered LI_0 phase without any texture, the 002 peak should have an intensity only half than that of 200 peak.

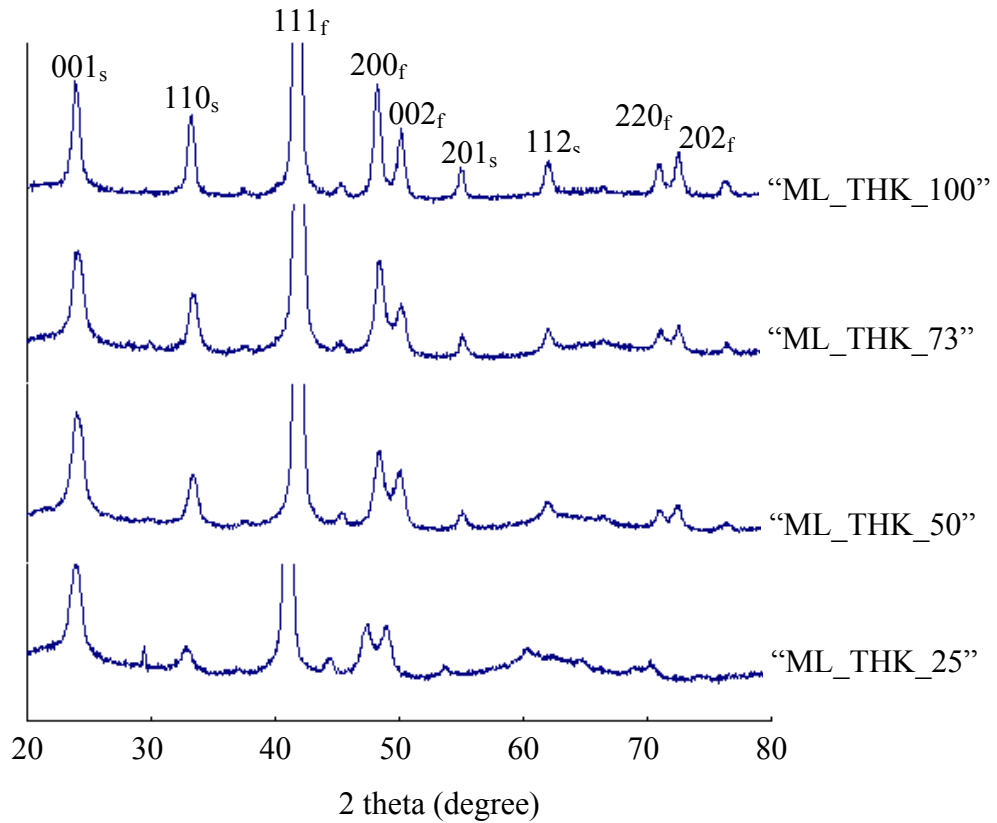


Figure 6.5 The XRD patterns of samples “ML_THK_25”, “ML_THK_50”, “ML_THK_73”, and “ML_THK_100” annealed at 400 °C for 1 hour.

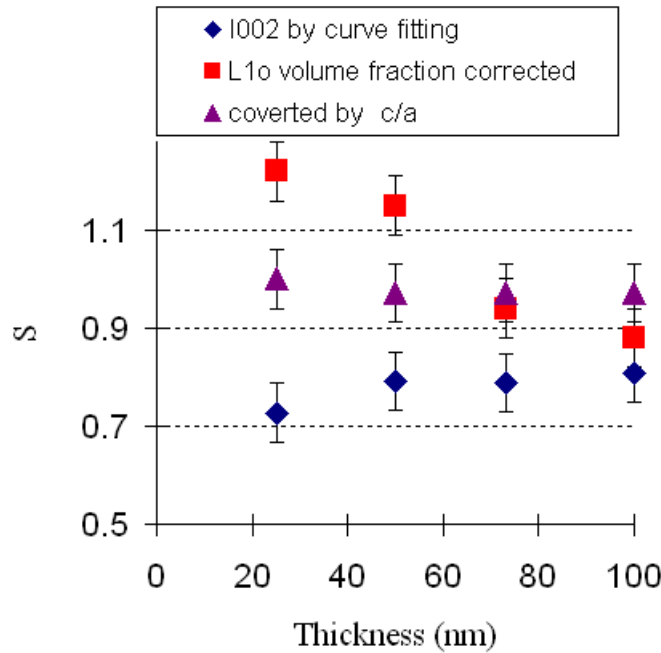
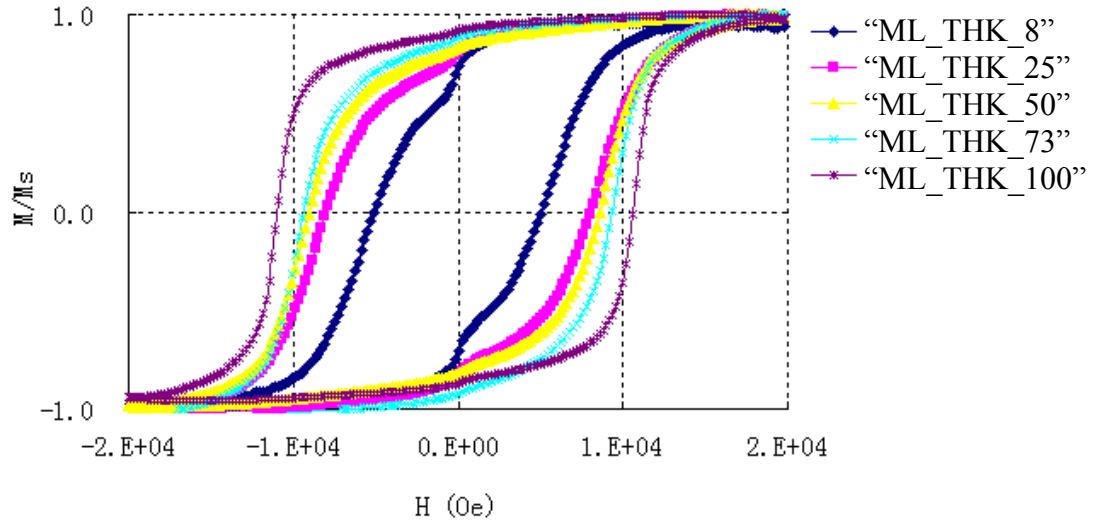


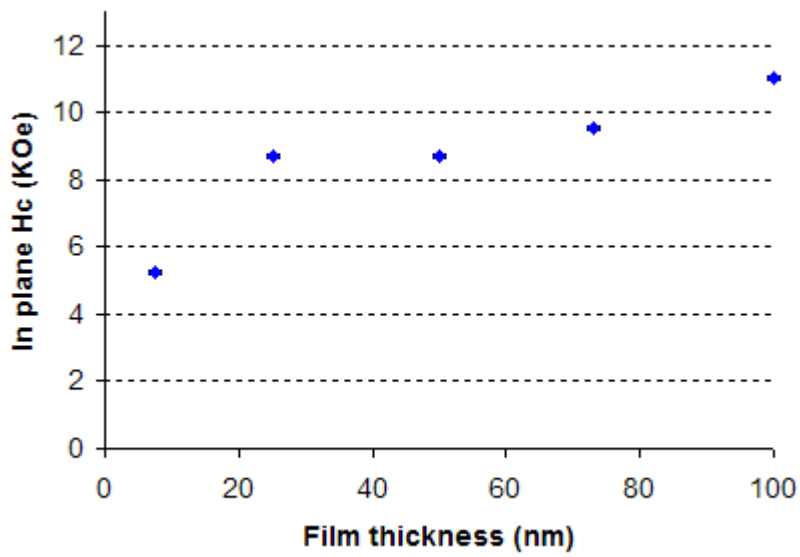
Figure 6.6 The long-range order parameter of samples “ML_THK_25”, “ML_THK_50”, “ML_THK_73”, and “ML_THK_100” annealed at 400 °C for 1 hour.

(c) Magnetic properties

Figure 6.7 shows the estimated in-plane coercivity of $[\text{Fe}/\text{Pt}]_n$ multilayer films annealed at 400 °C. The magnetic properties of samples annealed at 500°C are not available because the instrument used (AGFM) has only a 22 kOe maximum field and is unable to saturate these samples. It should also be noted that that M-H loops measured for samples annealed at 400 °C (figure 6.7 (a)) may also not be fully saturated, i.e., these may be minor loops. It can be seen from Figure 6.7 that the coercivity versus film thickness has a similar trend as $L1_0$ FePt phase fraction.



(a)



(b)

Figure 6.7 The a) M-H curves and b) in-plane coercivity versus film thickness for samples “ML_THK_8”, “ML_THK_25”, “ML_THK_50”, “ML_THK_73”, and “ML_THK_100” annealed at 400 °C for 1 hour.

6.3.2 Comparison of $[\text{Fe}/\text{Pt}]_n$ with co-sputtered FePt samples

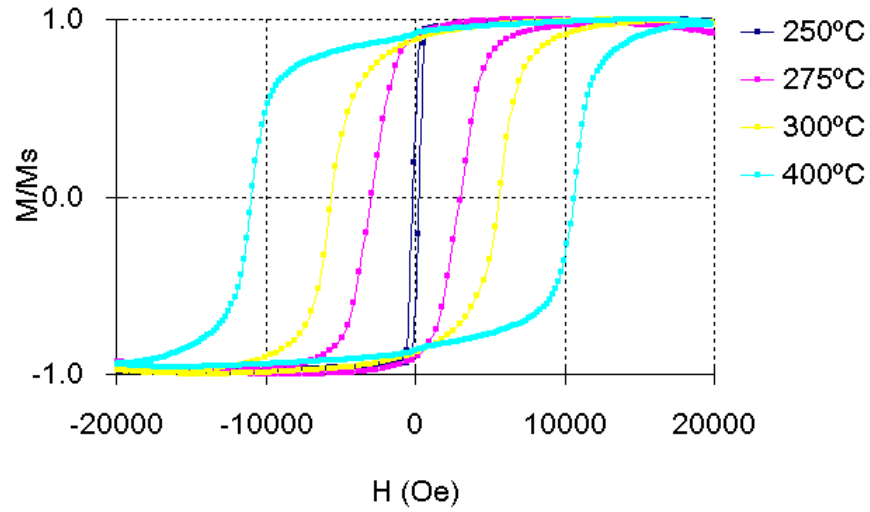
(a) Nucleation temperature

It has been commonly accepted that the heat treatment of $[\text{Fe}/\text{Pt}]_n$ multilayer films is one approach to achieve the $L1_0$ FePt phase at a lower processing temperature. However, as will be demonstrated, the initial formation temperature of the $L1_0$ phase is basically the same for both the co-sputtered FePt alloy films and the $[\text{Fe}/\text{Pt}]_n$ multilayer films.

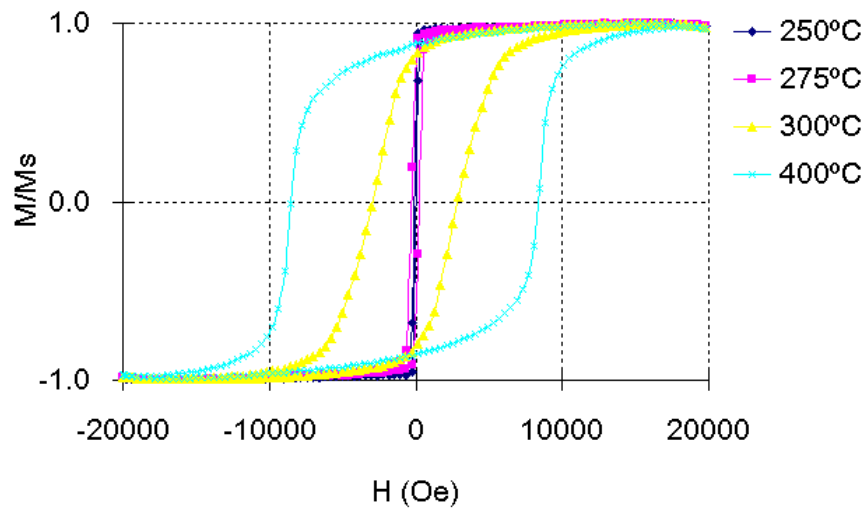
Due to the thickness dependence, the FePt co-sputtered films and the multilayer films with the same thickness must be selected to compare the temperature at which the formation of the $L1_0$ phase takes place. In this section, sample “ML_THK_100” and “A1_THK_100” were chosen to be annealed at 250°C, 275°C, 300°C, and 400 °C for 1 hour. Both samples have the same thickness of about 100nm. The corresponding magnetic properties are shown in figure 6.8 (a) and (b) for sample “ML_THK_100” and “A1_THK_100”, respectively.

Because the $L1_0$ FePt phase is the only phase in Fe-Pt system having large anisotropy energy density and able to provide high coercivity, the appearance of high coercivity (>1 kOe) indicates the formation of some amount of the $L1_0$ phase. Figure 6.8 shows that the ordered phase was formed for sample “ML_THK_100” annealed at or higher than 275°C, while it appeared for sample “A1_THK_100” annealed at or higher than 300°C. The difference of 25 °C cannot be considered as significant. Both samples annealed at 250°C show a very soft magnetic behavior.

A clear difference of the magnetic properties of co-sputtered alloys and multilayer films can be understood as the difference in the Ll_0 phase fraction and ordering, which will be understood further.



(a)



(b)

Figure 6.8 The M-H curves of (a) sample co-sputtered FePt film “ML_THK_100” and multilayer film “A1_THK_100” annealed at different temperature for one hour.

(b) Grain size

Figure 6.9 and 6.10 show the $L1_0$ FePt phase grains for samples “A1_THK_7” to “A1_THK_200” annealed for 1 hour at 400°C and 500°C, respectively. A comparison of the measured $L1_0$ FePt phase grain size of $[\text{Fe/Pt}]_n$ multilayer films and FePt alloy films annealed at the 400°C is shown in Figure 6.11. It can be seen that the $L1_0$ FePt phase grains in co-sputtered films generally are smaller than those in the annealed multilayers with the same thickness. In both annealed multilayers and FePt alloy films, it was observed that the size of $L1_0$ FePt phase grains increase with the increase the film thickness, although the tendency of the trend is different.

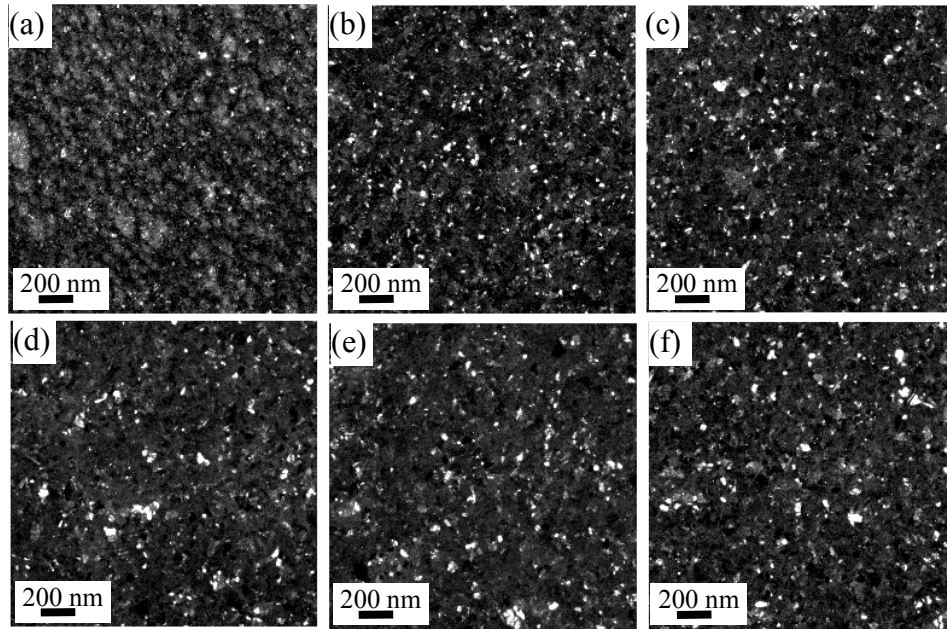


Figure 6.9 (a) to (f) are the plan view HCDF TEM images using 001 and 110 reflections of $L1_0$ FePt phase for samples “A1_THK_7”, “A1_THK_25”, “A1_THK_50”, “A1_THK_73”, “A1_THK_100”, and “A1_THK_200” annealed at 400 °C for 1 hour, respectively.

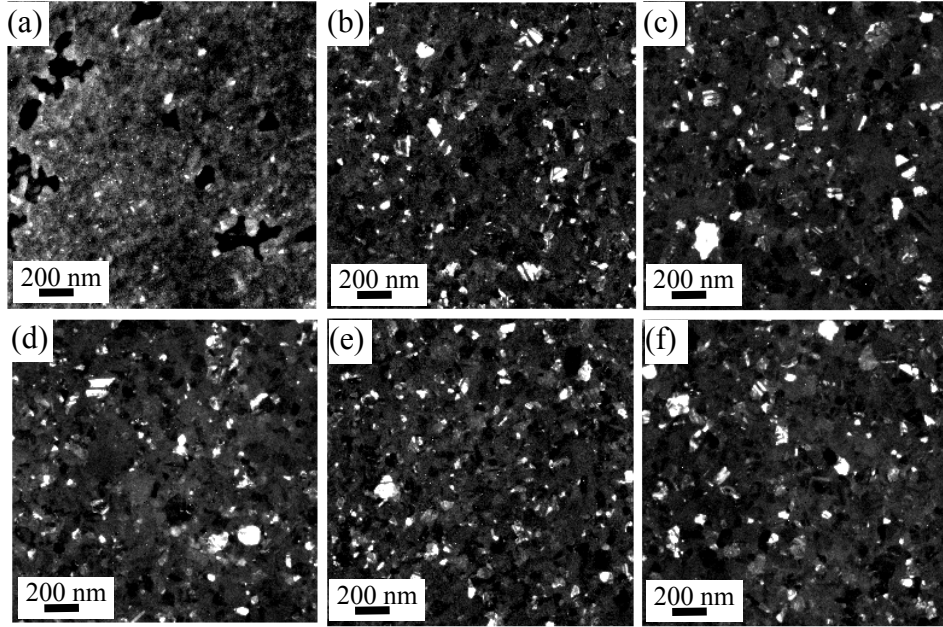


Figure 6.10 (a) to (f) are the HRTEM images using 001 and 110 reflections of $L1_0$ FePt phase for samples “A1_THK_7”, “A1_THK_25”, “A1_THK_50”, “A1_THK_73”, “A1_THK_100”, and “A1_THK_200” annealed at 500 °C for 1 hour, respectively.

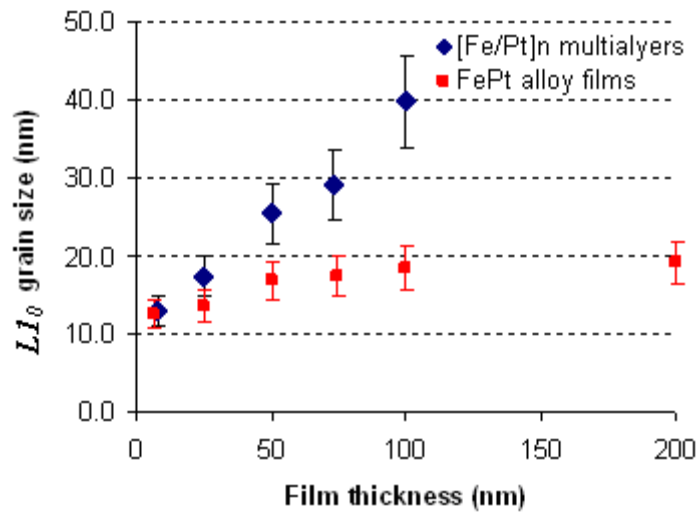


Figure 6.11 A comparison of measured $L1_0$ FePt phase grain size in $[Fe/Pt]_n$ multilayer films (“ML_THK_8” to “ML_THK_100”) and FePt alloy films (“A1_THK_7” to “A1_THK_200”) annealed at 400°C for 1 hour.

(c) $L1_0$ Phase fraction and ordering of annealed films

The quantification of $L1_0$ phase fraction in the annealed films is important to understanding the reaction mechanisms. Figure 6.12 shows the phase fraction of annealed film versus the film thickness of two sets of samples. Similar to that of multilayers, a steady increase of volume fraction was observed from 8 nm to 25 nm. From 25 nm to 200 nm, however, the volume fraction of $L1_0$ phase in FePt alloy films increases very slowly from 53% to 64%, which is different from the steady increase of volume fraction for multilayers.

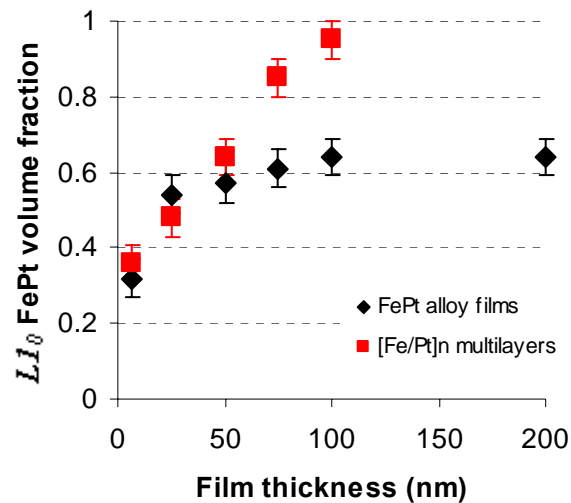


Figure 6.12 The $L1_0$ FePt phase fraction of versus film thickness for FePt alloy samples (“A1_THK_7” to “A1_THK_200”) and $[\text{Fe}/\text{Pt}]_n$ multilayer films (“ML_THK_8” to “ML_THK_100”) annealed at 400 °C for 1 hour.

Figure 6.13 shows the measured $L1_0$ FePt nucleation/grain density of $[\text{Fe}/\text{Pt}]_n$ multilayer films and FePt alloy films annealed at 400°C 1 hour. It demonstrates that the

nuclei/grain density in FePt alloy film is generally higher than that in the annealed $[\text{Fe}/\text{Pt}]_n$ multilayer films.

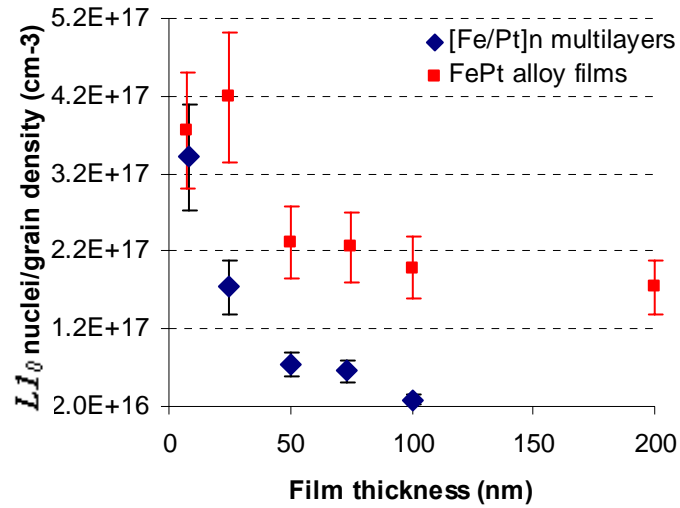


Figure 6.13 A comparison of measured $L1_0$ FePt phase nuclei/grain density in $[\text{Fe}/\text{Pt}]_n$ multilayer films (“ML_THK_8” to “ML_THK_100”) and FePt alloy films (“A1_THK_7” to “A1_THK_200”) annealed at 400°C for 1 hour.

Figure 6.14 shows the c/a ratio versus film thickness for these samples annealed at 400 °C for 1 hour. These values were determined through the 001 and 110 superlattice reflections of TEM diffraction pattern. The c/a ratio of these samples indicates that the extent of ordering in the $L1_0$ FePt phase of the alloy films is not very sensitive to the film thickness.

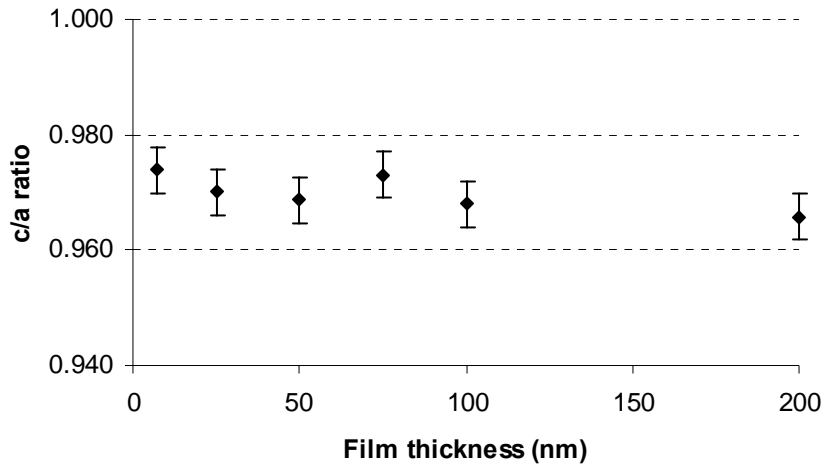
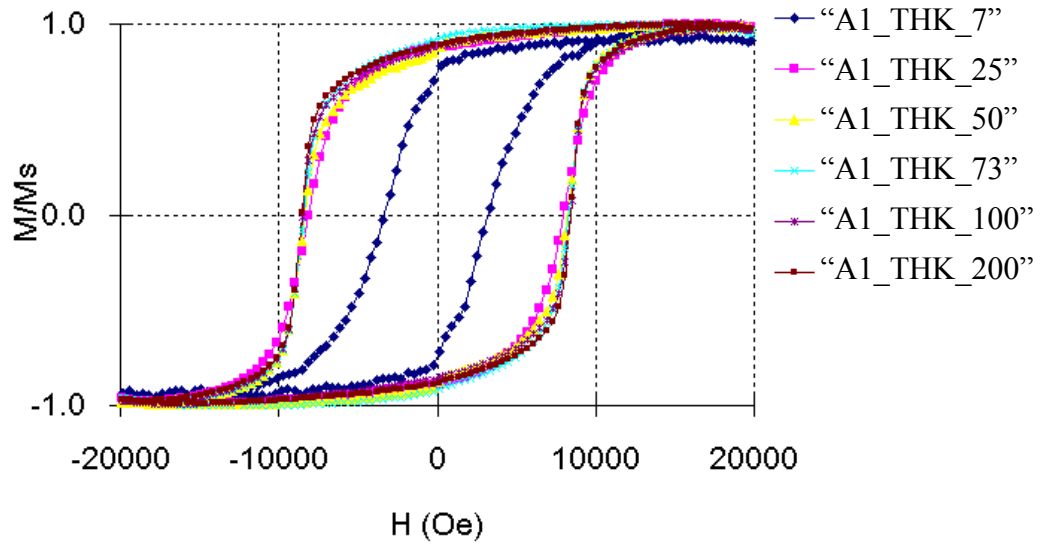


Figure 6.14 The c/a ratio versus film thickness for samples “A1_THK_7”, “A1_THK_25”, “A1_THK_50”, “A1_THK_73”, “A1_THK_100” and “A1_THK_200” annealed at 400 °C for 1 hour.

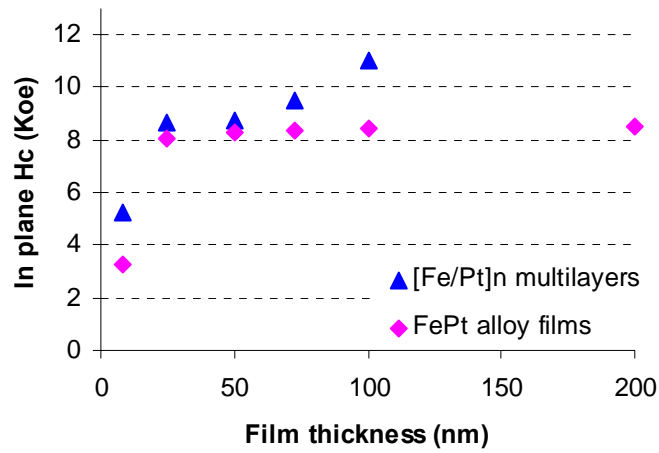
(d) Magnetic properties

Figure 6.15 (a) shows the M-H curves and coercivity of sample “A1_THK_7” to “A1_THK_200” annealed at 400 °C for one hour. The 8 nm thick film has a very low coercivity, other films, however, have similar M-H curves. Figure 6.15 (b) indicates that the coercivity very slightly increases for the FePt alloy film with thickness in the range of 25 nm to 200nm.

It is interesting to compare the coercivity of FePt alloy films and $[\text{Fe}/\text{Pt}]_n$ multilayer films. First of all, the annealed $[\text{Fe}/\text{Pt}]_n$ multilayer film generally has a higher coercivity than that of the annealed co-sputtered sample with the same thickness. Secondary, the magnetic properties of co-sputtered samples show a very weak trend with the film thickness compared to those of the $[\text{Fe}/\text{Pt}]_n$ multilayer films.



(a)



(b)

Figure 6.15 The (a) M-H curves, and (b) the coercivity of samples “A1_THK_7” to “A1_THK_200” annealed at 400 °C for 1 hour. As a comparisons, the coercivities of annealed [Fe/Pt]_n multilayer films (“ML_THK_8” to “ML_THK_100”) were also included.

6.4 Discussion and conclusions

The positive correlations among LI_0 phase grain size, volume fraction, and coercivity are also observed for the samples investigated in this chapter, similar to that observed for the samples described in chapter 5. The results further confirm that the conclusions drawn in previous chapter are valid.

The correlation between fcc grain size and LI_0 grain size is also followed. In $[Fe/Pt]_n$ multilayer films, both fcc grains and LI_0 grains increase with the increase with the film thickness, which is very consistent with the known trend of grain size scaling with film thickness. In FePt alloy films, however, the LI_0 FePt grains in films thicker than 50 nm have a similar size. A close examination of the BF TEM image, as shown in Figure 6.16, suggests that there is no significant difference of the fcc phase grain size. Such results, from another aspect, further confirm the influence of fcc grain size on the LI_0 phase formation.

A general trend of better results (larger LI_0 phase grain size, volume fraction, and higher coercivity) are observed for thicker samples. The different degree of this trend in $[Fe/Pt]_n$ multilayer films and FePt alloy films will be discussed later. The general trend can be explained through the different nucleation and phase growth behaviors in samples with different thicknesses.

Grain growth in thin films generally starts in the film thickness and in-plane directions to form a columnar structure. When the in-plane grain size is near the film thickness, grain growth slows substantially and this stage is called stagnation. A higher annealing temperature is needed to provide further in-plane grain growth [Thompson

(1990)]. Therefore, it is expected that the growth of $L1_0$ FePt phase at the expense of fcc phase in thicker film is greater and that larger grains are formed than those in thinner films.

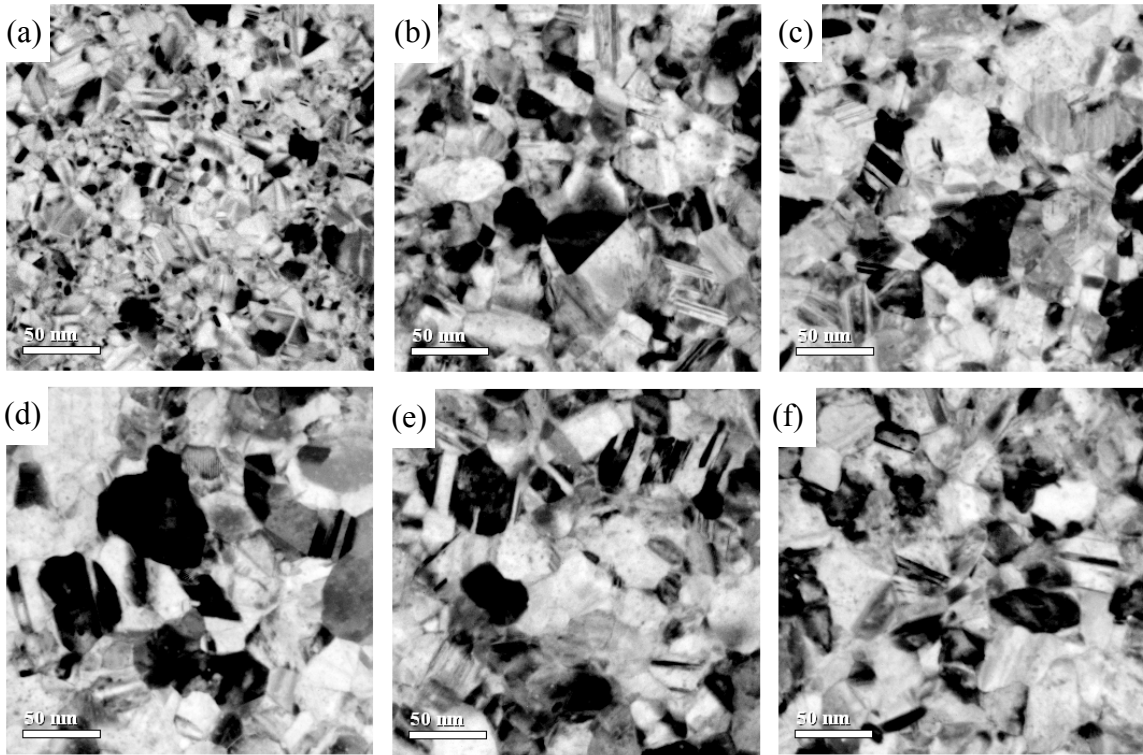


Figure 6.16 (a) to (f) shows the BF TEM images of samples “A1_THK_7” (7 nm), “A1_THK_25” (25 nm), “A1_THK_50” (50 nm), “A1_THK_73” (73 nm), “A1_THK_100” (100 nm), and “A1_THK_200” (200 nm) annealed at 400 °C for 1 hour, respectively.

A decrease in the volume fraction transformed with decreasing sample thickness is consistent with relatively simple models of the phase transformations by nucleation and growth [Berry and Barmak, (2007); Balluffi et al. (2005)]. However, for quantitative

use these models require a uniform growth rate for the transformed phase, which we do not observe due to the tendency for grain growth to stagnate when the grain size becomes comparable to film thickness. Further, it was found in both sets of samples that thinner samples do not show a reduced nucleation/grain density. This may suggest that the edge effect predicted for uniform nucleation and growth by Avrami-Johnson models does not have a significant influence on the $L1_0$ phase formation in these samples.

The different extent to which film structure and properties are related to the film thickness in $[\text{Fe}/\text{Pt}]_n$ multilayers and FePt alloy films can be explained by consideration of the driving force for phase and grain growth that are available in the as-deposited films. As illustrated in Figure 6.17, pure $[\text{Fe}/\text{Pt}]_n$ multilayers have a higher energy than that of the FePt alloy films and ordered $L1_0$ FePt material. It is believed that this extra energy in $[\text{Fe}/\text{Pt}]_n$ multilayer films is helpful for *fcc* FePt grain growth, which in turn aids the $L1_0$ phase growth, which results in a larger $L1_0$ volume fraction than the FePt alloy films.

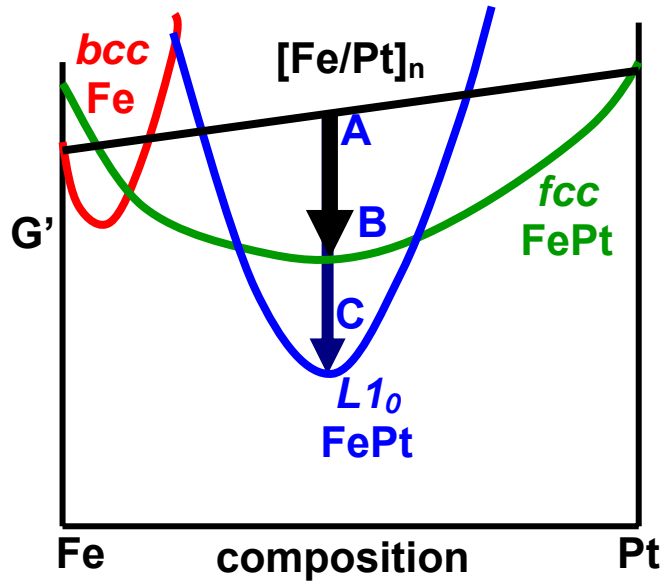


Figure 6.17 A schematic showing the relative energy of $[\text{Fe/Pt}]_n$ multilayers, FePt alloys, and order $L1_0$ phase. Point “A” indicates the Gibbs free energy of $[\text{Fe/Pt}]_n$ multilayer films. Point “B” indicates the Gibbs free energy of disordered fcc FePt alloy films, and point “C” indicates the Gibbs free energy of ordered $L1_0$ FePt samples. Point “A”, “B”, and “C” indicate the energy of samples with the same average composition of $\text{Fe}_{50}\text{Pt}_{50}$.

CHAPTER 7 EXCHANGE SPRING MAGNETS INVESTIGATION

7.1 Introduction and review

The principle of exchange spring magnets has been described in the first chapter. To construct an exchange spring magnet nanocomposite, the soft phase with high saturation magnetization is coupled with the hard phase with a high coercivity, and the exchange coupling between the two phases must be strong enough so that they can be reversed together during the demagnetization. For the $L1_0$ FePt based magnets, the $L1_0$ FePt phase is the hard phase with high anisotropy energy which provides a high coercivity, and the soft phase introduced can be any phase with a higher M_s than that of $L1_0$ FePt, such as Fe_3Pt , disordered FePt, Fe, Fe_2B et al.

Table 7.1 gives a summary of $L1_0$ FePt based exchanged spring magnets. The results can be simply classified into four groups. Earlier studies from Liu et al. [Liu et al., (1997, 1998, 1999)] reported very large value of $(BH)_{max}$ in the range of 30 ~ 50MGOe. Following reports on varying materials and processing techniques, however, give energy products much lower than those earlier reports, as see group II. Group III lists the studies by adding small concentration of tertiary elements. It is very interesting to see a dramatic increase of the energy product with small addition of ternary elements. One explanation is that these tertiary elements delayed the formation of ordering phase; so that a mixture of disordered and ordered phases was achieved. Group IV includes some recent reports using the exchange coupling of $L1_0$ FePt and Fe_2B .

Another important parameter, besides the energy product, is the processing temperature of the nanocomposites. For many application of this magnet (magnetic

MEMS, e.g.), an annealing temperature at, or lower than, 400°C is highly desirable. Most studies in table 7.1 usually have a much higher processing temperature.

A much lower energy product than what the theory predicted, as well as a higher processing temperature than what the applications required, drives the studies in this chapter. The influence of composition and annealing conditions on the energy product are studied systematically.

Table 7.1 A review of $L1_0$ FePt based exchange spring magnets

Group	Exchange couples	Prepared sample	Processing condition	$(BH)_{max}$ (MGOe)	references
I	$L1_0$ FePt ~ Fe ₃ Pt	Fe/Pt MLs (Fe:Pt=2:1)	Step1: RTA (500°C 5sec) Step2: 450°C 15min	50	Liu e al. (1999)
				40	Liu e al. (1998)
				30	Liu e al. (1997)
II	$L1_0$ FePt ~ Fe ₃ Pt	(FePt2.4nm/Fe0.9nm) ₁₆	700°C 1h annealing	16.9	Seki et al. (2005)
	$L1_0$ FePt ~ Fe	FePt/Fe	600°C 10min annealing	21	Rui et al. (2006)
				25	Rui et al. (2007)
	$L1_0$ FePt ~ <i>fcc</i> FePt	Bulk Fe _{0.6} Pt _{0.4}	600°C to 650°C annealing	15	Simizu et al. (2003)
	$L1_0$ FePt ~ Fe ₃ Pt	FePt/Fe	500°C annealing	15.2	Gu et al. (2005)
				16.57	Gu et al. (2006)
	$L1_0$ FePt ~ Fe ₃ Pt	FePt + Fe ₃ O ₄	Ar+5%H ₂ annealing (650°C 1h)	20.1	Zeng et al. (2002)
				18	Zeng et al. (2004)
$L1_0$ FePt ~ Fe ₃ Pt	Bulk FePt + Fe ₃ O ₄	High pressure compaction	16.3	Rong et al. (2007)	
$L1_0$ FePt ~ Fe ₃ Pt	FePt + Fe ₃ Pt particles	Shock compression and 700°C annealing	14	Jin et. al. (2006)	

Table 7.1. A review of $L1_0$ FePt based exchange spring magnets

Group	Exchange couples	Prepared sample	Processing condition	$(BH)_{max}$ (MGOe)	references
III	$L1_0$ FePt \sim fcc FePt	$Fe_{49-x}Co_xPt_{51}$ ($x= 0.0, 0.7, 1.3, 2.2$)	500°C annealing	18.4	Yuan et al. (2007) Yuan et al. (2006) Chen et al. (2005)
	$L1_0$ FePt \sim Fe_3Pt	FePtM (M=Ta, Cr)	600°C annealing	32.1	Chu et al. (2004)
	$L1_0$ FePt \sim fcc FePt	$Fe_{50}Pt_{50-x}Nb_x$ ($x=0.0, 0.83, 1.31, 2.05$)	450~700°C annealing	30.6	Chen et al. (2002)
IV	$L1_0$ FePt \sim Fe_2B	FePt/Fe-B + Co	500°C annealing	15.7	Chang et al. (2008)
	$L1_0$ FePt \sim Fe_2B, Fe_3B	FePtB films	300~500°C annealing	15.0	Sharma et al. (2007)
	$L1_0$ FePt \sim Fe_2B	Melt-spun FePtB	Speed control	14.7	Zhang et al. (2007)

7.2 Experiments

All samples were sputtered onto Si (100) substrates having a surface layer of 200 nm of thermally grown SiO₂ at room temperature. The deposition rate for Pt is 0.31 Å/sec and that for Fe is 0.48 Å/sec. The deposition rate of Fe and Pt was characterized with Rutherford backscattering spectroscopy. All depositions were performed in 4 mTorr of Ar + 3% H₂, and controlled by an automate system.

7.3 Results and discussion

7.3.1 The scale of exchange coupling length

The exchange coupling is basically an interface phenomenon between the hard phase and the soft phase. In this section, the length scale of the coupling is understood with two sets of samples. The first set of $L1_0$ FePt - Fe samples are listed in table 7.2. The $L1_0$ FePt is the stoichiometric $[Fe/Pt]_n$ multilayer sample annealed at 450°C for 30 minutes. Based on previous characterization, a pure ordered $L1_0$ FePt phase was achieved; however, the long-range order parameter is only about 0.7~0.8. The thickness of the $L1_0$ FePt films is about 73 nm. On top of the $L1_0$ FePt sample, a layer of Fe was deposited with thickness as table 7.2.

Table 7.2 A set of samples with varying thickness of Fe deposited on 73 nm $L1_0$ FePt films. The $L1_0$ FePt film was achieved by annealing the stoichiometric $[Fe/Pt]_n$ multilayer samples, “ML_THK_73”, at 450 °C for 30 minutes.

Fe thickness (nm)	1, 2, 3, 4, 5, 6, 7, 8, 9
Bottom layer	73 nm pure layer of ordered $L1_0$ FePt

Figure 7.1 shows the measured magnetic properties of samples. It can be noted from this figure that the samples with Fe layer thinner than 4 nm are well coupled, justified by the fact the M-H loop resembles that of a single magnetic phase. For samples with Fe layer thicker than 4nm, a kink was observed, which indicates that the $L1_0$ FePt is

insufficient to couple the Fe layer, and the Fe layer can be reversed at a lower demagnetizing field.

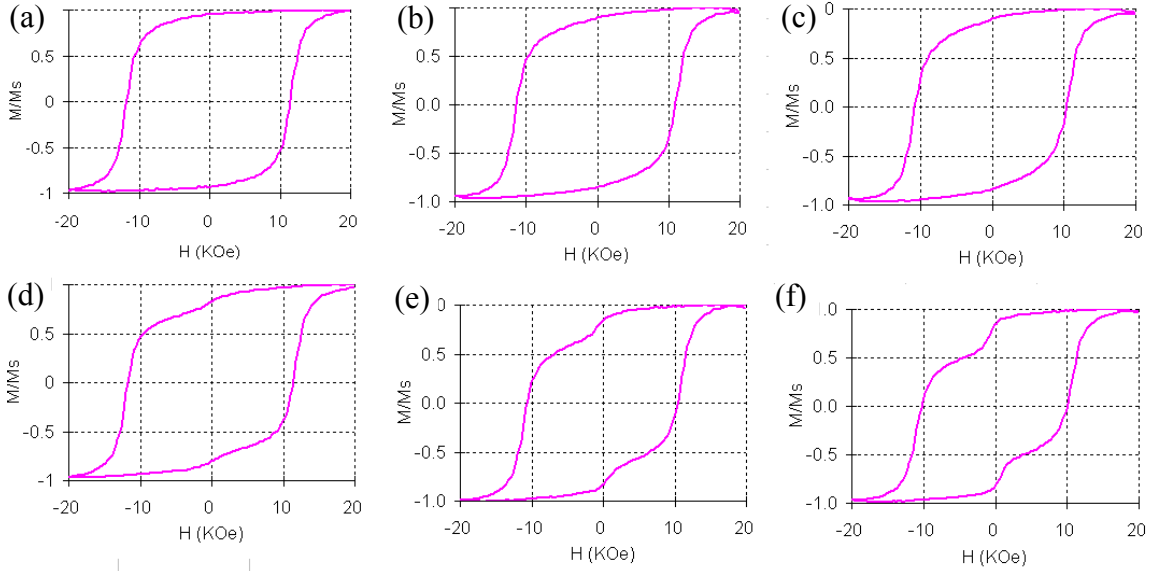


Figure 7.1 M-H loops of samples listed in table 7.2. The Fe thickness (t) was (a) $t=1$ nm; (b) $t=2$ nm; (c) $t=3$ nm; (d) $t=4$ nm; (e) $t=5$ nm; (f) $t=6$ nm. The samples with Fe thicker than 6 nm have similar M-H loops as (f).

The other set of samples are the same Fe layers deposited on highly ordered $L1_0$ FePt films, as shown in table 7.3. These highly ordered $L1_0$ FePt films are the stoichiometric $[\text{Fe}/\text{Pt}]_n$ multilayer films (“ML_THK_73”) annealed at 700°C for 30 minutes. Based on our previous characterization, the long-range order parameter is close to 1. The M-H loops of such $L1_0$ FePt – Fe films were measured and shown in figure 7.2. The curve shown is the minor loop because the instrument used is unable to saturate the sample.

Table 7.3 A set of samples with varying thickness of Fe deposited on highly ordered Ll_0 FePt films. The Ll_0 FePt film was achieved by annealing the stoichiometry $[Fe/Pt]_n$ multilayer samples (“ML_THK_73”) at 700 °C for 30 minutes.

Fe thickness (nm)	1, 2, 3, 4, 5, 6, 7, 8, 9
Bottom layer	73 nm highly ordered Ll_0 FePt

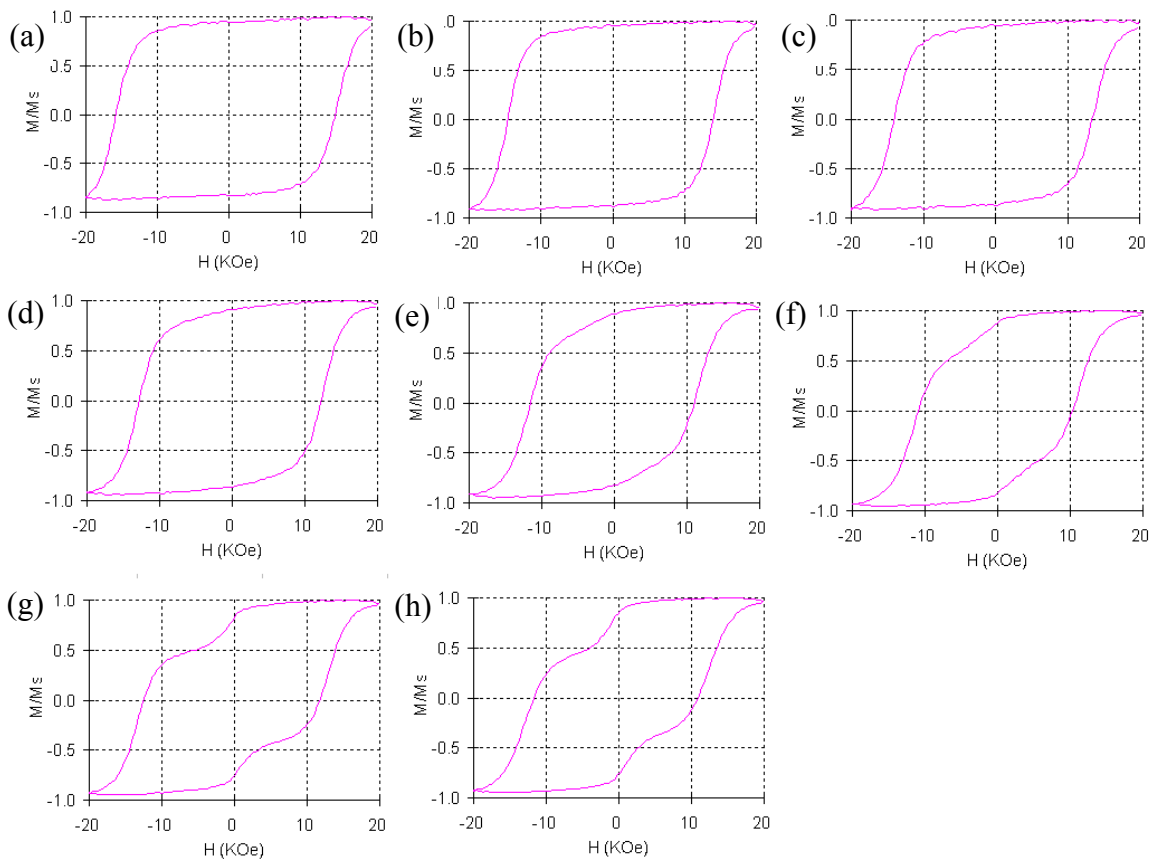


Figure 7.2 M-H of samples listed in table 7.3. The Fe thickness (t) was (a) $t=1$ nm; (b) $t=2$ nm; (c) $t=3$ nm; (d) $t=4$ nm; (e) $t=5$ nm; (f) $t=6$ nm; (g) $t=7$ nm; (h) $t=8$ nm. The samples with Fe thicker than 8 nm have similar M-H loops as (h).

Two interesting phenomena can be observed from Figure 7.2. First, Fe layers thinner than 5 nm are coupled rigidly with the $L1_0$ FePt. The samples with Fe layer of 5 nm and 6 nm show a weak coupling, as demonstrated by the rounded shoulder. For samples with Fe layer thicker than 6 nm, the soft phase can be reversed easily. The other interesting point is the coercivity. Direct examination of H_c of these samples is unavailable because of the limitation of the instrument. However, these minor loops suggest that the H_c of samples with loose or no exchange coupling is lower than those with rigid coupling.

7.3.2 Construction of exchange coupled magnets

[Fe/Pt]_n multilayer films with different composition, as listed in table 7.4, were used to construct the exchanged nanocomposite. The composition of samples was ranged from Fe₅₀Pt₅₀ to Fe₆₈Pt₃₂.

Table 7.4 A list of samples with varying composition

Sample ID	Film structure	Composition	Thickness (nm)
“ML_MGT_50”	[Fe _{3.6nm} Pt _{4.7nm}] ₁₂	Fe _{49.5} Pt _{50.5}	100
“ML_MGT_56”	[Fe _{4.5nm} Pt _{4.6nm}] ₆	Fe _{55.6} Pt _{44.4}	55
“ML_MGT_59”	[Fe _{4.6nm} Pt _{4.2nm}] ₁₂	Fe _{58.5} Pt _{41.5}	105
“ML_MGT_61”	[Fe _{5.5nm} Pt _{4.5nm}] ₆	Fe _{60.9} Pt _{39.1}	60
“ML_MGT_68”	[Fe _{7.3nm} Pt _{4.4nm}] ₆	Fe _{67.9} Pt _{32.1}	70

As is well understood, pure *L1₀* phase FePt has a high anisotropy energy, but its $(BH)_{max}$ is limited by saturation magnetization. Figure 7.3 shows the M-H loop of sample “ML_MGT_50” in the as-deposited condition and annealed at 400°C for 1 hour. The as-deposited sample has a M_s of 850 emu/cc, while the annealed one has a M_s of 609 emu/cc. For polycrystalline *L1₀* FePt films, a maximum $(BH)_{max}$ limit of 13MGOe is widely reported. The polycrystalline film generally has a lower energy product than that of the single crystalline films measured along the easy axis. The M_s difference of disordered *fcc* FePt and *L1₀* FePt suggests that the *fcc-L1₀* exchange coupled magnet can increase the product.

The red dot in Figure 7.3 (b) shows the position of $(BH)_{max}$, 11.5 MGOe. This position also indicates that the energy product of *L1₀* FePt phase is limited by the M_s .

Further increase of the coercivity does not help for the increase of the $(BH)_{max}$. It can also be seen that the M at the red spot slightly drops from 609 emu/cc (M_s) to 542 emu/cc, while the $(BH)_{max}$ decreased from the limit of 14.6 MGOe to 11.5 MGOe. The reason is the $(BH)_{max}$ is generally proportional to M^2 provided that the coercivity is high enough, therefore, slight change of M may result in a big different of $(BH)_{max}$.

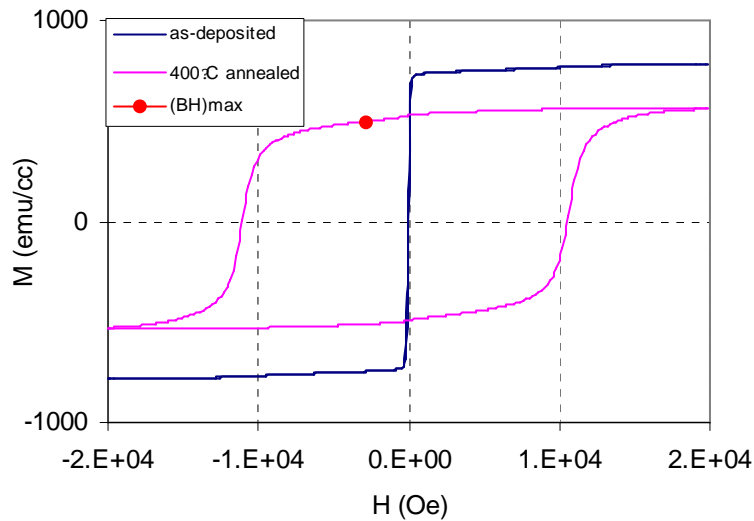


Figure 7.3 The M-H loops of as-deposited and 400°C annealed sample “ML_MGT_50”. The red dot in the figure indicates the position of the $(BH)_{max}$.

Two different processing approaches are needed for samples with different compositions. For high temperature annealed samples with a composition close to stoichiometric $Fe_{50}Pt_{50}$, the threshold to acquire large energy product is usually limited by the magnetization, while the coercivity is more than necessary. Therefore, a lower annealing temperature is desirable so that the annealed film is a mixture of disordered *fcc* FePt and ordered $L1_0$ FePt. As demonstrated, the *fcc* FePt phase has a higher saturation

magnetization than the ordered $L1_0$ FePt phase. For samples with a much higher Fe concentration, the saturation magnetization is not the threshold. Instead, it is difficult to achieve the ordered phase. The coercivity of annealed film is usually very low, which prevents the achievement of high energy product magnets.

The sample with the stoichiometric composition, “ML_MGT_50”, was annealed at 300°C and 350°C for 1 hour, and 400°C for 15 minutes. The measured results were compared with the sample annealed at 400°C for one hour, which was assumed to be pure $L1_0$ FePt phase based on previous characterization. The lower annealing temperatures or short annealing time are applied to achieve a mixture of fcc FePt phase and ordered $L1_0$ FePt phase. Figure 7.4 shows the M-H hysteresis loop of annealed samples at these conditions. Table 7.5 gives a summary of the M, H at the $(BH)_{max}$ position.

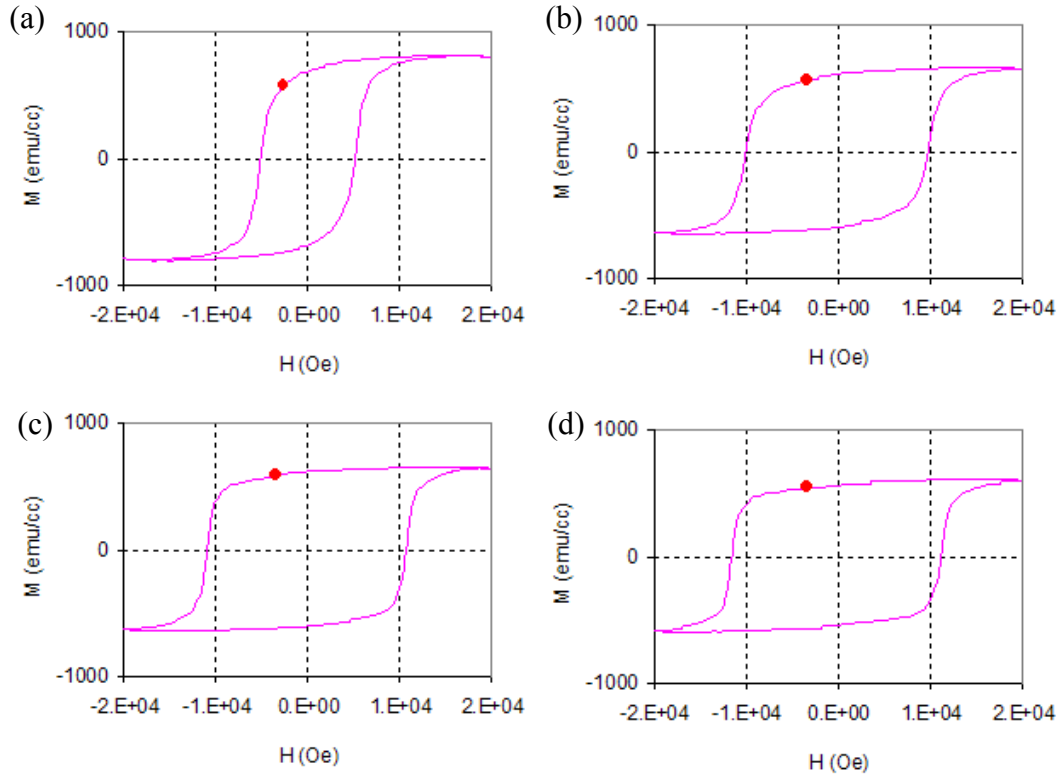


Figure 7.4 The M-H hysteresis loops of sample “ML_MGT_50” annealed at (a) 300°C for 1 hour, (b) 350°C for 1 hour, (c) 400°C for 15 minutes, and (d) 400°C for 60 minutes.

The red spots on the curve shows the position of $(BH)_{max}$.

Table 7.5 A summary of magnetic properties of sample “ML_MGT_50” annealed at different conditions.

Annealing condition	M, M_s (emu/cc)	H, H_c (kOe)	$(BH)_{max}$ (MGOe)	Threshold
300°C, 1 hour	566, 810	2.59, 5.38	11.7	H limited
350°C, 1 hour	560, 659	3.39, 10.2	12.3	M limited
400°C, 15minutes	579, 647	3.39, 11.0	13.2	M limited
400°C, 1 hour	542, 600	3.39, 11.3	11.5	M limited

The results shown above indicate that a lower annealing temperature or shorter annealing time is helpful to increase the $(BH)_{max}$ of the annealed films. The main advantage of this approach is the lower processing temperature and short annealing time, which are highly desirable for some applications as magnetic MEMS films, for example.

The influence of Fe concentration can be clearly demonstrated with Figure 7.5, the M-H hysteresis loops of samples “ML_MGT_56”, “ML_MGT_59”, “ML_MGT_61”, and “ML_MGT_68” annealed at 400 °C for 1 hour. The saturation magnetization increases steadily with the increase of Fe concentration. The H_c , however, changes in the reverse direction, as expected. This trend was the same for samples annealed at different annealing conditions (examined temperature varying from 300°C to 600°C and time varying from 15 minutes to 4 hours). Because the energy product of annealed film was determined by the coercivity, magnetic moment, as well as the shape of the loop.

Therefore, it is expected that a balance of coercivity and magnetization can be achieved to maximize the energy product.

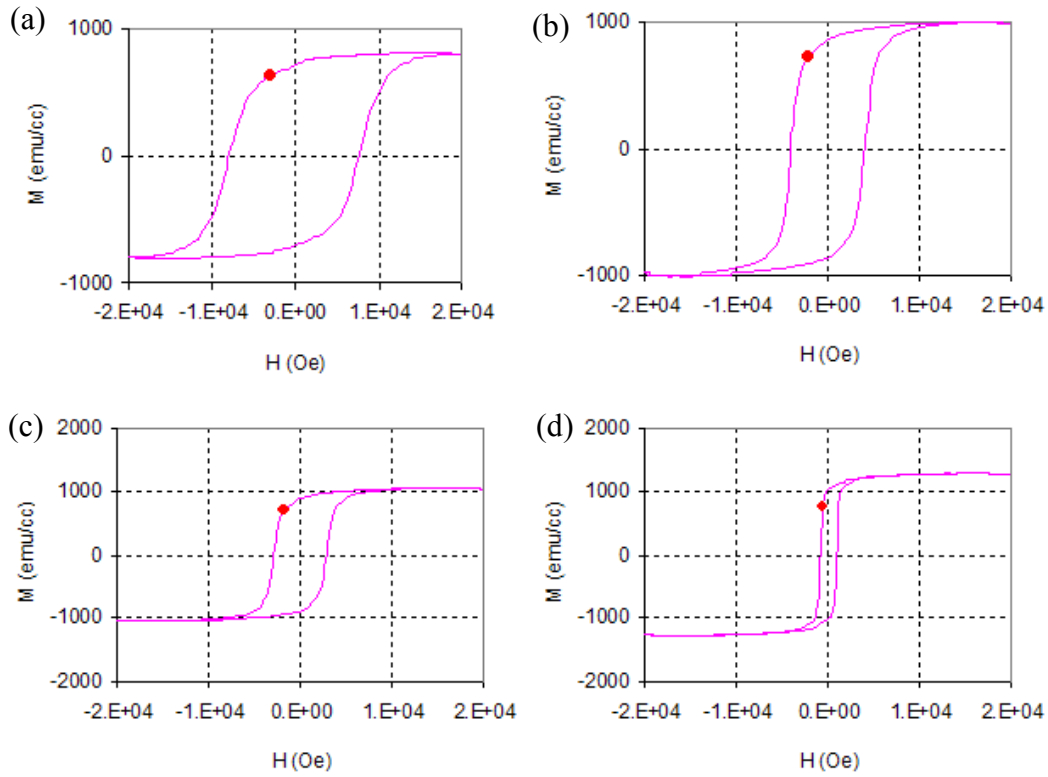


Figure 7.5. The M-H hysteresis loops of sample (a) “ML_MGT_56”; (b) “ML_MGT_59”; (c) “ML_MGT_61”; and (d) “ML_MGT_68” annealed at 400°C for 60 minutes. The red spots on the curve shows the position of $(BH)_{max}$.

Table 7.6, 7.7, and 7.8 shows the saturation magnetization, coercivity, and the energy product of samples annealed at different conditions, respectively. The M_s and H_c generally follow a simple trend. For each sample, the decreases of magnetization, and the increases of coercivity are observed with the increase of annealing temperature. At

the same annealing condition, the M_s increases, and H_c decreases with the increase of Fe concentration.

Table 7.6 The saturation magnetization (emu/cc) of annealed samples

Sample	300°C 1h	350°C 1h	400°C *	500°C 15min	600°C 15min
“ML_MGT_50”	810	656	600	N/A	N/A
“ML_MGT_56”	950	844	828	659	623
“ML_MGT_59”	1053	1040	968	869	770
“ML_MGT_61”	1080	1010	1089	900	843
“ML_MGT_68”	1315	1231	1283	1284	1352

*: the annealing time is different form different samples, varying from 15minutes to one hour. The one with highest $(BH)_{max}$ was put in the table.

Table 7.7 The coercivity (kOe) of annealed samples

Sample	300°C 1h	350°C 1h	400°C *	500°C 15min	600°C 15min
“ML_MGT_50”	5.38	10.2	11.3	N/A	N/A
“ML_MGT_56”	3.79	4.98	6.97	9.36	11
“ML_MGT_59”	2.59	2.99	4.98	6.57	6.17
“ML_MGT_61”	1.4	2.59	2.99	4.58	4.58
“ML_MGT_68”	0.2	0.602	1	0.6	0.6

*: the annealing time is different form different samples, varying from 15minutes to one hour. The one with highest $(BH)_{max}$ was put in the table.

Table 7.8 The energy product (MGOe) of annealed samples

Sample	300°C 1h	350°C 1h	400°C *	500°C 15min	600°C 15min
“ML_MGT_50”	11.7	12.3	11.5	N/A	N/A
“ML_MGT_56”	12.2	13.3	14.7	12.5	12.6
“ML_MGT_59”	11.8	12.8	16	16.7	14.9
“ML_MGT_61”	4.77	11.3	13.3	12.4	11.2
“ML_MGT_68”	N/A	2.52	6.32	2.44	4.68

*: the annealing time is different form different samples, varying from 15minutes to one hour. The one with highest $(BH)_{max}$ was put in the table.

The trends of M_s and H_c with the annealing condition and Fe concentration determines peak position of $(BH)_{max}$, as shown in table 7.8. For samples with composition close to stoichiometry $L1_0$ FePt, the magnetization is limited, and the coercivity is higher than desirable. Consequently, a relatively lower annealing temperature, thus corresponding to a mixture of fcc FePt and $L1_0$ FePt, is more beneficial for higher energy product. “ML_MGT_50” and “ML_MGT_56” are the examples in this group. For samples with higher Fe concentration, the achievement of higher energy product is mainly limited by its relatively lower coercivity. For these samples, a relatively higher annealing temperature is needed to increase the ordering of $L1_0$ FePt phase. Too high annealing temperature, however, is not helpful to increase the energy product, as shown above. Sample “ML_MGT_59” and “ML_MGT_61” are examples in this group.

7.4 Conclusions

The exchange spring coupling length was experimentally characterized to be limited within several nanometers at the interface. A higher ordering of the hard phase is helpful to increase the length scale slightly.

The energy product of sample with varying annealing condition and composition was examined in this chapter. It was found that for samples with composition close to stoichiometric Ll_0 FePt, a lower processing temperature is beneficial to increase the energy product. The reason is that higher energy product is limited by the average saturation magnetization, and a lower processing temperature gives a larger fraction of disordered phase, and increases the M_s of annealed samples.

For sample with higher Fe concentration, a relatively higher annealing temperature was found to be beneficial to increase the ordering and coercivity, and thus to increase the energy product. The reason is that $(BH)_{max}$ is limited by the low coercivity of annealed sample with higher Fe concentration.

CHAPTER 8 SUMMARY

8.1 Conclusions

The transmission electron microscopy study of the annealed multilayers indicates that the Pt layer grows at the expense of Fe during annealing forming a disordered *fcc* FePt phase by interdiffusion of Fe into Pt. This thickening of the *fcc* Pt layer can be attributed to the higher solubilities of Fe into *fcc* Pt, as compared to the converse. For the range of film thickness studied, a continuous $L1_0$ FePt product layer, which then thickens with further annealing, is not found. Instead, the initial $L1_0$ FePt grains are scattered mainly on the grain boundaries within the *fcc* FePt layer and at the Fe/Pt interfaces and further transformation of the sample to the ordered $L1_0$ FePt phase proceeds coupled with the growth of the initial $L1_0$ FePt grains.

A more comprehensive study of annealed $[\text{Fe/Pt}]_n$ films is provided concerning the phase fraction, grain size, nucleation/grain density, interdiffusivity, long-range order parameter, and magnetic properties. A method based on hollow cone dark field TEM is introduced to measure the volume fraction, grain size, and density of ordered $L1_0$ FePt phase grains in the annealed films, and a model based on low-angle X-ray diffraction is used to measure the effective Fe-Pt interdiffusivity.

The process-structure-properties relations of two groups of samples with varying substrate temperature and periodicity are reported. The results demonstrate that the processing parameters (substrate temperature, periodicity) have a strong influence on the structure (effective interdiffusivity, $L1_0$ phase volume fraction, grain size and density) and magnetic properties. The correlation of these parameters suggests that the annealed

[Fe/Pt]_n multilayer films have limited nuclei, and the following growth of LI_0 phase is very important to the extent of ordered phase formed. A correlation between the grain size of *fcc* FePt phase and the LI_0 FePt phase fraction (or magnetic properties) strongly suggests that the phase transformation of $fcc \rightarrow LI_0$ is highly dependent on the grain size of the parent *fcc* FePt phase. It is explained based on a much higher (several order) growth rate of some special incoherent interfaces compared to other interfaces.

An investigation of the influence of total film thickness on the phase formation of LI_0 FePt phase in [Fe/Pt]_n multilayer films and a comparison to that of FePt co-deposited alloy films is also conducted. A general trend of better LI_0 phase formation in thicker films was observed in both types of films. It was further found that the thickness dependence of the structure and of the magnetic properties in [Fe/Pt]_n multilayer films is much stronger than that in FePt alloy films. This may be related to the higher chemical energy contained in [Fe/Pt]_n films than FePt alloy films, which is helpful for the *fcc* FePt grain growth and LI_0 FePt phase growth. However, the initial nucleation temperature of [Fe/Pt]_n multilayers and co-deposited alloy films was found to be similar.

An investigation of LI_0 FePt-based exchange spring magnets is presented based on our understanding of the LI_0 formation in [Fe/Pt]_n multilayer films. It is known that exchange coupling is an interfacial magnetic interaction and it was experimentally shown that this interaction is limited to within several nanometers of the interface. A higher degree of order of the hard phase is helpful to increase the length scale slightly. Two approaches can be used to construct the magnets. For samples with composition close to stoichiometric LI_0 FePt, the achievement of higher energy product is limited by the average saturation magnetization, and therefore, a lower annealing temperature is

beneficial to increase the energy product, which gives a larger fraction of disordered phase. For sample with higher Fe concentration, the $(BH)_{max}$ is limited by the low coercivity of annealed sample. A relatively high annealing temperature is beneficial to increase the ordering and coercivity, and thus to increase the energy product.

8.2 Future work

This dissertation demonstrates that the LI_0 FePt phase can be achieved at low processing temperature in thicker films. The need for future work and discovery to provide enhanced LI_0 phase nucleation for magnetic recording applications is quite clear. For thin film magnetic recording, a very thin film (< 10 nm) is required. Formation of highly textured LI_0 FePt films with perpendicular anisotropy through heat treatment of $[\text{Fe}/\text{Pt}]_n$ multilayer films is also needed, as required for their applications. It has been reported that the epitaxial $[\text{Fe}/\text{Pt}]_n$ or FePt films can be formed by using the MgO and Al_2O_3 substrates. Further study on the nucleation and growth of LI_0 FePt in the epitaxial or highly textured $[\text{Fe}/\text{Pt}]_n$ films on these substrates will also be very interesting.

Severe plastic deformation might be one way to construct LI_0 FePt based exchange spring magnets in bulk forms. Severe plastic deformation is one way to prepare multilayer materials, where each layer can be as thin as several nanometers. This method might be an ideal approach to construct LI_0 FePt based exchange spring magnets. For example, a thick highly ordered LI_0 FePt film and Fe film (i.e., several μm) can be prepared separately. Through severe plastic deformation, the $[\text{Fe}/\text{FePt}]_n$ multilayers can be formed. The layer thickness is controlled by the number of repeating folding followed by the plastic deformation. One problem is how to apply these plastic deformed materials. The LI_0 FePt based exchange spring magnets mainly focus on the film applications, while the severe plastic deformation is more appropriate to prepare bulk form of multilayers.

On the general thin film multilayer reactions, it is interesting to understand if the process-structure-properties relations and the selective phase growth model can be applied to other material systems.

**APPENDIX A THEORY OF EFFECTIVE INTERDIFFUSIVITY OF
MULTILAYER FILMS THROUGH XRD**

The model used in this thesis to measure the interdiffusivity of multilayer films is based on the pioneering study on the free energy of the spinodal decomposition. The homogenization of multilayer films during annealing is the reverse process of the spinodal decomposition. It is well known that the solution for spinodal decomposition composes of local composition fluctuation. This local composition fluctuation gives an additional local composition gradient and interface strain compared to an isotropic solid solution or macroscale diffusion couple. Specifically, the total free energy of a material with compositional fluctuation can be expressed as Equation (A.1).

$$F = \int_V \left[f'(c) + k(\nabla c)^2 + \frac{\eta^2 E}{1-\nu} (c - c_0)^2 \right] dV \quad (\text{A.1})$$

Where F is the total Helmholtz free energy, f' is the Helmholtz free energy of a unit volume of homogeneous material of composition C_0 , k is the coefficient to represent the influence of steep compositional gradients on the free energy, $k(\nabla c)^2$ is the increase in free energy due to introduced compositional gradient, $\eta = d\ln(a)/dc$ (a is the lattice parameter, and c is the local composition), E is the Young's modulus, ν is the Poisson's ratio, and $\frac{\eta^2 E}{1-\nu} (c - c_0)^2$ is the increase in free energy due to interface coherent strain.

Details on the derivation of this expression can be found in the reference [Cahn, (1961, 1962, 1966); Cook et al., (1969); Philofsky et al., (1969)].

From equation (A.1), for a presence of local change in composition or coherent strain, the change of total free energy in the solution can be expressed as:

$$\delta F = \int_V \left[f'' + \frac{2\eta^2 E}{1-\nu} (c - c_0) - \frac{\partial k}{\partial c} (\nabla c)^2 - 2k\nabla^2 c \right] \delta c dV$$

The quantity in brackets is the change in free energy due to a local change of composition δc . The net flux of atoms can then be given through the change of free energy.

$$J = -M \cdot \text{grad} \left[f'' + \frac{2\eta^2 E}{1-\nu} (c - c_0) - \frac{\partial k}{\partial c} (\nabla c)^2 - 2k \nabla^2 c \right]$$

and

$$- \text{div} J = \frac{\partial c}{\partial t} = \text{div} \left\{ M \cdot \text{grad} \left[f'' + \frac{2\eta^2 E}{1-\nu} (c - c_0) - \frac{\partial k}{\partial c} (\nabla c)^2 - 2k \nabla^2 c \right] \right\}$$

If the terms not linear in c are neglected, a simplified expression is obtained.

$$\frac{\partial c}{\partial t} = M \cdot \left(f'' + \frac{2\eta^2 E}{1-\nu} - 2k \nabla^2 c \right) \nabla^2 c$$

Here M is defined as mobility, and has the expression:

$$M = \tilde{D}_0 / f''$$

\tilde{D}_0 is defined as the interdiffusivity of bulk diffusion couples. Therefore, the above expression can be rewritten as:

$$\frac{\partial c}{\partial t} = \tilde{D}_0 \cdot \left(1 + \frac{2\eta^2 E}{(1-\nu)f''} - \frac{2k \nabla^2 c}{f''} \right) \nabla^2 c \quad (\text{A.2})$$

Compared to the commonly used Fick's law,

$$\frac{\partial c}{\partial t} = \tilde{D}_0 \nabla^2 c$$

The effective interdiffusivity (D_Λ) in the solution with compositional fluctuation is defined as:

$$D_{\Lambda} = \tilde{D}_0 \cdot \left(1 + \frac{2\eta^2 E}{(1-\nu)f''} - \frac{2k\nabla^2 c}{f''} \right)$$

At the early stage of Spinodal decomposition or later stages of thermal annealing of multilayers, the compositional modulations are expected to be small. In this case, Eq. (A.2) has the discrete solution:

$$c(p, t) = A(t) \cos \left[\frac{2\pi x(p)}{\lambda} \right]$$

where $A(t)$ is the amplitude of composition modulation at time t , λ is the wavelength and $x(p)$ is the distance of the p th plane from the origin. In term of the amplitude at time zero:

$$A(t) = A(0) \exp[-D_{\Lambda} B^2(\lambda)t]$$

In which

$$B^2(\lambda) = \left(\frac{2\pi}{\lambda} \right)^2 - \left(\frac{d^2}{12} \right) \left(\frac{2\pi}{\lambda} \right)^4 + \dots$$

In the kinematic approximation the integrated intensity $I(t)$ of the first Bragg small angle peak near the direct beam is proportional to the square of the amplitude $A(t)$.

$$I(t) \sim |A(t)|^2$$

Based on above equation:

$$I(t) = I(0) \exp[-2D_{\Lambda} B^2(\Lambda)t] \quad , \text{ or}$$

$$D_{\Lambda} = -\frac{1}{2B^2(\Lambda)} \ln \left(\frac{I(t)}{I(0)} \right)$$

Which is the equation widely used to measure the interdiffusivity in multilayer films.

**APPENDIX B TEM DIFFRACTION INTENSITY EVALUATION OF
FCC AND $L1_0$ FePt PHASES**

The diffraction intensity in TEM is different from that of XRD. The calculation is usually difficult and involves the simulations. In this thesis, a simplified estimation is applied to compare the intensities of different reflections, based on the solution of Howie-Whelan equations [[Williams et al., \(1996\)](#)].

The Howie-Whelan equations, Equation B.1 and B.2, are usually used to understand the diffraction intensity. The column approximation is applied for the analysis.

$$\frac{d\phi_g}{dz} = \frac{\pi i}{\xi_g} \phi_0 e^{-2\pi i s z} + \frac{\pi i}{\xi_0} \phi_g \quad (\text{B.1})$$

$$\frac{d\phi_0}{dz} = \frac{\pi i}{\xi_g} \phi_g e^{2\pi i s z} + \frac{\pi i}{\xi_0} \phi_0 \quad (\text{B.2})$$

where ϕ_g is the amplitude of diffracted beam, ϕ_0 is that of the direct beam, ξ_g and ξ_0 is the extinction distance for the diffracted beam and direct beam respectively, s is called excitation error, z is the distance along the optic axis.

Above equations can be solved to give the intensity expression of ϕ_g .

$$|\phi_g|^2 = \left(\frac{\pi t}{\xi_g} \right)^2 \frac{\sin^2(\pi S_{eff})}{(\pi S_{eff})^2} \quad (\text{B.3})$$

where t is the film thickness, and S_{eff} is defined as the effective excitation error.

$$S_{eff} = \sqrt{s^2 + \frac{1}{\xi_g^2}}$$

To compare the intensity of diffracted beam, we can simply assume the excitation error (s) to be zero. Then from equation (B.3) we can write.

$$I = |\phi_g|^2 = \sin^2 \left(\frac{\pi t}{\xi_g} \right) \quad (\text{B.4})$$

The calculation of ξ_g is needed in order to calculate the intensity of ϕ_g . From the reference, ξ_g can be expressed as

$$\xi_g = \frac{\pi V_c \cos \theta_B}{\lambda F_g} \quad (\text{B.5})$$

where V_c is the volume of a unit cell, θ_B is the Bragg angle, λ is the wavelength of electron beams, and F_g is the structure factor. All terms in the expression, except F_g , can be easily achieved. The structure factor F_{hkl} (hkl as the index of g) is defined as

$$F_{hkl} = \sum_i f_i e^{2\pi i(hx_i + ky_i + lz_i)} \quad (\text{B.6})$$

where x_i , y_i , z_i is the atomic position of i -th atom in the unit-cell, and f_i is the atomic scattering factor for electron beams. The same expression is also commonly used to calculate the structure factor of XRD. The atomic scattering factor, f_i , is a measure of the amplitude of an electron wave scattered from an isolated atom, which is a fundamental result of the wave nature of the electron. The value of f_i , unfortunately, is still hard to be determined precisely. One approximation to define the f_i is expressed as Equation (B.7).

$$f_i(\theta) = \frac{m_0 e^2}{2h} \left(\frac{\lambda}{\sin \frac{\theta}{2}} \right)^2 (Z - f_x) = 2.38 \times 10^{-10} \left(\frac{\lambda}{\sin \frac{\theta}{2}} \right)^2 (Z - f_x)(\text{cm}) \quad (\text{B.7})$$

where λ is the wavelength (0.00197 nm for 300KeV), Z is the atomic number, f_x is the scattering factors for X-rays, $\theta/2$ is the scattering angle.

From equations B.4 to B.7, the intensity of diffracted beams can be calculated for FePt, as listed in table B.1. The film thickness is set to 10 nm. Other terms are well

known. From the table, it is very clear that the diffracted beam intensity for 201_{L10} and 112_{L10} are much lower than that of the rest of diffracted beams in the table, especially for sample with a lower long range order parameter ($S=0.8$).

Table B.1. The intensity evaluation of diffraction beams.

hkl	$f_x(\text{Fe})$	$f_x(\text{Pt})$	$\sin(\theta)$	$f_i(\text{Fe})$ (Å)	$f_i(\text{Pt})$ (Å)	F_{hkl} (Å)	ξ_g (Å)	I (%) (S=1)	I (%) (S=0.8)	I (%) (S=0.7)
0 0 1	21.6	62.1	2.7E-03	5.72	20.77	30.1	286.89	79.0	50.6	48.1
1 1 0	19.6	58.3	3.7E-03	4.54	13.94	18.8	459.32	39.9	25.6	21.2
1 1 1	18.0	55.0	4.6E-03	3.68	10.58	28.5	302.69	74.2	74.2	74.2
2 0 0	16.9	52.6	5.2E-03	3.21	8.97	24.3	354.73	60.0	60.0	60.0
0 0 2	16.6	52.0	5.4E-03	3.07	8.53	23.2	372.07	55.9	55.9	55.9
2 0 1	15.8	50.2	5.9E-03	2.83	7.73	9.8	880.98	12.2	7.8	6.1
1 1 2	15.0	48.0	6.5E-03	2.46	6.71	8.5	1015.64	9.3	5.9	4.6
2 2 0	14.1	45.3	7.3E-03	2.11	5.76	15.7	548.67	29.4	29.4	29.4
2 0 2	13.9	44.9	7.5E-03	2.06	5.63	15.4	561.62	28.2	28.2	28.2

LIST OF REFERENCES

- Aaronson H. I., and Kinsman K. R. (1977), Growth mechanisms of gold-copper II plates, *Acta Metallurgica*. 25, 367.
- Aubertine D. B., Ozguveen N., McIntyre P. C., and Brennan S. (2003), Analysis of x-ray diffraction as a probe of interdiffusion in Si/SiGe heterostructures, *Journal of Applied Physics*. 94, 1557.
- Avrami M. (1939), Kinetics of phase change. I. General theory, *Journal of Chemical Physics*. 7, 1103.
- Avrami M. (1940), Kinetics of phase change. II. Transformation-time relations for random distribution of nuclei, *Journal of Chemical Physics*. 8, 212.
- Avrami M. (1941), Granulation, phase change and microstructure. Kinetics of phase change. III, *Journal of Chemical Physics*. 9, 177.
- Balluffi R. W., Allen S. M., Carter W. C., *Kinetics of Materials* (J. Wiley, New York, 2005), p. 537~538.
- Barmak K., Ristau R. A., Coffey K. R., Parker M. A., and Howard J. K. (1996), Grain growth and ordering kinetics in CoPt thin films, *Journal of Applied Physics*. 79, 5330.
- Barmak K.; Kim J.; Berry D. C.; Wierman K. W.; Svedberg, E. B.; Howard, J. K. (2004), Calorimetric studies of the A1 to L1₀ transformation in FePt and related ternary alloy thin films, *Journal of Applied Physics*. 95, 7486.
- Barmak K., Coffey K. R., Rudman D. A., and Foner S. (1990), Phase formation sequence for the reaction of multilayer thin films of niobium/aluminum, *Journal of Applied Physics*. 67, 7313.

- Barmak K., Kim J., Lewis L. H., Coffey K. R., Toney M. F., Kellock A. J., and Thiele, J.-U. (2005), On the relationship of magnetocrystalline anisotropy and stoichiometry in epitaxial L_{10} CoPt (001) and FePt (001) thin films, *Journal of Applied Physics*. 98, 033904/1.
- Barmak K., Coffey K. R., Rudman D. A., Foner S. (1992), Effects of microstructure on phase formation in the reaction of niobium/aluminum multilayer thin films, *Materials Research Society Symposium Proceedings*, 230, 61.
- Berry D. C., Ultrahigh density magnetic recording media: The A1 to L_{10} phase transformation in FePt and related ternary alloys (Carnegie Mellon University dissertation, Pittsburgh, 2007).
- Berry D.C., Kim j., Barmak K., Wierman K., Svedberg E. B., and Howard J. K. (2005), Differential scanning calorimetry studies of the effect of Cu on the A1 to L_{10} transformation in FePt thin films, *Scripta Materialia*. 53, 423.
- Berry D. C., and Barmak K. (2007), Time-temperature-transformation diagrams for the A1 to L_{10} phase transformation in FePt and FeCuPt thin films, *Journal of Applied Physics*. 101, 014905/1.
- Bian B., Laughlin D. E., Sato K., and Hirotsu Y. (2000), Fabrication and nanostructure of oriented FePt particles, *Journal of Applied Physics*. 87, 6962.
- Bollero A., Gutfleisch O., Muller K. H., Schultz L., and Drazic G. (2002), High-performance nanocrystalline PrFeB-based magnets produced by intensive milling, *Journal of Applied Physics*. 91, 8159.

- Brown G., Kraczek B., Janotti A., Schulthess T. C., Stocks G. M., and Johnson, D. D. (2003), Competition between ferromagnetism and antiferromagnetism in FePt, *Physical Review B: Condensed Matter and Materials Physics*. 68, 052405/1.
- Brown W. Jr. (1979), Thermal fluctuation of fine ferromagnetic particles, *IEEE Transactions on Magnetics*. 15, 1196.
- Burkert T., Eriksson O., Simak S. I., Ruban A. V., Sanyal B., Nordstrom L., and Wills J. M. (2005), Magnetic anisotropy of L₁₀ FePt and Fe_{1-x}Mn_xPt, *Physical Review B: Condensed Matter and Materials Physics*. 71, 134411/1.
- Cahn J. W. (1961), Spinodal composition, *Acta Metallurgica*. 9, 795.
- Cahn J. W. (1962), Spinodal decomposition in cubic crystals, *Acta Metallurgica*. 10, 179.
- Cahn J. W., Hilliard J. E. (1959), Free energy of a nonuniform system. III. Nucleation in a two-component incompressible fluid, *Journal of Chemical Physics*. 31, 688.
- Cahn, J. W. (1966), Later stages of spinodal decomposition and the beginnings of particle coarsening, *Acta Metallurgica*, 14, 1685.
- Cantelli V., von Borany J., Muecklich A., Zhou S., and Grenzer J. (2007), Influence of energetic ions and neutral atoms on the L₁₀ ordering of FePt films, *Nuclear Instruments & Methods in Physics Research, Section B: Beam Interactions with Materials and Atoms*. 257, 406.
- Chang L, Giessen BC, In synthetic modulated structures (Academic Press, New York, 985).
- Chang C. W., Chang H. W., Chiu C. H., Hsieh C. C., Fang Y. K., and Chang W. C. (2008), Magnetic property improvement of Pt-lean FePt /Fe-B-type nanocomposites by Co substitution, *Journal of Applied Physics*. 103, 07E133/1.

- Chen S. K., Hsiao S. N., Yuan F. T., and Chang, W. C. (2005), Magnetic property enhancement of Fe_{49-x}CoxPt₅₁ (x = 0.0, 0.7, 1.3, 2.2) thin films, *IEEE Transactions on Magnetics*. 41, 3784.
- Chen S. K., Yuan F. T., Chang W. C., and Chin Tsung-Shune (2002), Magnetic properties of FePt and Fe₅₀Pt_{50-x}Nbx (x = 0.00, 0.83, 1.31, 2.05) thin films, *Journal of Magnetism and Magnetic Materials*. 239, 471.
- Chen S. K., Yuan F. T., Hsiao S. N., Chang H. C., Liou C. Y., and Chang W. C. (2004), Thickness dependence of longitudinal coercivity in Fe–Pt–Al thin films, *Journal of Magnetism and Magnetic Materials*. 282, 198.
- Chou S. C., Yu C. C., Liou Y., Yao Y. D., Wei D. H., Chin T. S., and Tai M. F. (2004), Annealing effect on the Fe/Pt multilayers grown on Al₂O₃ (001) substrates, *Journal of applied physics*. 95, 7276.
- Chou S. C., Yu C. C., Liou Y., and Yao Y. D. (2004), Bilayers thickness effect on the magnetic properties of [Fe/Pt]_n films, *Physics of the Solid State (a)*. 201, 1755.
- Christian J. W., *The Theory of Transformations in Metals and Alloys*, 2nd ed. (Pergamon Press, New York, 1975), p. 1, 8, 9, 19, 479.
- Chu J. P., Mahalingam T., and Wang S. F. (2004), The structure and magnetic properties of sputtered FePtM (M = Ta, Cr) thin films, *Journal of Physics: Condensed Matter*. 16, 561.
- Coehoorn R., De Mooij D. B., De Waard C. (1989), Meltspun permanent magnet materials containing iron boride (Fe₃B) as the main phase, *Journal of Magnetism and Magnetic Materials*, 80, 101.
- Coey, J.M.D. (1997), Permanent magnetism, *Solid State Communications*. 102, 101.

- Coey J. M. D. (2002), Permanent magnet applications, *Journal of Magnetism and Magnetic Materials*. 248, 441.
- Coffey K. R., Dissertation: thin film reaction kinetics in multilayers of niobium/aluminum (Massachusetts Institute of Technology, Cambridge, Massachusetts, 1989).
- Coffey Kevin R., Parker M. A., and Howard J. K. (1995), High anisotropy L1₀ thin films for longitudinal recording, *IEEE Transactions on Magnetics*. 31, 2737.
- Coffey K. R., Barmak K., Rudman D. A., and Foner S. (1992), First phase formation kinetics in the reaction of niobium/aluminum, *Materials Research Society Symposium Proceedings*. 230, 55.
- Coffey K. R., Barmak K., Rudman D. A., and Foner S. (1992), Thin film reaction kinetics of niobium/aluminum multilayers, *Journal of Applied Physics*. 72, 1341.
- Cook H. E., and Hilliard J. E. (1969), Effect of gradient energy on diffusion in gold-silver alloys, *Journal of Applied Physics*. 40, 2191.
- Ding J., Liu Y., Street R., and McCormick P. G. (1994), High magnetic performance in isotropic α -Fe+Sm₂Fe₁₇N_x, *Journal of Applied Physics*. 75, 1032.
- Ding J., Liu Y., McCormick P. G., and Street R. (1993), Remanence enhancement in isotropic samarium-cobalt powders, *Journal of Magnetism and Magnetic Materials*. 123, L239.
- Ding Y., and Majetich S. A. (2006), Nucleation site density study of the L10 phase transformation in FePt nanoparticles, *Journal of Applied Physics*. 99, 08G701/1.
- Endo Y., Kikuchi N., Kitakami O. and Shimada Y. (2001), Lowering of ordering temperature for fct Fe-Pt in Fe/Pt multilayers, *Journal of Applied Physics*. 89, 7065.

- Endo Y., Oikawa K., Miyazaki T., Kitakami O., and Shimada Y. (2003), Study of the low temperature ordering of L1₀-Fe-Pt in Fe/Pt multilayers, *Journal of Applied Physics*. 94, 7222.
- Farrow R. F. C., Weller D., Marks R. F., Toney M. F., Cebollada A., and Harp G. R. (1996), Control of the axis of chemical ordering and magnetic anisotropy in epitaxial FePt films, *Journal of Applied Physics*. 79, 5967.
- Fidler J., Schrefl T., Hoefinger S., Hajduga M. (2004), Recent developments in hard magnetic bulk materials, *Journal of Physics: Condensed Matter*. 16, S455.
- Fleming R. M., McWhan D. B., Gossard A. C., Wiegmann W., and Logan R. A. (1980), X-ray diffraction study of interdiffusion and growth in gallium arsenide-aluminum arsenide ((GaAs)_n(AlAs)_m) multilayers, *Journal of Applied Physics*. 51, 357.
- Fullerton E. E., Jiang J. S., and Bader S. D. (1999), Hard/soft magnetic heterostructures: model exchange-spring magnets, *Journal of Magnetism and Magnetic Materials*. 200, 392.
- Grober R. D., Schoelkopf R. J., and Prober D. E. (1997), Optical antenna: Towards a unity efficiency near-field optical probe, *Applied Physics Letters*. 70, 1354.
- Gu Y. S., Zhan X. Y., He J., Ji Z., Zhang Y., and Zhou C. (2005), Structural and magnetic properties of exchange spring type FePt /Fe multilayers, *Materials Science Forum*, 475, 4013.
- Gu Y., Zhang D., Zhan X., Ji Z., and Zhang Y. (2006), Structural and magnetic properties of RF sputtered FePt /Fe multilayers, *Journal of Magnetism and Magnetic Materials*. 297, 7.

- Gupta D., and Ho P. S., In Diffusion Phenomena in thin films and microelectronic materials (Noyes Pub, Park Ridge, 1988).
- Han K., Yu-Zhang K., Kung H., Embury J. D., Daniel B. J., and Clemens B. M. (2002), A structure investigation of epitaxial Fe-Pt multilayers, Philosophical Magazine. 82, 1633.
- Hasegawa T., Li G. Q., Pei W., Saito H., Ishio S., Taguchi K., Yamakawa K., Honda N., Ouchi K., Aoyama T., and Sato I. (2006), Structural transition from $L1_0$ phase to A1 phase in FePt films caused by ion irradiation, Journal of Applied Physics. 99, 053505/1.
- Huang Y., Okumura H., Hadjipanayis G. C., and Weller D. (2002), Perpendicularly oriented FePt nanoparticles sputtered on heated substrates, Journal of Magnetism and Magnetic Materials. 242-245, 317.
- Haason P., Physical Metallurgy, 3rd edition (Cambridge press, New York, 2003).
- Hufnagel T. C., Kautzky M. C., Daniels B. J., and Clemens B. M. (1999), Structure evolution during deposition of epitaxial Fe/Pt(001) multilayers, Journal of applied physics. 852609.
- ICDD Powder Diffraction File, Card No. 27-071, 1998.
- ICDD Powder Diffraction File, Card No. 29-071, 1998.
- ICDD Powder Diffraction File, Card No. 43-135, 1998.
- Iwasaki S., Nakamura Y., and Ouchi K. (1979), Perpendicular magnetic recording with a composite anisotropy film, IEEE Transactions on Magnetics. 15, 1456.
- Iwasaki S. (1980), Perpendicular magnetic recording, IEEE Transactions on Magnetics. 16, 71.

- Iwasaki S., Nakamura Y. (1977), An analysis for the magnetization mode for high density magnetic recording, IEEE Transactions on Magnetics. 13, 1272.
- Weller D., Moser A., Folks L., Best M. E., Lee W., Toney M. F., Schwickert M., Thiele J., and Doerner M. F. (2000), High Ku materials approach to 100 Gbits/in². IEEE Transactions on Magnetics. 36, 10.
- Jin Z. Q., Li J., Thadhani N. N., Wang Z. L., Vedantam T., and Liu, J. P. (2006), Shock compression of FePt and FePt /Fe₃Pt nanoparticles: exchange-coupled nanocomposite magnets, AIP Conference Proceedings, 845, 1157.
- Johnson W. A., and Mehl R. F. (1939), Reaction kinetics in processes of nucleation and growth, Transactions of the American Crystallographic Association. 135, 416.
- Kaiser T., Sigle W., Goll D., Goo N. H., Srot V., van Aken P. A., Detemple E., and Jager W. (2008), Transmission electron microscopy study of the intermixing of Fe-Pt multilayers, Journal of Applied Physics. 103, 063913.
- Kang S., Harrell J. W., Nikles D. E. (2002), Reduction of the fcc to L1₀ ordering temperature for self-assembled FePt nanoparticles containing Ag, Nano Letters, 2, 1033.
- Kang S., Jia Z., Nikles D. E., and Harrell J. W. (2003), Synthesis, self-assembly, and magnetic properties of [FePt]_{1-x}Aux nanoparticles, IEEE Transactions on Magnetics. 39, 2753.
- Kitakami O., Okamoto S., Kikuchi N., and Shimada Y. (2003), Energy barrier enhanced by higher order magnetic anisotropy terms, Japanese Journal of Applied Physics. 42, L455.

- Kneller E. F., Hawig R. (1991), The exchange-spring magnet: a new material principle for permanent magnets, *IEEE Transactions on Magnetics*. 27, 3588.
- Kushida A., Tanaka K., Numakura H. (2003), Chemical diffusion in L1₀-ordered FePt, *Materials Transactions*. 44, 59.
- Lee S.-B., Rickman J. M., and Barmak K. (2003), Phase transformation kinetics and self-patterning in misfitting thin films, *Acta Materialia*. 51, 6415.
- Leineweber T., Kronmuller H. (1997), Micromagnetic examination of exchange coupled ferromagnetic nanolayers, *Journal of Magnetism and Magnetic Materials*. 176, 145.
- Lim B. C., Chen J. S., and Wang J. P. (2004), Thickness dependence of structural and magnetic properties of FePt films, *Journal of Magnetism and Magnetic Materials*. 271, 431.
- Greer A. L. (1997), Measurements of atomic diffusion using metallic multilayers, *Current Opinion in Solid State & Materials Science*. 2, 300.
- Liu J. P., Luo C. P., Liu Y., and Sellmyer D. J. (1998), High energy products in rapidly annealed nanoscale Fe/Pt multilayers, *Applied Physics Letter*. 72, 26.
- Liu J. P., Liu Y., Luo C. P., Shan Z. S., and Sellmyer D. J. (1997), Magnetic hardening in FePt nanostructured films, *Journal of Applied Physics*. 81, 5644.
- Liu J. P., Liu Y., Skomski R., and Sellmyer D. J. (1999), High energy products in exchange-coupled nanocomposite films, *IEEE Transactions on Magnetics*. 35, 3241.
- Ludwig A., Zotov N., Savan A., and Groudeva-Zotova S. (2006), Investigation of hard magnetic properties in the Fe-Pt system by combinational deposition of thin film multilayer libraries, *Applied Surface Science*. 252, 2518.

- Luo C. P., and Shellmyer D. J. (1995), Magnetic properties and structure of Fe/Pt thin films, *IEEE Transactions on Magnetics*. 31, 2764.
- Ma Z., Allen L. H. (1994), Kinetic mechanisms of the C49-to-C54 polymorphic transformation in titanium disilicide thin films: a microstructure-scaled nucleation-mode transition, *Physical Review B: Condensed Matter and Materials Physics*. 49, 13501.
- Maeda T., Kai T., Kikitsu A., Nagase T., and Akiyama J. (2002), Reduction of ordering temperature of an FePt -ordered alloy by addition of Cu, *Applied Physics Letters*. 80, 2147.
- Maeda T., Kikitsu A., Kai T., Nagase T., Aikawa H., Akiyama J. (2002), Effect of added Cu on disorder-order transformation of L10-FePt, *IEEE Transactions on Magnetics*. 38, 2796.
- Massalski T. B., *Binary Alloy Phase Diagrams* (ASM Internatinal, Ohio 1990), p. 1752.
- Mehrer H., *Diffusion in Solid Metals and Alloys, New Series, Group III, 26* (Springer, Berlin, 1990).
- Minh P. T. L., Thuy N. P., and Chan N. T. N. (2004), Thickness dependence of the phase transformation in FePt alloy thin films, *Journal of Magnetism and Magnetic Materials*. 277, 187.
- Moser A., Takano K., Margulies D. T., Albrecht M., Sonobe Y., Ikeda Y., Sun S., and Fullerton E. E., (2002), Magnetic recording: advancing into the future, *Journal of Physics D: Applied Physics*. 35, R157.
- Nakajima H., Fujimori H., Koiwa M. (1988), Interdiffusion and structural relaxation in molybdenum/silicon multilayer films, *Journal of Applied Physics*. 63, 1046.

- Néel L., (1949), *Annales de Geophysique (Centre National de la Recherche Scientifique)*.
5, 99.
- Niarchos D. (2003), Magnetic MEMS: key issues and some applications, *Sensors and Actuators A*. 109, 166.
- Nose Y., Ikeda T., Nakajima H., and Numakura H. (2005), Tracer diffusion of Fe and Pd in FePt and FePt₃, *Diffusion and Defect Data--Solid State Data, Pt. A: Defect and Diffusion Forum*. 237-240, 450.
- Nose Y., Ikeda T., Nakajima H., Tanaka K., and Numakura H. (2003), Fe tracer diffusion in L1₀ ordered FePt, *MRS Proceedings*. 753, 381.
- O'Grady K., EL-Hilo M., and Chantrell R. W. (1993), The characterization of interaction effects in fine particle systems, *IEEE Transactions on Magnetics*. 29, 2608.
- O'Handley R. C., *Modern Magnetic Materials, Principles and Applications* (Wiley, New York, 1999).
- Ohring M., *Materials science of thin films, deposition and structure*. 2nd edition (Academic press, San Diego, CA, 2002).
- Park K. M., Na K. H., Na J. G., Jang P. W., Kim H. J., Lee S. R. (2002), High coercivity and small grains of (Fe₅₇Pt₄₃)_{100-x}Cu_x ternary thin films, *IEEE Transactions on Magnetics*. 38, 1961.
- Philofsky E. M., and Hilliard J. E. (1969), Effect of coherency strains on diffusion in copper-palladium alloys, *Journal of Applied Physics*. 40, 2198.
- Piramanayagam S. N. (2007), Perpendicular recording media for hard disk drives, *Journal of Applied Physics*. 102, 011301/1.

- Platt C. L., Wierman K. W., Svedberg E. B., van de Veerdonk R., Howard J. K., Roy A. G., and Laughlin D. E. (2002), L-10 ordering and microstructure of FePt thin films with Cu, Ag, and Au additive, *Journal of Applied Physics*. 92, 6104.
- Pretorius R., Theron C. C., Vantomme A., and Mayer J. W. (1999), Compound phase formation in thin film structures, *Critical Reviews in Solid State and Materials Sciences*. 24, 1.
- Prokes S. M., Fatemi M., Wang K. L. (1990), X-ray studies of heat treated silicon-germanium/silicon strained-layer superlattices, *Journal of Vacuum Science & Technology, B: Microelectronics and Nanometer Structures*. 8, 254.
- Reddy V. Raghavendra, Kavita S., Gupta Ajay. (2006), ^{57}Fe Mossbauer study of $L1_0$ ordering in $^{57}\text{Fe}/\text{Pt}$ multilayers, *Journal of Applied Physics*. 99, 113906/1.
- Rein G., Mehrer H., Maier K. (1978), Diffusion of platinum-197 and gold-199 in platinum at low temperatures, *Physica Status Solidi A: Applied Research*, 45, 253.
- Richter H. J. (1999), Recent advances in the recording physics of thin-film media, *Journal of Physics D: Applied Physics*. 32, R147.
- Ristau R. A., Barmak K., Lewis L. H., Coffey K. R., and Howard J. K. (1999), On the relationship of high coercivity and $L1_0$ ordered phase in CoPt and FePt thin films, *Journal of Applied Physics*. 86, 4527.
- Roberts W. (1954), X-ray measurements of order in CuAu, *Acta Metallurgica*. 2, 597.
- Rong C., Nandwana V., Poudyal N., Liu J. P., Kozlov M. E., Baughman R. H., Ding Y., Wang Z. L. (2007), Bulk FePt -based nanocomposite magnets with enhanced exchange coupling, *Journal of Applied Physics*. 102, 023908/1.

- Rui X., Shield J. E., Sun Z., Yue L., Xu Y., Sellmyer D. J., Liu Z., and Miller D. J. (2006), High-energy product exchange-spring FePt /Fe cluster nanocomposite permanent magnets, *Journal of Magnetism and Magnetic Materials*. 305, 76.
- Rui X., Sun Z., Xu Y., Sellmyer D. J., and Shield J. E. (2007), Cluster-Assembled Iron-Platinum Nanocomposite Permanent Magnets, *Materials Research Society Symposium Proceedings*. 962E, 0962-P04-03.
- Sato K., Fujiyoshi M., Ishimaru M., and Hirotsu Y. (2003), Effects of additive element and particle size on the atomic ordering temperature of $L1_0$ - FePt nanoparticles, *Scripta Materialia*. 48, 921.
- Sayama J., Yamashita Y., Asahi T., Osaka T. (2007), Sputter-deposited $SmCo_5$ thin films with perpendicular magnetic anisotropy for high density magnetic recording media, *ECS Transactions*. 3, 307.
- Sayama J., Mizutani K., Yamashita Y., Asahi T., Osaka T. (2005), $SmCo_5$ -based thin films with high magnetic anisotropy for perpendicular magnetic recording, *IEEE Transactions on Magnetics*. 41, 3133.
- Seki T. O., Takahashi Y. K., Hono K. (2005), Magnetic properties and microstructure of the granular films processed by annealing FePt-based multilayers, *IEEE Transactions on Magnetics*. 41, 3799.
- Se-Young O., Nguyen D. P., Lee C., Koo B., Lee B., Shimozaki T., Okino T. (2006), Interdiffusion in Fe/Pt multilayer thin films, *Diffusion and Defect Data--Solid State Data, Pt. A: Defect and Diffusion Forum*. 258-260, 199.

- Sharma P., Waki J., Kaushik N., Louzguine-Luzgin D. V., Kimura H., and Inoue A. (2007), High coercivity characteristics of FePtB exchange-coupled nanocomposite thick film spring magnets produced by sputtering, *Acta Materialia*. 55, 4203.
- Shewmon P. G., *Transformations in Metal* (McGraw-Hill, Inc., New York, 1969). p.106-111.
- Shibata K. (2003), FePt magnetic recording media: problems and possibilities for practical use, *Materials Transactions*. 44, 1542.
- Sima V. (2004), Order-disorder transformations in materials, *Journal of Alloys and Compounds*. 378, 44.
- Simizu S., Obermyer R. T., Zande B., Chandhok V. K., Margolin A., and Sankar S. G. (2003), Exchange coupling in FePt permanent magnets, *Journal of Applied Physics*. 93, 8134.
- Skomski R., Coey J. M. D. (1993), Giant energy product in nanostructured two-phase magnets, *Physical Review B: Condensed Matter and Materials Physics*. 48, 15812.
- Skomski R. (2003), Nanomagnetism, *Journal of Physics: Condensed Matter*. 15, R841.
- Staunton J. B., Ostanin S., Razee S. S. A., Gyorffy B. L., Szunyogh L., Ginatempo B., and Bruno E. (2004), Temperature dependent magnetic anisotropy in metallic magnets from an ab initio electronic structure theory: L1(0)-ordered FePt, *Physical review letters*. 93, 257204.
- Sun S. (2006), Recent Advances in Chemical Synthesis, Self-Assembly, and Applications of FePt Nanoparticles, *Advanced Materials & Processes*. 18, 393.

- Sun S., Murray C. B., Weller D., Folks L., Moser A., (2000), Monodisperse FePt nanoparticles and ferromagnetic FePt nanocrystal superlattices, *Science* (Washington, D. C.). 287, 1989.
- Suzuki T., Itoh Y., Birukawa M., and Van Drent W. (1998), Solid immersion lens near field optical approach for high density optical recording, *IEEE Transactions on Magnetics*. 34, 399.
- Suzuki T., and Ouchi K. (2001), Sputter-deposited (Fe-Pt)-MgO composite films for perpendicular recording media, *IEEE Transactions on Magnetics*. 37, 1283.
- Takahashi Y. K., Ohnuma M., Hono K. (2001), Low-temperature fabrication of high-coercivity $L1_0$ ordered FePt magnetic thin films by sputtering, *Japanese Journal of Applied Physics, Part 2: Letters*. 40, L1367.
- Tang L., and Laughlin D. E. (1996), Electron diffraction patterns of fibrous and lamellar textured polycrystalline thin films. I. Theory, *Journal of Applied Crystallography*. 29, 411.
- Tang L., and Laughlin D. E. (1999), Electron diffraction patterns of fibrous and lamellar textured polycrystalline thin films. II. Application, *Journal of Applied Crystallography*. 29, 419.
- Thiele J.-U., Folks L., Toney M. F., Weller D. K. (1998), Perpendicular magnetic anisotropy and magnetic domain structure in sputtered epitaxial FePt (001) $L1_0$ films, *Journal of Applied Physics*. 84, 5686.
- Thompson C. V. (1990), Grain growth in thin films, *Annual Review of Materials Science*. 20, 245.

- Toney M. F., Lee W., Hedstrom J. A., and Kellock A. (2003), Thickness and growth temperature dependence of structure and magnetism in FePt thin films, *Journal of Applied Physics*. 93, 15.
- Verdier M., Veron M., Bley F., Ingwiller F., Dempsey N. M., and Givord D. (2005), Characterization of Fe/Pt bulk multilayers and FePt formations, *Philosophical Magazine*. 85, 11-21, 3157-3172.
- Visokay M. R., and Sinclair, R. (1995), Direct formation of ordered CoPt and FePt compound thin films by sputtering, *Applied Physics Letters*. 66, 1692.
- Walser R. M., and Bene R. W. (1976), First phase nucleation in silicon-transition-metal planar interfaces, *Applied Physics Letters*. 28, 624.
- Wecker J., Schnitzke K., Cerva H., and Grogger W. (1995), Nanostructured Nd-Fe-B magnets with enhanced remanence, *Applied Physics Letters*. 67, 563.
- Weller D., and Doerner M. F. (2000), Extremely high-density longitudinal magnetic recording media, *Annual Review of Materials Science*. 30, 611.
- Wiedwald U., Klimmer A., Kern B., Han L., Boyen H.-G., Ziemann P., and Fauth K. (2007), Lowering of the $L1_0$ ordering temperature of FePt nanoparticles by He⁺ ion irradiation, *Applied Physics Letters*. 90, 062508/1.
- Wierman K. W., Platt C. L., Howard J. K., and Spada F. E. (2003), Evolution of stress with $L1_0$ ordering in FePt and FeCuPt thin films, *Journal of Applied Physics*. 93, 7160.
- Williams D. B., and Carter C. B., *Transmission Electron Microscopy, A Textbook for Materials Science* (Plenum Press, New York, 1996).

- Withanawasam L., Hadjipanayis C., and Krause R. F. (1994), Enhanced remanence in isotropic Fe-rich melt-spun Nd-Fe-B ribbons, *Journal of Applied Physics*. 75, 6646.
- Withanawasam L., Zheng Y. H., and Hadjipanayis G. C. (1995), Nanocomposite $R_2Fe_{14}B/\alpha\text{-Fe}$ and $Sm_2(Fe-Ga)_{17}C_x/\alpha\text{-Fe}$ Magnets, *Scripta Metallurgica et Materialia*. 33, 1765.
- Yao B., and Coffey K. R. (2008), A high throughput approach for cross-sectional transmission electron microscopy sample preparation of thin films, *Journal of Electron Microscopy*. accepted.
- Yao B., and Coffey K. R. (2008), Back-etch method for plan view transmission electron microscopy sample preparation of optically opaque films, *Journal of Electron Microscopy*. 57, 47.
- Yao B., Petrova R. V., Vanfleet R. R., and Coffey K. R. (2007), A modified back-etch method for preparation of plan-view high-resolution transmission electron microscopy samples, *Journal of Electron Microscopy*. 56, 209.
- Yuan F. T., Hsiao H. N., Chen S. K., Chang H. W., You K. L., and Yao Y. D. (2007), Microstructure study of the Co-added FePt thin films with high energy density, *Physica Status Solidi A: Applications and Materials Science*. 204, 4162.
- Yuan F. T., Hsiao S. N., Liao W. M., Chen S. K., and Yao Y. D. (2006), Improvement of energy product in exchange coupled $Fe_{49-x}Co_xPt_{51}$ ($x=0.0,0.7,1.3,2.2$) thin films, *Journal of Applied Physics*. 99, 08E915/1.
- Zeldovich J. B. (1943), On the theory of new phase formation; cavitation, *Acta Physicochimica U.R.S.S.* 18, 1.

- Zeng H., Li J., Liu J. P., Wang Z. L., and Sun S. (2002), Exchange-coupled nanocomposite magnets by nanoparticle self-assembly, *Nature* (London, United Kingdom). 420, 395.
- Zeng H., Li J., Wang Z. L., Liu J. P., and Sun S. (2004), Bimagnetic Core/Shell FePt /Fe₃O₄ Nanoparticles, *Nano Letters*. 4, 187.
- Zhang B., Yang J., Jin L., Ye C., Bashir J., Butt N. M., Siddique M., Arshed M., and Khan Q. H. (1990), Temperature factor of silicon by powder neutron diffraction, *Acta Crystallographica, Section D: Biological Crystallography*. A46, 435.
- Zhang L., and Ivey D. G. (1993), Prediction of silicide formation sequence from the principle of the largest free energy degradation rate, *Materials Research Society Symposium Proceedings*. 311, 299.
- Zhang W., Yubuta K., Sharma P., Makino A., and Inoue A. (2007), Influence of quenching rate on the microstructure and magnetic properties of melt-spun L1₀ - FePt /Fe₂B nanocomposite magnets, *Journal of Applied Physics*. 101, 09K518/1.
- Zotov N., Feydt J., Savan A., and Ludwig A. (2006), Interdiffusion in Fe-Pt multilayers, *Journal of Applied Physics*. 100, 073517.